TECHNISCHE UNIVERSITÄT WIEN

# Master Thesis

## Microfluidic Platform for Biomolecule Quantification

Submitted at the Faculty of Electrical Engineering, Vienna University of Technology in partial fulfillment of the requirements for the degree of Master of Science (Diplom-Ingenieur)

under the supervision of

Ao.Univ.Prof. Dr. Franz Keplinger

Dr. Ioanna Giouroudi

Dr. Georgios Kokkinis

submitted by

**Anna Malec, BSc.**

Matr. Nr. 1025363

Wien, November 2017

# Table of content

# Preface (project summary)

This thesis was part of the Austrian Science Fund (FWF) Stand-Alone Project 'Magnetic Microfluidic Biosensor for the Detection and Quantification of Biomolecules' with Project No. P28544-N30. It proposes a novel, multiplex, portable microfluidic biosensor for detection and quantification of biomolecules conjugated with $Fe_3O_4$ nanoparticles suspended in static fluid. Through this approach, the detection and quantification are simplified and accelerated, and real-time information about the output results is delivered. Quantification hands-on time is reduced using automation and efficient data evaluation by appropriate software. Parts of this work were also funded by the Austrian COMET Programme: K2 XTribology Project No. 849109 (see Appendix A: paper acknowledgments).

# Abstract

The aim of this thesis is to investigate and develop a microfluidic platform for the detection and size characterization of individual magnetic micromarkers suspended in liquid along with the capture and quantification of microorganisms such as *E.coli* bacteria by labeling them with magnetic particles (MPs). Two methods were studied for the above-mentioned development: (1) a dark field video imaging system and (2) magnetophoresis, as quick, inexpensive and compact approaches for microbiomolecule identification and quantification in ex vivo biomedical applications. In the first technique, dynamic processes and interactions of micro/nano particles in liquids (Brownian motion) are being utilized whereas in the second method it is the induced translational motion of MPs due to the externally applied magnetic field gradient. The proposed microfluidic platform is suitable for small sample volumes ($10\ \mu L$), where microsize precision is required. This research has been mostly restricted to experimental examination of *E.coli* comprised solvent, yet the system is applicable for obtaining clinical information about diverse liquid contents when an additional biological binding protocol is provided. A minor limitation associated with the experimental methods is that the concentration range of micromarkers/magnetic particles in the sample needs to be adjusted in such a manner that the number of individual particles in the microscope's field of view is sufficient.

# Introduction

Clinical information about the pathogenic content of liquid is the heart of understanding the causes of various diseases. No diagnosis can be introduced if the noxious agent is unknown. Therefore, detection of pathogens in liquids is a crucial step in the planning of treatment and has received a considerable critical attention in the biomedical field. It gives the information about the presence or an advancement of pathogenic diseases and provides data about the organism's immune response. Identification and quantification of biomolecules plays an important role in understanding biomolecular interactions and enzyme kinetics that take place within a living organism. Researches encompassing these areas give unique insight into cellular behaviors. With the help of biomarkers, protein expression, lipid concentration or antibody-antigen reactions are studied. To date, there has been much progress in the field of bacterial agents' detection. Various strategies have been developed and introduced to detect, quantify and observe their dynamics. These methods include plating, culturing and the use of biochemical tests, modified agar methods, chemiluminescence enzyme immunoassay, Enzyme-Linked Immunosorbent Assay (ELISA) or Fluorescent Bacteriophage Assay (FBA), flow cytometry, solid phase fluorescent capillary immunoassay and Time-Resolved Fluorescence Immunoassay (TRFIA). More recent approaches include Polymerase Chain Reaction (PCR), evanescent wave fiber optic biosensor, PCR combined with acoustic wave sensor, Surface Plasmon Resonance (SPR) sensor, interferometric array sensors and quartz crystal microbalance (QMB). Despite their availability and feasibility, these techniques suffer from several major drawbacks. They are either time-consuming and unprecise, either rather expensive and require highly qualified personnel or their accuracy has not been fully explored.

In this thesis, a quick, inexpensive and compact method for microbiomolecule identification and quantification is proposed where no complicated laboratory facilities neither highly qualified personnel is needed. The method is based on the microfluidic platform that is designed in a way to be applied for micro-sized sample volumes. In this thesis, liquids used to test the system contain *E.coli* bacterium attached to magnetic biomarkers. The overall description of concept covers five sections in this thesis. Specifically, in S*ection 1,* the theoretical background of this research work is explained and provides an insight of how multidisciplinary the proposed sensing device concept is. This section begins with an introduction to microfluidics. Afterwards, the fundamentals of magnetic particles, the forces acting on magnetic particles as well as the concept of magnetic field gradient are discussed. Moreover, the fundamentals of Brownian motion and optical microscopy detection methods are also shortly provided. The section is completed with the explanation of the biological binding mechanism between functionalized magnetic particles and antibody captured *E.coli*.

S*ection 2* concentrates on the methodology and the system design. First, the working principle of the 1$^{st}$ detection/quantification method ''Brownian motion combined with dark field video microscopy'' is described and then the concept of the 2$^{nd}$ technique ''magnetically driven manipulation of MP'' is clarified. Furthermore, this section covers an explanation of the particle tracking system's operation, calculation of resolution and processing of data. Lastly, the requirements valid for systems' design are outlined.

Section 3 is concerned with the experimental 'hands-on' approach. It illustrates the fabrication steps and presents materials and instruments used in the experimental setup. Applied procedures and setting of parameters is elucidated. Finally, the research results and the graphical representation of the output tracking routine coming from the observation of samples with various *E.coli* concentration are demonstrated.

The final section (*Section 4*) presents the conclusions drawn from this thesis tying up the various theoretical and empirical strands and establishes a discussion of the implication of the findings to the future research in this area.

As for further reading, the APPENDICES includes a more detailed description of the binding protocol, properties of the magnetic particles, MATLAB scripts as well as the published SPIE Conference Proceedings of part of this thesis.

# 1. Theory

## 1.1. Microfluidics

Microfluidics is a multidisciplinary field that deals with the behavior of fluids flowing in micro-sized channels. It covers the technology of the fabrication of the channels together with the system's design that drive the flow. The size of a liquid sample delivered into such a microfluidic channel ranges at the microscale. Through the microfluidic approach it is possible to characterize the content of the sample even when little amount of material is at one's disposal.

Parallel to microfluidics, the trend known as 'miniaturization of devices' (lab-on-chip) should be mentioned. Miniaturization improves precision and accuracy of the measurements (as the measurements are completed at the micro scale). It reduces the costs of production (when inexpensive 'soft' [1] microfluidic channels are used) and decrease the overall measurements' time. Miniaturization offers portability, continuous sampling, real-time testing and immadiate information about the results. Therefore, the delivery of a larger amount of data within a shorter time interval is achievable.

Depending on the application, a microfluidic system combines various independent micro-components such as pumps, valves, mixers, heaters, sensing devices and sample delivery mechanism on a single chip. Moreover, the type of the material of the selected microdevice not only affects the design, architecture, costs and fabrication method but also strongly influences the working concept due to the various interactions at the interface (e.g. surface roughness, heat transfer or molecular adhesion [2]) due to micro-scale.

In microfluidics, some of the conditions/phenomena stay similar in comparison to macrofludics, while others are characteristic only for a specific scale range. For instance, the assumption that fluid is homogeneous and infinitely divisible which is valid for any fluid flowing in macrochannels, is also kept for the most micro-liquid flows provided that the hydraulic diameter $D_h$ is greater than $10\ \mu m$ [3] (as in the case of this thesis [see channel's dimensions on the Figure 2.3.4]). Furthermore, depending on the scale, liquids in microfluidic channels might be treated differently than a traditional Newtonian/non-Newtonian or compressible/incompressible fluid. These classifications are not always adequate for micro-scale due to the significance of molecular interactions or other liquids' characteristics. Another important aspect in microfluidics, which is of small relevance in macro-flows and is often ignored there, is the viscous heating. It is an irreversible process in which the work done by a neighboring fluid is converted into heat due to the action of shear forces [4][5]. Other phenomena that are ignored in the macro scale but should be considered in micro-flows are: entrance effects, surface texture, surface tension and electrodynamic effects[1].

### 1.1.1. Laminar vs. turbulent fluid flow

Fluids confined in microfluidic structures demonstrate the physical properties that are not observed on the macroscopic scale. Reduction of the size of the system results in the increase of the area over volume (for a micro-device this ratio is $\sim 10^6\ m$ [6]) and that effects in the dominance of the surface effects over volumetric effects. Thus, in microfluidics, inertia[2][7] forces can be negligible in comparison to viscous, electrostatic/electrodynamic or surface tension forces. The quantity that characterizes this relationship is a dimensionless **Reynold Number** $Re$ given by the equation [8]:

[1] *In electrolyte an electric double layer (EDL) can be formed*
[2] *Forces related to the resistance of an object to the change of its motion*

$$Re = \frac{\rho u L}{\mu} = \frac{uL}{\nu} \tag{1.1.1}$$

where $\rho$ is the density of the fluid $[kg/m^3]$ , $u$ is the characteristic velocity of the fluid $[m/s]$ , $L$ is characteristic linear dimension $[m]$, $\mu$ is the dynamic viscosity of the fluid $[Ps]$ and $\nu$ is the kinematic[3] viscosity of the fluid $[m^2/s]$.

In microfluidics, where Reynold Number $Re$ is much smaller than 1 ($Re \ll 1$), a regular, predictable laminar flow profile will be formed. Apart from localized turbulences resulting from cross-sectional shape/size changes, there will be no other turbulent flows present. Figure 1.1.1 shows the different fluid flow profiles associated with macro- and microfluidics correspondingly. The state, when fluid flow changes its profile from turbulent to laminar, is called **transition state** and appears when Reynold Number ranges between 1200-1600 for a rectangular channel [9].

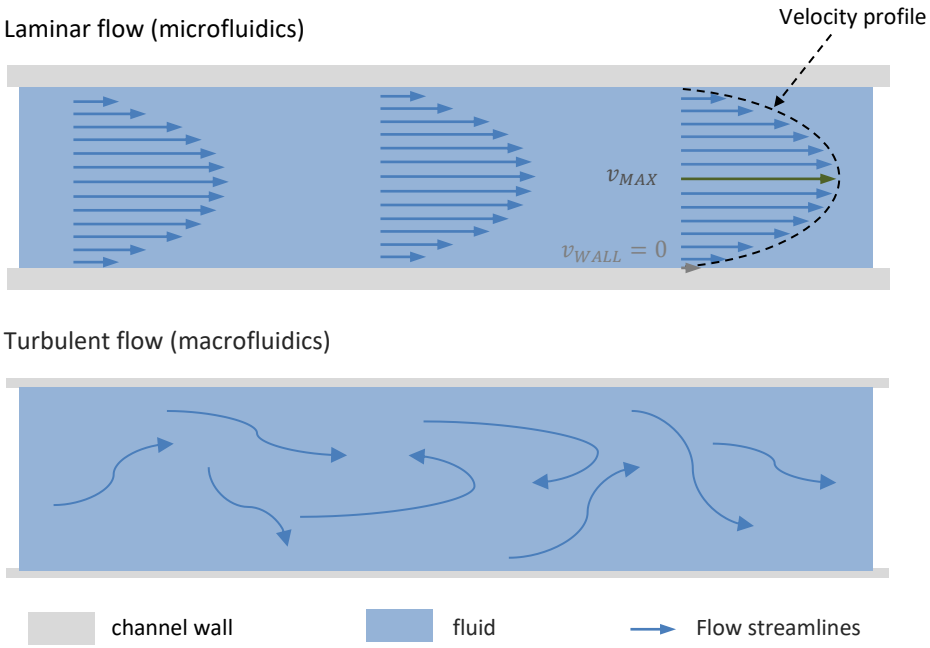


Figure 1.1.1: Streamline representation of the movement of the fluid associated with differently scaled channels. On the top smooth and constant micro-fluidic laminar flow profile with zero velocity at the channel wall and maximum velocity at the center lines. On the bottom, chaotic turbulent flow profile resulting from friction between layers typical for macrofluidics

It should be mentioned, that a fully developed parabolic laminar flow (as the one from Figure 1.1.1 top) of a fluid entering a microfluidic channel with a hydraulic diameter $D_h$ is formed after the distance known as 'hydrodynamic entry length' $L_{E\ Laminar}$ is reached [10]:

$$L_{E\ Laminar} = \kappa \cdot Re \cdot D_h \tag{1.1.2}$$

where $\kappa_{micro} = 0.5$ for microchannel or for macroconduits $\kappa_{macro} = 0.05$. The hydraulic diameter is defined as $D_h = 4A/P$ , with $A$ being the cross-sectional area and $P$ the perimeter[4].

[3] ***Dynamic viscosity*** *is a measure of the fluid's resistance to flow when an external force is applied while* ***kinematic viscosity*** *is the measure of a fluid's inherent resistance to flow when no external force, but only the gravity, is acting on the fluid.*
[4] *A perimeter is a path that surrounds a two-dimensional shape*

### 1.1.2. PDMS channel

For biological lab-on-chip microfluidic applications, where large surface-to-volume ratios are encountered, additional factors such as interfacial biochemistry and hydrophobicity will influence the hydraulic resistance and the flow profile.

PDMS channels (polydimethylsiloxane; a nontoxic, transparent, silicon-based organic polymer) are commonly used in water-based microfluidics due to their inexpensive, relatively quick fabrication process. Their original hydrophobic surfaces can be modified to obtain desired interfacial chemistry e.g. by plasma oxidation to obtain hydrophilicity [11].

### 1.1.3. Glass surface chemistry

In the case of glass surfaces [e.g. borosilicate glass used in this thesis to trap a drop of the fluid, the adhesive behavior of *E.coli* takes over the hydrophobic/hydrophilic interactions [12]. It means that these bacteria, with time, will preferably attach to the glass surface if no additional forces are provided.

## 1.2. Fundamentals of magnetic particles

Depending on the arrangement of magnetic moments[5] within magnetic domains[6] and how they behave when the external magnetic field $\vec{H}$ is applied or removed, a magnetic material can be classified either as dia-, para-, ferro-, ferri- or antiferro-magnetic. The magnetization $\vec{M}$[7] [13] is the measure of the material internal response to this field $\vec{H}$ and is given by [14][15]:

$$\vec{M} = \chi_v \vec{H} \qquad (1.2.1)$$

where $\chi$, termed as 'volumetric magnetic susceptibility', is a dimensionless quantity that varies among materials and may (para- and diamagnetic) or may not (ferromagnetic) be constant. Ferromagnetic materials have the highest value of magnetic susceptibility that reaches even up to $\sim 10^6$ [16], for paramagnetic materials it ranges between $\sim 10^{-5} to \sim 10^{-2}$, while for a diamagnetic materials it is negative and in the order of $\sim -10^{-5}$ [15].

Magnetic domains within ferromagnetic materials are magnetized spontaneously[8][17]. When the total resultant magnetization for all magnetic domains is zero, the ferromagnetic material is said to be demagnetized [16]. At this state, the magnetic moments in each individual domain are oriented differently with respect to the adjacent ones [see Figure 1.2.1].

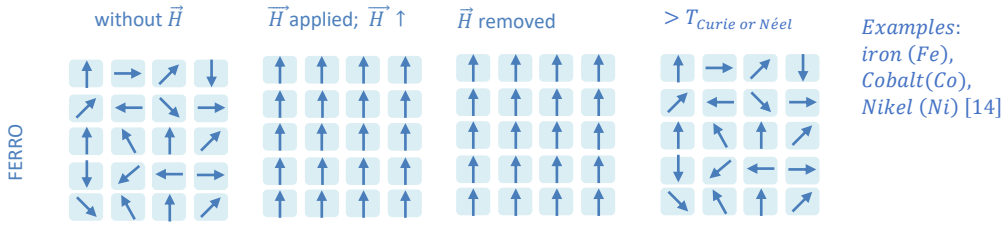


Figure 1.2.1: Arrangements of magnetic moments within domains for a ferromagnetic material

[5] *The origins of magnetic moment $\vec{m}$ can be either microscopic electric currents resulting from the rotation of electrons around the nuclei or when the electrons spin while in orbit.*

[6] *Magnetic domain is defined as a region in a magnetic material in which the individual magnetic moments of the atoms are aligned parallel to one another (the magnetization within the domain is in uniform direction).*

[7] $\vec{M} = \frac{\Sigma_v \vec{m}_{mag}}{V}$ *Total resultant magnetization $\vec{M}$ is the sum of all existing in the sample magnetic moments $\vec{m}$ per unit volume $V$. Magnetization is a measure of how the material responds when a magnetic field is applied to it. It also describes the way that a material changes the magnetic field [13].*

[8] *The spontaneous magnetisation is defined as the magnetization that can exist in individual regions or domains even when no external magnetic field is present [17].*

However, when an external magnetic field $\vec{H}$ is applied, the total resultant magnetization $\vec{M}$ is changing from zero to saturation $\vec{M}_s$ and the magnetic moments are aligning parallel to the direction of the external magnetic field $\vec{H}$ [see Figure 1.2.1]. When the magnetic field is decreased and reverses in sign, the ferromagnetic material's magnetization does not retrace its original path. The magnetization curve of the material exhibits a so-called sigmoid-shaped hysteresis [see Figure 1.2.2]. At zero-magnetic field, the material retains a considerable degree of magnetization called remanent magnetization $\vec{M}_r$, while the value at which the magnetization is back to zero is called coercive field $\vec{H}_c$.

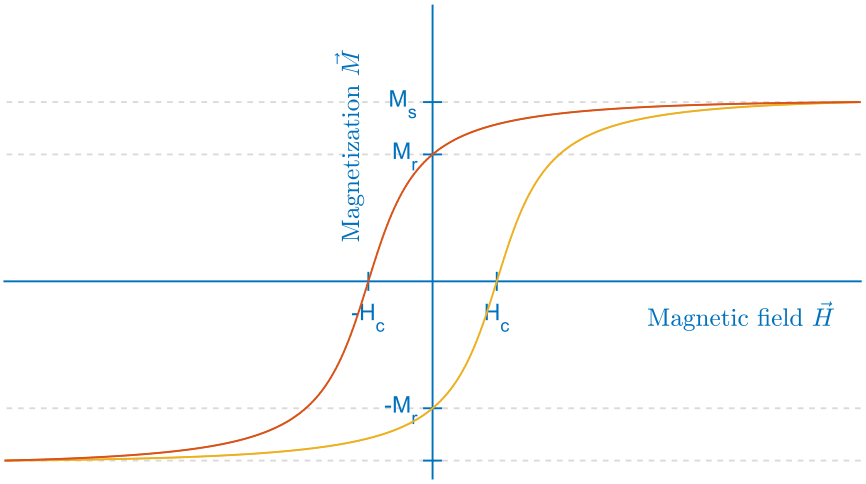


Figure 1.2.2: A typical hysteresis loop of a ferromagnetic material

As in ferromagnetism, paramagnetism is attributed to unpaired electrons' spins whose magnetic moments align with $\vec{H}$. Nevertheless, the configuration of electrons in paramagnets is different, in a way that they are able to freely change the direction of their spin. Therefore, after the removal of $\vec{H}$, the material will return to zero magnetization state [[see Figure 1.2.3 and Figure 1.2.4]. Diamagnetic materials demonstrate an antiparallel magnetization behavior with respect to the direction of $\vec{H}$. In antiferromagnetic materials below Néel temperature, the magnetic moments of neighboring layers are arranged antiparallel to each other so that they cancel each other [16]. In ferrimagnetic materials adjacent layers are also lined up antiparallel [18], however their magnetic moments are unequal, which results in non-zero, spontaneous [17] magnetization.

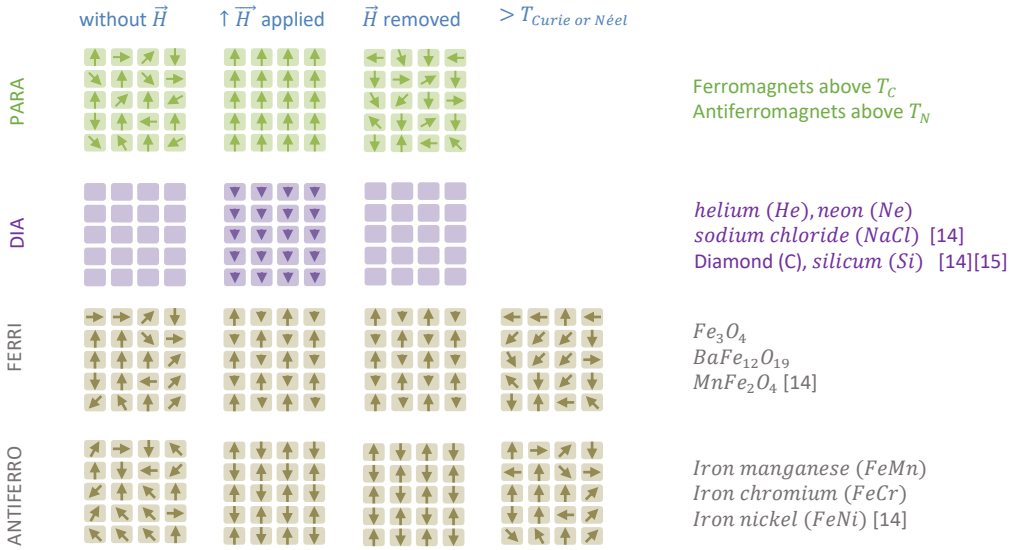


Figure 1.2.3: Arrangement of magnetic moments within domains for different magnetic materials

Another form of magnetism is superparamagnetism. Here, an external magnetic field magnetizes the material, similarly to a paramagnet (there is no remanence, yet the magnetic susceptibility of a superparamagnetic material is greater than that of paramagnet [see Figure 1.2.4]).

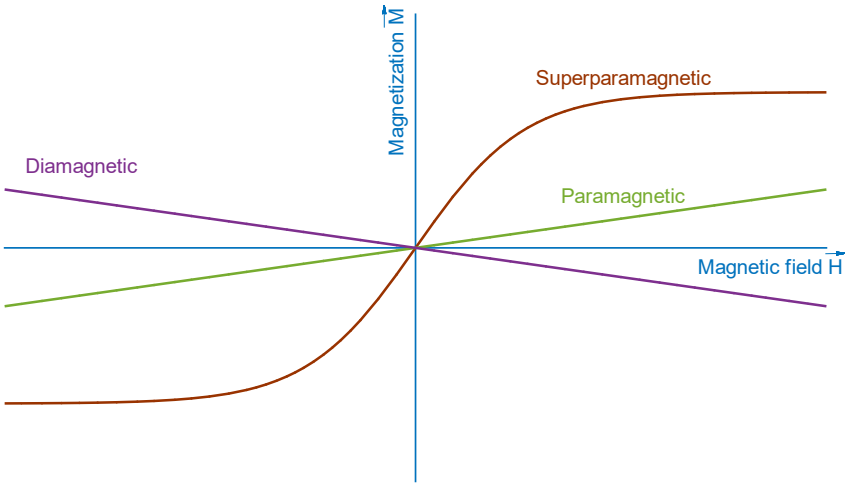


Figure 1.2.4: Magnetization curves of superparamagnetic, paramagnetic and diamagnetic materials

Superparamagnetism is a property that occurs in sufficiently small ferromagnetic or ferrimagnetic nanoparticles. Particles below the Curie or Néel[9] temperature and below the critical diameter $d$ e.g. $\sim 17\ nm$ for magnetite ($Fe_3O_4$)[19] or $\sim 100\ nm$ for ferric oxide ($Fe_2O_3$) and $\sim\ 50\ nm$ for $CoFe_2O_4$ [20] will consist of a single magnetic domain i.e. it experiences uniform magnetization at any field. Such conformation is favorable over multidomain structures and arises due to their small size (the energy that would be needed to divide such small nanoparticle into multiple magnetic domains is higher than the energy required to remain in a single magnetic domain state).

The main advantage of superparamagnetic particles over ferroparticles is the absence of remanence, which if present, would result in unwanted aggregations. Therefore, superparamagnetic particles besides a uniform distribution within a suspension media show the ability to yield large surface binding area and smooth resuspension.

### 1.2.1. Magnetic Particles

Magnetic particles have become a promising biomarker for miniaturized device detection methods not only due to their small size and selective surface functionality but also because of a strong and tunable response to an external magnetic field strength. The potential and versatility of their applications arise also from the fast and simple handling of a sample vial, minimal sample loss, and easily automated protocols. Magnetic nanoparticles are gaining great interest in the biomedical field research. Throughout the years they have facilitated multiple laboratory studies in medical diagnostics and therapeutics; some of them are highlighted in *Table 1.1*.

[9] *$T_{Néel}$ is the temperature above which an **antiferromagnetic** material becomes paramagnetic while $T_{Curie}$ is the temperature, above which, a **ferromagnetic** material becomes paramagnetic.*

| Application | Description/Example | Magnetic particle matertial |
|---|---|---|
| enhanced contrast MRI | Diagnostic; adding MPs to tumor/imaged object to increase the contrast | – superparamagnetic gadolinium-based contrast media [21]<br>– suspended colloids of iron oxide particles<br>– superparamagnetic iron platinum (SPIP) [22]<br>– paramagnetic manganese (Mn) based nanoparticles [23] |
| targeted magnetic drug delivery | Therapeutic; binding nanoparticles with chemotherapy drugs (e.g. $150\ nm$ size particle of albumin surrounding drug paclitaxel) with magnetic delivery [24] to eliminate the cancer | – Fe(salen) based [25] |
| magnetic hyperthermia | Therapeutic; tumor therapy by direct injection of ferrofluids[10] and heating pathogenic cells by applying AC magnetic field (metabolism of cancerous cells is more susceptible to high temperature than of healthy ones) [26] | – magnetite ($Fe_3O_4$) and related composites with cobalt, nickel, or other substitutions [27][28] |
| magnetic separation | Diagnostic; incorporation of a magnet that allows separation/capture of pathogens [29] | – diverse magnetic particles |
| detection of circulating tumor cells (CTC)/pathogens | Diagnostic; immunomagnetic assay coupled with optical method/PCR assays | – diverse magnetic particles<br>– typically $Fe_3O_4$ for CTC [30] |
| Magnetic particle imaging MPI[11] | Diagnostic; diagnostic imaging, measures the location and concentration of nanoparticles in vivo [31] | – SPIO (superparamagnetic iron oxide) [31] |
| Analyzes of stored (for transfusion) blood | When blood deteriorate the erythrocytes produce more microvesicles. These microvesicles can be labeled with magnetic particles [32] and detected by NMR | – typically $Fe_3O_4$ |

*Table 1.1: Biomedical applications of MPs in scientific research*

Depending on the medical application, magnetic particles come in several sizes, various structures different compositions and with different surface modifications. The key to obtain an eligible magnetic behavior within a micro/nano particle is to select a proper magnetic material composition together with an adequate fabrication method. The oldest technique involves coating of the micron-sized paramagnetic core (lumps of iron oxide) with derivatized silane. Another method exploited e.g. by CORTEX BIOCHEM INC described as encapsulation process; it engages mixing of ultra-pure $Fe_3O_4$ (iron (II, III) oxide) powder with a polymer such as polysaccharides, acrylic polymers, and co-polymers, and then grinding and sieving [33]. Magnetic particles that have a polystyrene core coated with an iron oxide and polystyrene coating are paramagnetic in nature (such as SPHEROTECH™) [34] [see Figure 1.2.5], while the composition of magnetite dispersed in a polymer matrix gives superparamagnetic properties to the particles (e.g. BANGS LABORATORIES INC with particle diameter $3 - 8\ \mu m$)[35][36][37]). In this research work INVITROGEN™ products were used. They are uniform, superparamagnetic microparticles ($1 -$

[10] *Ferrofluids are colloidal liquids made of nanosized ferro- or ferri-particles suspended in carrier fluid (water or organic solvent).*
[11] *In MPI in contrast to MRI, it is the particles themselves that are detected, rather than the response that they induce in surrounding tissues.*

$4.5\mu m$) with an even dispersion of magnetic material ($Fe_2O_3$ and $Fe_3O_4$) captured in a highly cross-linked porous polystyrene matrix. Another superparamagnetic nanoparticle (0.5µm) fabrication technique proposes oxidation of metal ion with basic solution to form magnetic crystals, which are later dispersed in a polysaccharide matrix [38].

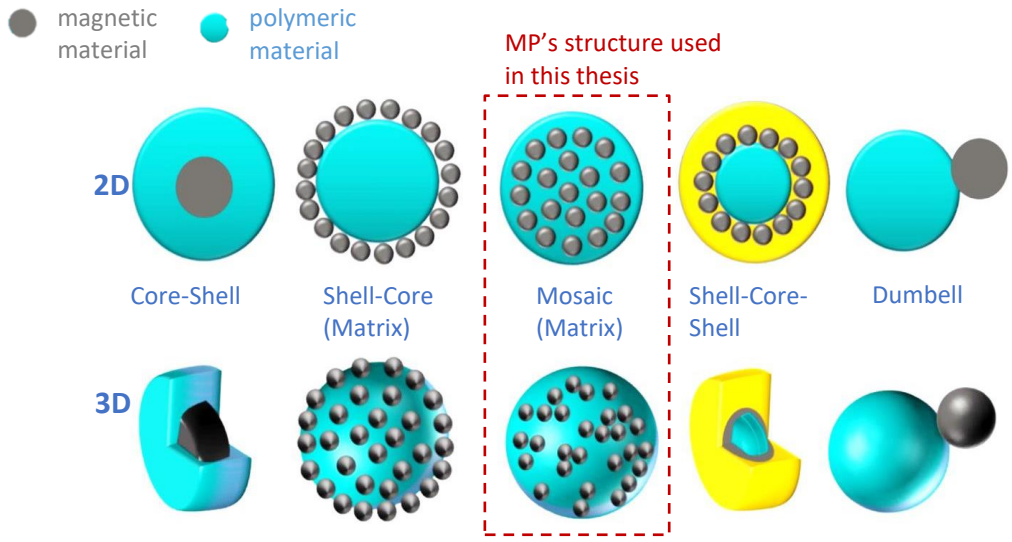


Figure 1.2.5: Various structures of coated Nano-Magnetic Particles (NMPs) [28]

Since exposure to iron induces cytotoxic side effects such as membrane leakage, the formation of apoptotic bodies, chromosome condensation or nuclear blebbing [39], some companies offer to encase the particle with an additional thin protective layer of a pure polymer (e.g. dextran, agarose [40]). This shell additionally decreases the tendency of MPs to agglomerate as well as provides a defined surface area for coupling of various molecules.

Thus, to obtain the desired physical or chemical properties of magnetic particles appropriate surface modification is selected. For instance; some magnetic particles are pre-coupled with ligands. The ligand can be an antibody, protein (protein A or G for Ig purification and immunoprecipitation) or antigen, DNA/RNA probe or any other molecule with an affinity to the desired target [41].

### 1.2.2. Forces acting on magnetic particles

#### *Magnetic Force*

If a point-like magnetic dipole with a magnetic moment $\vec{m}$ is placed in a non-uniform, magnetic flux density $\vec{B}$, a force $\overrightarrow{F_m}$ will be exerted on the particle, resulting in the particle's translational motion towards the maxima of the field [42] [13] [43][44]:

$$\overrightarrow{F_m} = (\vec{m} \cdot \nabla)\vec{B} \tag{1.2.2}$$

Provided that the undermentioned assumptions are satisfied:

- the potential energy of a particle must be greater than the associated with Brownian fluctuations thermal energy,
- the magnetic fields exerting on a magnetic particle of volume $V_{MP}$ are static and in the range of linear susceptibility regime on the magnetization curve [45].

Then the linear relation for the moment at small fields can be characterized by:

$$\vec{m} = V_{MP}\vec{M} = V_{MP}\Delta\chi_v\vec{H} \quad (1.2.3)$$

where $\vec{M}$ is the magnetization of particle, $\Delta\chi_v$ is the difference between volumetric magnetic susceptibility of magnetic particle $\chi_{v_{MP}}$ and the surrounding fluid media $\chi_{v_{fluid}}$ [12] :

$$\Delta\chi_v = \chi_{v_{MP}} - \chi_{v_{fluid}} \quad (1.2.4)$$

Finally, after substituting equation (1.2.3) into (1.2.2) and using the relationship of magnetic induction field $\vec{B}$ in free space: $\vec{B} = \mu_0\vec{H}$ , where $\mu_0$ is the magnetic permeability in free space ($\mu_0 = 4\pi \times 10^{-7}\ Hm^{-1}$), the magnetic force $F_m$, which will act on a superparamagnetic nanoparticle suspended in the biological medium due to externally applied magnetic field gradient is given by [45][46]:

$$\vec{F}_m = \frac{V_{MP}\Delta\chi_v}{\mu_0}(\vec{B}\cdot\nabla)\vec{B} \quad (1.2.5)$$

Note that in the presence of a homogenous field, the force $\vec{F}_m$ on the particle is zero and only a torque will arise.

Described above, the nondestructive method for real-time manipulation of a nanoscale (magnetic) object controlled by a magnetic force is defined as **magnetophoresis.**

Depending on the relative magnitude of fluid's and particle's permeability, magnetophoresis can be classified either as positive ($\mu_{fluid} < \mu_{MP}$) or negative ($\mu_{fluid} > \mu_{MP}$). In the first case, the magnetic particle is attracted to magnetic field intensity maxima and repelled from minima, while for the second case[13] it is attracted to minima and repelled from maxima [47]. In this thesis only positive magnetophoresis is considered (studied MPs are suspended in dielectric media i.e. in DI water or in the solution of PBS-BSA (0.1%) in water and thus $\mu_{fluid} < \mu_{MP}$ .

Phenomenology of magnetophoresis according to equation (1.2.5) can be summarized as:

i. $F_m$ is proportional to particle's magnetic volume[47].
ii. $F_m$ is proportional to the difference of susceptibility between particle and surroundings $\Delta\chi_v$
iii. $F_m$ is directed along the gradient of the magnetic field $\nabla\vec{B}^2$[47][48]

Furthermore, a magnetic field gradient required to induce magnetophoretic motion must overcome random Brownian forces that are characterized by the object and the suspension medium.

### *Drag Force*

When a spherical rigid object of a radius $a$ is placed in a microfluidic channel where the following assumptions are satisfied:

- the fluid is homogeneous (uniform in composition), incompressible[14] [49] and Newtonian[15] [50],
- Reynold's number is small $Re \ll 1$,
- no convergent neither divergent flow takes place,
- the laminar velocity profile of a fluid is fully developed,
- there are no other objects nearby that would affect the flow pattern,
- the fluid of viscosity $\eta$ (e.g for water viscosity $\eta_{H_2O} = 8.9 \times 10^{-4}\ [N\ s\ m^{-2}]$) is assumed to move with a constant velocity $\vec{u}$ along a z-axis (steady-state motion [51]),
- at the surface of the sphere the no-slip boundary condition [16]( $v(r = a) = 0$) [51] is met,

[12] Volumetric magnetic susceptibility of water at 20°C is $\chi_{v\_H_2O} = -9.04 \times 10^{-6}$ *using SI convention (dimentionless volumetric susceptibility), while the magnetic susceptibility of the magnetic particle that was used in this thesis' experiments is* $\chi_{v\_MP} = 0.7$ *[see Appendix C].*

[13] *e.g of diamagnetic particles diluted in ferrofluid.*

[14] Incompressible means that the effects of pressure on the **fluid density** are zero or negligible; density of the fluid does not change over time or space [51].

[15] *Newtonian fluids obey Newton's law of viscosity: the* ***viscosity is independent*** *of the shear rate.*

[16] *Assumes* ***zero*** *fluid* ***velocity*** *at the solid boundary.*

and the particle starts to migrate with a velocity $\vec{v}_P(t)$ [see *Figure 1.2.6*] e.g. due to magnetophoretic force $F_m(t)$ described in formula (1.2.5), then the opposite to that magnetophoretic ($F_m$) force, the so called **hydrodynamic drag force** $\vec{F}_d(t)$ will arise [51]:

$$\vec{F}_d(t) = 6\pi\eta a \Delta\vec{v}(t) \tag{1.2.6}$$

where $\Delta\vec{v}(t)$ is the flow velocity relative to the object and according to *Figure 1.2.6* it is described as the difference between the fluid velocity $\vec{u}$ relative to observer and the velocity of a particle $v_P(t)$ relative to the observer[51]:

$$\Delta\vec{v}(t) = \vec{u} - \vec{v}_P(t) \tag{1.2.7}$$

Equation (1.2.6) is also known as the **Stokes' law**, which is derived by applying the Stokes flow limit[17] to Navier-Stokes equations[18].

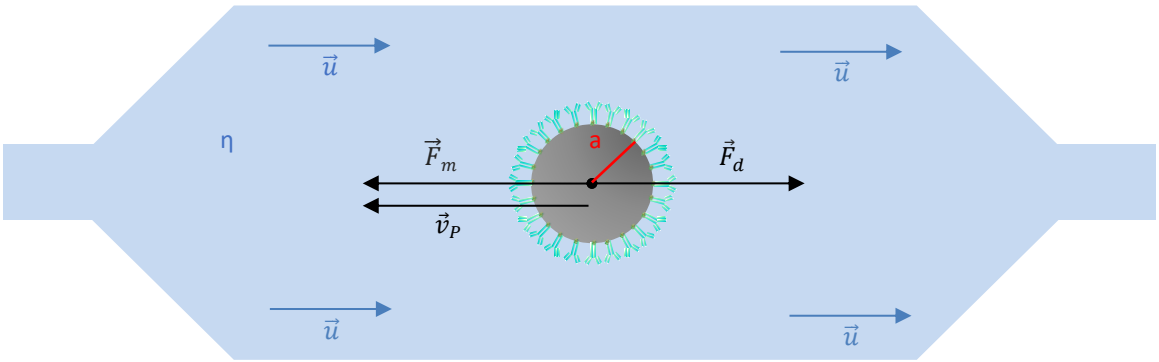


Figure 1.2.6: Idealized model of a Stokes drag force $\vec{F}_d$ acting on a spherical particle of radius $a$, when the sphere moves from right to left due to the induced magnetic force $\vec{F}_m$with a velocity $\vec{v}_{MP}$ in microfluidic channel filled with a fluid of viscosity η and velocity $\vec{u}$

Frictional Stokes drag force $\vec{F}_d$ arising from differences in velocities $\Delta\vec{v}$ between the liquid $\vec{u}_{fluid}$ and a particle $\vec{v}_{MP}$ is composed of a pressure drag force and shear stress drag force $\left(\vec{F}_d = \vec{F}_p + \vec{F}_s\right)$ and resists very small relative motion (creeping motion) between rigid sphere of diameter $a$ and a fluid of infinite extent, of viscosity $\eta$ **[**52**].**

For many lab-on-a-chip systems, due to limitations in fabrication methods, the microfluidic channel usually has a rectangular cross-section. Fourier sum representation is required to find a solution to pressure driven, steady-state flows in such channels (the Poiseuille flow) or an approximation of infinite parallel-plate channel can be used instead [51]. In the case of this thesis's experiments infinite parallel–plate channel and no fluid flow in the channel: $\underline{\vec{\boldsymbol{u}} = \mathbf{0}}$ is assumed. Only the spherical magnetic particle MP is in motion $\underline{\vec{\boldsymbol{v}}_{\boldsymbol{MP}} \neq \mathbf{0}}$.

### *DVLO Force*

Apart from fluid drag effects, additional forces like adhesion and sliding friction can affect the motion of a manipulated particle. Adhesion is defined as a pull-off force and can arise due to van der Waal interactions, hydrogen bonding, covalent bonding or electrostatic charging [53].

DVLO[19] refer to the interactions between charged surfaces' particles within a liquid medium. That includes the effects of the van der Waals attractions together with the electrostatic repulsions emerging while the double layer of counterions is formed around the micro/nanoparticle (with negatively charged outermost layer) [54] [see Figure 1.2.7]. The van der Waals forces contribute to attraction while electrostatic forces to repulsion of two adjacent particles (or repulsion at a particle-solid surface interface). Therefore, if the neighboring object is

[17] *Limit of small Reynolds numbers* $Re \ll 1$.
[18] *Equations describing motion of viscous fluid substances arising from Newton 2nd law* $(F = dM/dt)$ *for fluid motion.*
[19] *Theory named after four scientists:. B. Derjaguin, L. Landau, E. Vervey, and T.Overbeek.*

negatively charged, a microparticle that has negative outermost layer will experience electrostatic repulsion force.

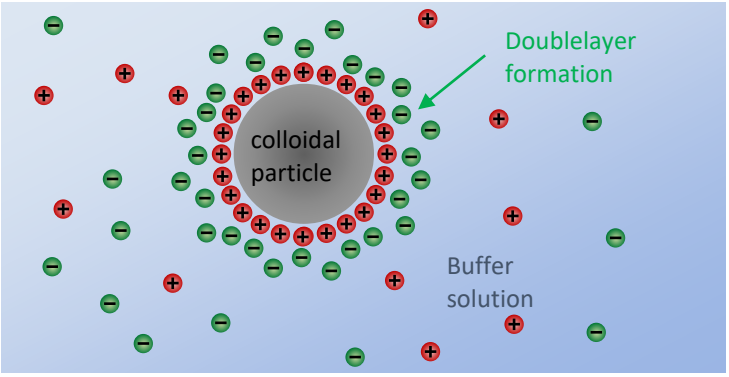


Figure 1.2.7: Electrical double layer formation around a colloidal particle. The outermost layer is negatively charged. If two identical particles are in close proximity, then van der Waals forces will act to attract particles while electrostatic forces will act to repulse them.

### 1.2.3. Non-uniform magnetic field formation

One method to manipulate a magnetic particle is to induce a non-uniform magnetic field by applying a DC current $\vec{I}$ through a microconductor. According to Biot-Savart law, the induced magnetic field $\vec{B}_P$ at a point $P$ [see Figure 1.2.8] is expressed by the equation:

$$\vec{B}_P = \frac{\mu_0}{4\pi}\int_C \frac{Id\vec{s}\times\hat{r}}{r_{PQ}^2} \tag{1.2.8}$$

where $d\vec{s}$ is a current length element, $r_{PQ}$ is a distance from $Q$ to point $P$ and $\hat{r}$ is its direction vector.

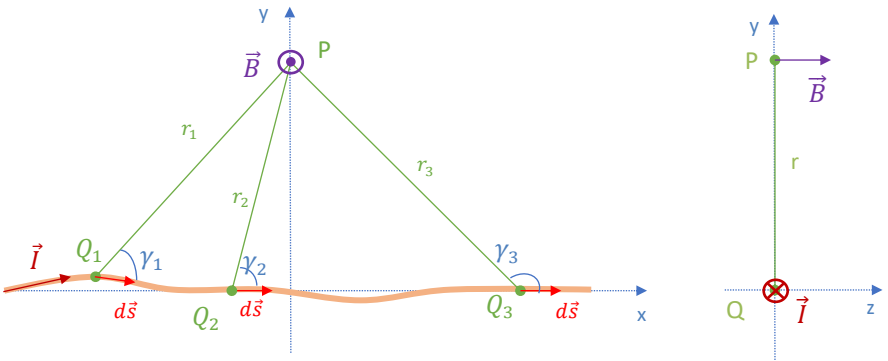


Figure 1.2.8: Biot-Savart law for magnetic field generated by a steady electric current over the path $C$ in a wire

For a symmetric system (i.e. for an infinite long straight wire), where the magnetic field around an 'Amperian loop' is constant, equation (1.2.8) is computed to (1.2.9), which holds that the magnetic flux density $B$ decreases with the distance from a conductor $r$ [as seen in Figure 1.2.9] creating a static non-uniform magnetic field.

$$B_P = \frac{\mu_0 I}{2\pi r} \tag{1.2.9}$$

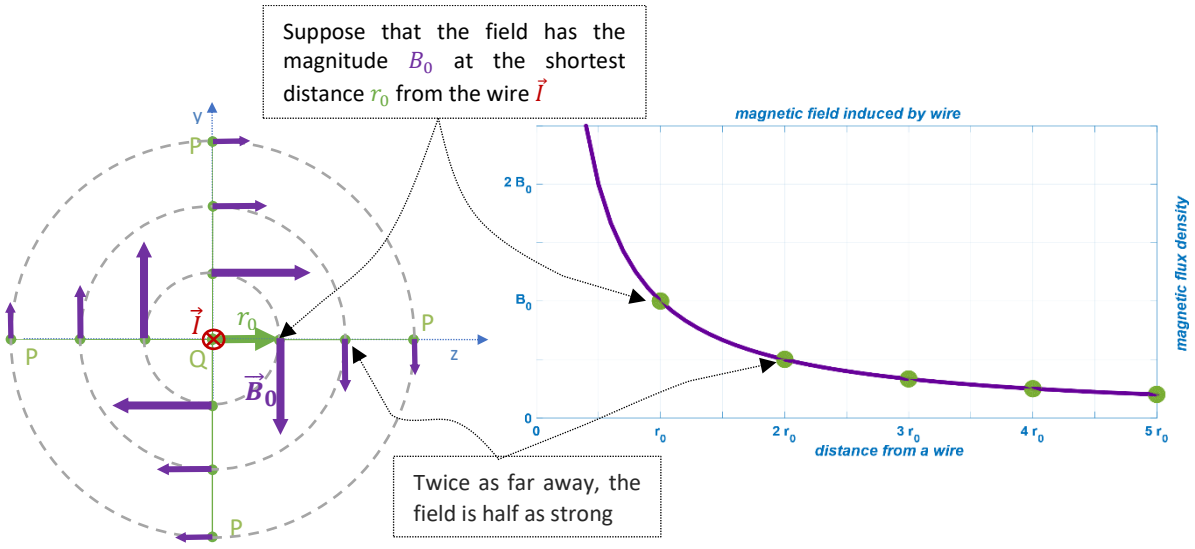


Figure 1.2.9: Nonuniform magnetic field formation induced by DC current flowing through infinitely long straight wire

Details on the analysis and simulations of magnetic fields around non-symmetric microsystems (i.e. rectangular microconductors used for this thesis' experiments can be found in previous works [55].

## 1.3. Brownian motion

Brownian motion, defined as random, chaotic movements of microscopic particles suspended in liquid or gasses, is a result of collisions and thermal fluctuations between neighboring atoms/molecules. This phenomenon, observed for all objects within a solution, i.e. not only for smaller solvent molecules but also for larger colloidal particles, occur at the molecular level and evoke the process of a diffusion expressed mathematically by the first Fick's law (1.3.1). This equation describes the migration of molecules in a direction opposite to the concentration gradient $\partial c/\partial x$ [56]:

$$J = -D \cdot \frac{\partial c}{\partial x} \tag{1.3.1}$$

$J$ is the diffusive flux in $[mol/m^2 s]$, $D$ is the diffusion coefficient in $[m^2/s]$, $c$ is the concentration in $[mol/m^3]$ and $x$ is the position(length) in $[m]$.

In the case of magnetic particles suspended in water both magnetic particles and the water molecules will undergo Brownian motion, though, the displacement will be observed at a different time and size scale. In this thesis, the time of interest $t$ is much larger than the average time $\tau_m$ between molecular collisions. The mass $M$ of a particle under our investigation is also much larger than the mass $m$ of individual molecules forming the viscous fluid, so that the second ones are treated on a continuum level[20] as a Newtonian fluid with constant shear viscosity $\eta$ [56].

In the suspension used in this thesis, magnetic particles will collide with fast-moving fluid molecules and change their trajectories in uncoordinated, contingent step-manner. This movement depends on the size and shape of the particle together with the viscosity $\eta$ and the temperature $T$ of the medium and is described by a mean square displacement $\langle r(t)^2 \rangle$ in the equation [57]:

[20] *Although the fluid is composed of molecules, it is assumed to be treated as continuous.*

$$\langle r(t)^2 \rangle = 2 \cdot DIM \cdot D \cdot t \tag{1.3.2}$$

$DIM$ is the number of dimensions under consideration, $t$ is the displacement time, $D$ is a diffusion coefficient that for an idealized spherical particle of radius $r_s$ according to Stokes-Einstein equation equals to:

$$D = \frac{k_B T}{6\pi\eta r_s} = \frac{RT}{6\pi N_A \eta r_s} \tag{1.3.3}$$

where $k_B$ is the Boltzmann constant $k_B \approx 1.38 \times 10^{-23}\,[J \cdot K^{-1}]$ ; $R$ is the gas constant $R = 8.3144598(48)\,[kg \cdot m^2 \cdot s^{-2} \cdot mol^{-1}]$ and $N_A$ is the Avogadro constant $N_A = 6.022140857(74) \times 10^{23}\ [mol^{-1}]$.

Apart from the above described translational motion, molecules can also experience rotational motion (i.e. re-orient about its own axes). Thus $D$ can have the form of (1.3.4) and it will depend on the temperature $T$ and the rotational friction coefficient which is the characteristic of an object defined as $f_{rot} = 8\pi {r_s}^3$.

$$D_{rot} = \frac{k_B T}{f_{rot}} \tag{1.3.4}$$

For a $2D$ system, as in the case of investigations in this thesis, where only $x$ and $y$ -displacements are considered, equation (1.3.2) becomes:

$$\langle r(t)^2 \rangle = \langle x(t)^2 \rangle + \langle y(t)^2 \rangle = 4Dt \tag{1.3.5}$$

Due to its randomness, the evolution of a particle position is difficult to deduce. In such cases, stochastic mathematical models, which estimate the pattern or trend in trajectories using different configurational probability distribution methods, are employed. In this study, however, no such stochastic approach is required, since the displacement path is determined experimentally by utilizing a particle tracking technique with dark field video microscopy [see Section 1.4.1]. This displacement is described by the equation [58]:

$$MSD(n) = \frac{1}{N-n} \sum_{i=0}^{N-n} ((x_i - x_{i+n})^2 + (y_i - y_{i+n})^2) \tag{1.3.6}$$

Where MSD is Mean Squared Displacement, $N$ is the total number of collected frames, $t$ is the time interval for a given displacement that equals to $t = n\Delta t$ , where $n = 1, \dots, N-1$ and $\Delta t$ is the time between two consecutive frames (i.e. $\Delta t$ is the fixed time step between neighbouring camera' frames).

The number of such displacements (i.e. MSD) is $N - n$ and therefore large for small $n$ which would result in well averaged $MSD$ values [58].

In other words, MSD describes the spatial extent of random motion of a Brownian particle and is calculated from its $x_i$- and $y_i$-coordinates for every frame $i = 1, \dots, N$ at the interval $t = n\Delta t$ between each frame. Thus, for $MSD(1)$ we take the arithmetic average of all (i.e. $N-1$) displacements whereas for $MSD(N-1)$ it is only one displacement. Hence, to get better averaging it is advisable to take the first few MSDs i.e. $MSD(1)$ or $MSD(2)$ etc.

A detailed description of this approach and how to experimentally obtain MSD of a particle undergoing microscopic motion from dark field video microscopy is presented in Section 2.1.3.

Relevant in this thesis is the **size** of a particle undergoing Brownian motion and it can be calculated by substituting the Stokes-Einstein equation (1.3.3) into (1.3.5) and (1.3.6). Therefore, $r_s$ can be rewritten in the form of (1.3.7), and will correspond to the calculated hydro-dynamic radius (which includes both solvent (hydro) and shape (dynamic) effects) of a hypothetical sphere that diffuses in similar manner as the particle under investigation:

$$r_s = \frac{k_B T}{6\pi\eta} \cdot \frac{4n\Delta t}{MSD(n)} \tag{1.3.7}$$

Assumed that only Brownian fluctuations are present in the fluid, the relationship between MSD and lag time ($n\Delta t$) is linear (which is further experimentally proven by the studies conducted e.g. by [59]) and takes the form of the equation [58]:

$$MSD(n) = 4\sigma^2 - \frac{4}{3}Dt_E + 4D \cdot n\Delta t \tag{1.3.8}$$

Expression $4D$ corresponds to the slope of a function and $4\sigma^2 - \frac{4}{3}Dt_E$ to its offset (y-intercept), where $t_E$ is the camera exposure time[21] and $\sigma$ the dynamic localization uncertainty[22].

The lower and upper limits, for the size of a colloidal particle $d_p$ to be classified as 'Brownian', are not sharply defined. The minimum is set by the condition that solvent molecules must interact with the particle surface (which is characterized through viscosity and temperature). This phenomenon is observed when the size of a particle is at least $\sim 10$ times bigger than the solvent molecule (i.e. $d_{p\ LOWER\ LIMIT}$ is $\sim 1\ nm$). On the contrary, the maximum size is limited by the feasibility of thermal motion and the experimental time range. In other words, factors such as e.g. gravitational fields should not overcome relevance of Brownian fluctuations (i.e. $d_{p\ UPPER\ LIMIT}$ is said to be $\sim 10\ \mu m$) [60]. Let us consider now a short time interval during which 'larger' Brownian particles hardly change their position. Within this time domain, solvent molecules however experience many thermal displacements over distances of their own size. Therefore, when the time scale is changed and Brownian particles movement is visible for this subsystem, then the fluid is said to be in instantaneous equilibrium in the field generated by Brownian particles [61].

The dynamics of Brownian motion are affected by potential (direct) and hydrodynamic (indirect) interactions. The first ones appear due to the particle's energy, while the second ones are mediated by the solvent. Consequently, the particle trajectory is chaotic and has a nontrivial geometric structure. To represent its path, stochastic (or probabilistic) processes described in [62] [63] such as Random Walk, Wiener or Poisson Process are commonly used.

Brownian motions are confined to liquids/gases, due to lack of free mobility of atoms within a solid (i.e. bonds between neighboring atoms in solids are too tight for thermal collisions to happen). The same is valid when the temperature is dropping towards absolute zero ('freezing' into a solid state).

## 1.4. Optical Detection

### 1.4.1. Dark-field microscopy

By controlling the aperture diagram placed at the front focal plane of the substage condenser, the amount and angle of the light hitting the specimens can be selected. Typically, in dark field microscopy an object is illuminated with a hollow cone of light, so that the deviated (first- and higher order diffracted light) rays, but not the illuminating (zeroth-ordered light) [64] rays enter the objective lens [see Figure 1.4.1 [65]]. Therefore, if the sample is removed from the stage, no light can enter the objective.

Due to irregularities on the specimen's surface and hence the interactions of photons with the surface's particles, the direction of propagation of light is altered. This modified (scattered) light enters the objective, while the unscattered light is excluded (by proper configuration of illumination system together with aligned condenser and lenses).

[21] *Frame rate refers to number of individual frames within one second, while exposure time refers to the amount of time that each individual frame is exposed to light. So if the exposure time is set to 100, it means that each frame is exposed for 1/100th of a second.*
[22] *Uncertaintities due to measurements limitations.*

For a dark field microscopy system without additional Iris Diaphragms [see Figure 1.4.1 a)], the numerical aperture of the substage condenser $NA_{cond}$ must be $\sim 15\%$ 'just' higher than the $NA_{objective}$ [66]. NA is characteristic of an objective lens and is defined in equation (1.4.1). The angle $\alpha$ designates half of the maximum angle under which beams emitted from the focus F can be collected by an objective lens and $n$ corresponds to the refractive index for a medium ($n_{H_2O} \approx 1.33$, $n_{oil} \approx 1.518$ [67], $n_{air} \approx 1.0029$).

$$NA = n \sin \alpha \tag{1.4.1}$$

Oil medium is preferable over the air because it increases NA (with proper condenser setup even up to $NA = 1.4$ as in [68]) and resolution of the lens; however, the objectives must be specially optimized for the respective media. The resolution of an optical imaging system is limited by diffraction, which is characterized by the wavelength of light $\lambda$ illuminating the circular aperture, and by the aperture's size. According to Rayleigh criterion[23], the distance $d$ between two closely spaced airy disks[24], which can still be distinguished by the observer **as separate**, is given by the equation [69]:

$$d = \frac{0.61\lambda}{NA} \tag{1.4.2}$$

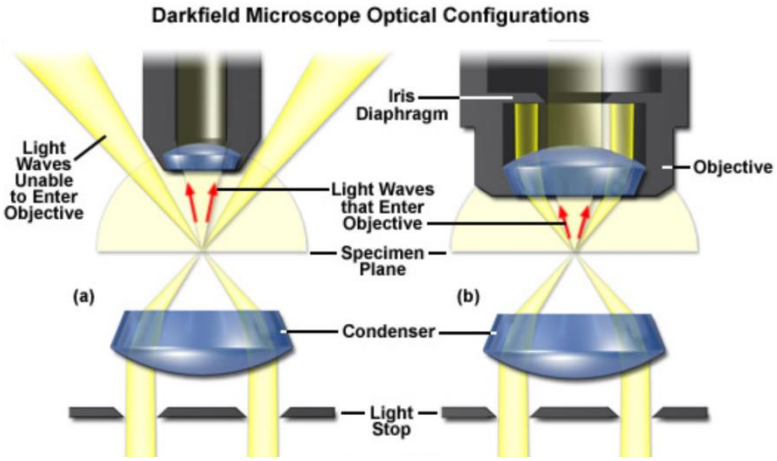


Figure 1.4.1: Elimination of direct light illumination by means of dark field sub-stage condenser and spider Light Stop a) without and b) with additional Iris Diaphragm [65]

In darkfield microscopy, very small objects (even smaller than the limit of resolution $d$ for the objective) can be detected [70]. This is possible due to the light diffraction phenomena where the particle becomes visible as bright, minute diffraction disc (still, in order to differentiate between adjacent particles, the distance between them must be greater then $d$). The limit of detection in a dark field microscope is determined by the amount of contrast attainable between the object and the background [64], thus, in order to enhance it, illumination intensity is increased. The above described scattering phenomenon also brings disadvantages, since even small dust particles will be visible as a bright spot on a dark background image. Therefore, clean working conditions are crucial.

Dark-field microscopy does not always require a special sub-stage condenser. A hollow cone of light can be created e.g. by inserting a black circular piece of paper material or another opaque 'spider stop' in a plane conjugate to the aperture plane [71]. To obtain a dark field image from a phase-contrast microscope, the $100\times$ phase-contrast annular ring could be combined with a $10\times$ or $20\times$ objective. Alternatively, a bright-field

[23] *Criterium defining the shortest distance at which two point emitters can be distinguished as separate objects.*
[24] *That is the pattern that arises from diffraction at circular pinhole.*

microscope connected to a digital image processor that removes the low-frequency components (corresponding to zeroth-ordered light) of the Fourier spectrum, can also give a dark background image as an output [72].

Dark-field microscopy is best suited for revealing outlines, edges, and boundaries of the object. The contrast (in intensity) created between the background and the imaged object is an advantage when applying image processing detection and tracking algorithms based on the pixel intensity changes.

### 1.4.2. Fluorescence microscopy

The use of fluorophores requires several crucial modifications in an optical imaging system. To evoke sufficient photon excitation from a fluorophore, high-intensity light sources such as High-Pressure Mercury Vapor Arc-Discharge lamp (the intensity of this lamp is $100\times$ greater than the halogen one) xenon arc, halide lamps, laser or low-cost LED are used. The spectrum of emission covers UV to infrared light, thus a dichroic mirror positioned at $45°$ is necessary to filter the wavelength of interest. Once the fluorophore is excited by absorption of light, a photon is promoted from the ground state singlet state $S_0$ to an excited state $S_1$ as presented on Figure 1.4.2 [73]. The return via fluorescence to vibrational levels of $S_0$ electronic ground state, takes place in the time range of about $0.1-100\ ns$ [74] and competes with nonradiative pathways [75].

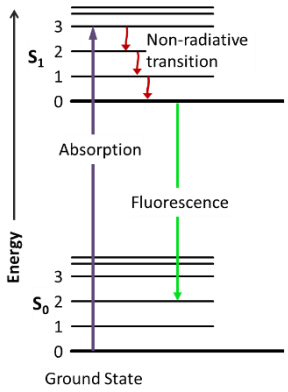


Figure 1.4.2: Simplified Jablonsky Diagram for singlet states fluorescence [73].

The fluorescence is emitted by the sample in all directions but only a specific cone of light is captured by the lenses. Therefore, to extract this weak light from the strong excitation source light, high-quality dichroic, block and excitation filters are required. Once, the desired wavelength is filtered from the spectrum, it reaches photodetectors such as charge-coupled device (CCD), electron multiplied charge-coupled device (EMCCD) cameras or avalanche photodiodes (APD) [76].

Common limitations of fluorescence microscopy are photobleaching (where fluorescent dye molecules are photochemically destroyed mostly due to photo-oxidation), phototoxicity (fluorescent dye acts as a photosensitizer and causes damages in the presence of molecular oxygen), optical resolution (noise level coming from photobleaching) and misrepresentations of small objects.

Organic dyes fluorophore labels are characterized by high extinction coefficient $10^4-10^5 M^{-1}cm^{-1}$ (a parameter that defines how strong a substance absorbs light at a given wavelength), Stokes shift (wavelength difference between maxima of absorption and emission) typically of $20-40\ nm$ and moderate-to-high QYs[25] [77]. In this thesis' experiments, the used organic dye Alexa Fluor has an excellent solubility in water and superior photostability compared with fluoresceins or rhodamines.

In a conventional widespread epi-fluorescent microscope, the fluorescent label in the sample is excited using a mercury or xenon lamp [see Figure 1.4.3 [78]]. The specimen is bathed in light and can be viewed directly by eye

[25] *Quantum Yield is the efficiency of a given fluorophore* $\Phi = \frac{\#\ photons\ emitted}{\#photons\ absorbed}$

or projected directly onto an image capture device (as in contrast to confocal microscopy where sample needs to be scanned with a laser [79]).

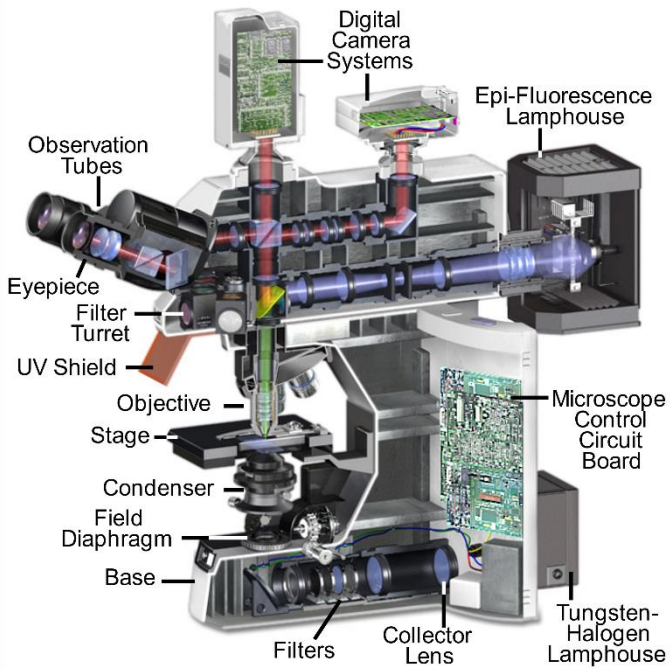


Figure 1.4.3: Optical train of widespread epi-fluorescence microscope equipped for both transmitted and reflected fluorescence microscopy [78]. Similar microscope was used for this thesis' experiments.

### 1.4.3. Video microscopy

To convert an optical image into an electrical signal, a camera is attached to a microscope by the means of optical couplers. These are e.g. 'c mounts' on a dedicated phototube on a trinocular head. Optionally, there are intermediate optics (reduction lenses) introduced to reduce the image size to better match the small sensor size on the digital camera. Depending on the setup, the camera can also be connected to one of the microscope's eyepieces [80].

Cameras use semiconductors to convert light energy into electrical energy. When a light hits the photodiode it excites an electron, which jumps from the valence to the conduction band and an electron-hole pair is created. The electron travels in the conduction band through the n-type semiconductor toward the positive pole of the battery, while the hole 'travels' in the opposite direction (p-type semiconductor towards the negative pole of battery). The greater the light intensity is, the greater the number of created electron-hole pairs and the greater the photocurrent. Both, Charge-Coupled Device (CCD) and photodiode array (here each photodiode acts as a picture element or pixel) cameras create electron-hole pairs. Thus, the digital image is an array of integers obtained by sampling and quantizing the optical image [64] [81].

## 1.5. Biology

### 1.5.1. Escherichia coli

*Escherichia coli* are commonly present in nature, genetically diverse, Gramm negative and anaerobic bacteria species. They can be isolated from a variety of host endotherm organisms along with soil, sediments and water. In humans, noninfectious strains of this prokaryotic, coliform microorganism are a part of the normal flora of

the gastrointestinal tract, while pathogenic strains are typically known as food poisoning noxious agents [82]. Most commonly used laboratory *E.coli* subtype is *K-12*: a genetic variant shown in Figure 1.5.1 [83][84], which is also used in this thesis experiments. This strain belongs to Risk Group #1 according to the European biological agents' safety directive (1 - 4 scale range) and even when accidentally consumed in laboratory, it does not colonize in the human gut [85]. Wild-type *K-12 E.coli* differs from pathogenic *E.coli* in the way, that the second one is missing genes; this absence is responsible for the pathoadaptive mutations [86]. *E.coli* is a rod-shaped, extensively investigated bacterium, (with an approximate width of $0.5\ \mu m$ and a $2\ \mu m$ length [87]). It can persist relatively long in sterile soil/ water conditions (even up to 50 days in case of K-12 strain W3110 [88]). Its envelope consists of three layers: the cytoplasmic membrane, the peptidoglycan (a rigid structure determining the rod shape), and the outer membrane (enclosed bacterial capsule), covered with different surface proteins serving as binding targets (epitopes) for antibodies [89]. Depending on the genetic variant, *E.coli* can have optionally a flagella assembly (including the K-12 wild strain researched in this thesis [90]) for locomotion purposes.

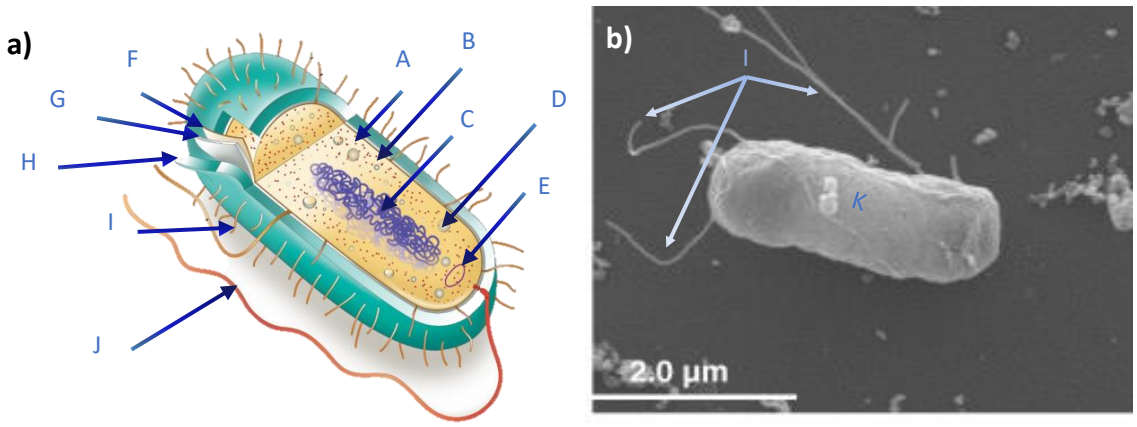


Figure 1.5.1: Cell structure and SEM micrograph of K-12 E.coli strain a) prokaryotic cell structure: A is the cytoplasm, B is the ribosome, C is the nucleoid, D is the inclusion, E is the plasmid, F is plasma membrane, G is the cell wall, H is the outer membrane, I the is pilus, J is the flagellum b) Scanning Electron Microscope (SEM) micrograph of rod-shaped E.coli K12, where I is the peritrichous arrangement of flagella, K is the bacterial capsule[83][84].

### 1.5.2. Rabbit polyclonal antibody

The rabbit is the most frequently used laboratory animal for polyclonal antibodies production due to the ease of handling and bleeding, high antibody affinity and titer and immune responses against a broad range of antigens (broader than for mouse or other rodents) [91][92]. Polyclonal antibodies, as opposed to monoclonal, are heterogeneous and will contain a mixture of antibodies of different affinities recognizing multiple epitopes on multiple proteins [see Figure 1.5.2]; therefore, their exact affinity cannot be determined. The process of production of rabbit polyclonal antibodies involves preparation of antigen samples, which are later injected into the rabbit (i.e. immunization) to evoke high expression levels of antigen-specific antibodies in the serum. Usually, the procedure is divided into 5 steps: initial injection, first booster injection, second booster injection, test bleed and third booster injection [93]. Eventually, the rabbit serum is collected and antibodies are recovered by purification [94].

### 1.5.3. Secondary Goat polyclonal antibody

The goat brings about 7-8 times more serum than the rabbit. Additionally, the goat serum contains around 20 mg/ml of total IgG, which is about 2-3 times more than the rabbit serum [95]. If a goat is immunized with rabbit antibodies, it will produce secondary antibodies (in this thesis Goat anti-rabbit IgG H&L are used [see Appendix F], where IgG H&L stands for targeting Heavy and Light chains of the IgG molecule as shown in Figure 1.5.2).

Since Light Chains can be shared by different antibody classes, anti-IgG H&L can react not only with IgG, but also with other antibody classes (e.g. IgE, IgD, and IgM).

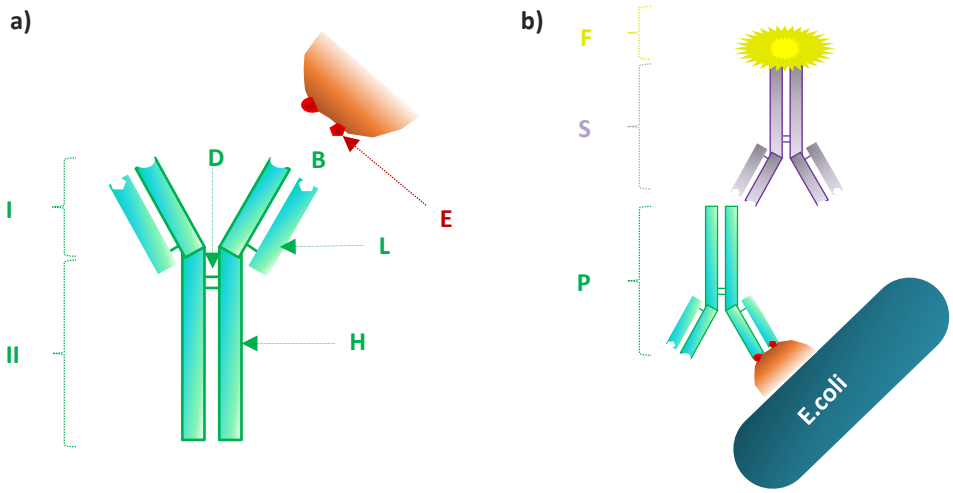


Figure 1.5.2: Antibody-Antigen binding mechanism: a) Y-shaped antibody structure with two regions; I corresponds to variable region, while II to constant region, D is the disulfide bridge, B is the binding side to antigen's epitope, L is the light chain, H is the heavy chain, E is the epitope, b) Multiple antibody-antigen arrangements, where P is the primary antibody binding to epitope protein on bacterial wall capsule, S is the secondary antibody targeting heavy and light chains of primary antibody and F is the conjugated fluorophore to secondary antibody for labelling purposes.

Since the Y-shaped IgG molecule has a random rotational orientation on the surface, its size depends on the measurement technique and can vary between $11\,nm$ [96] to $20-40\,nm$ in diameter and about $\sim 2\,nm$ in height [97].

### 1.5.4. Biotin-Streptavidin

The streptavidin-biotin binding mechanism (where ''strept'' stands for a protein SA purified by bacterium *Streptomyces avidinii* and ''biotin'' for a small $244Da$ molecule also known as B7 or H vitamin) is the strongest noncovalent interaction known in nature. Its lock-and-key coupling system can only be broken under harsh conditions (such as $pH = 4$, high temperature, salt concentration) [98]. Characterized by an affinity constant of $10^{-13}$ to $10^{-15}$ in $[L/mol]$[99], together with high specificity and robustness, SA-B complex appears as an ideal candidate for a biological linkage system. Hence, biotinylated molecules (like e.g. antibody, whose biological activity is not affected by binding of a small biotin molecule) can be specifically bound to streptavidin coated surfaces (like e.g. a streptavidin coated magnetic particle (MP)) to serve as biological markers [see Figure 1.5.3 [100]]. Biotinylation is achieved by covalently coupling the primary antibody free amine groups with the N-Hydroxysuccinimide ester of biotin under mild conditions to give a high degree of substitution.

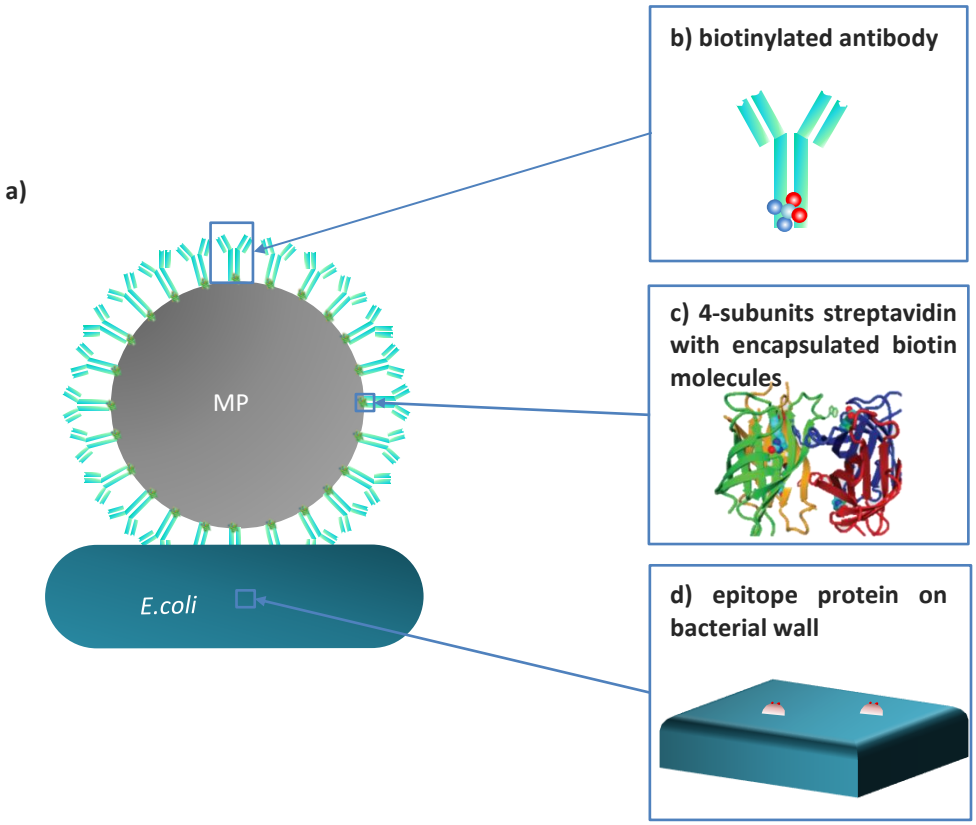


Figure 1.5.3: Schematics of E.coli capture mechanism utilizing a functionalized magnetic particle and an SA-B linkage system (unscaled); a) streptavidin coated MP with attached biotinylated antibodies and a recognized E.coli antigen; b) biotinylated antibody with usually ~3-6 biotin molecules per immunoglobulin; c) Quaternary streptavidin structure [100] composed of four protein subunits (green, yellow, red and dark blue) corresponding to four identical β-barrels together with small spherical biotin molecules that are captured inside the streptavidin; d) Surface of E.coli bacterium covered with antigenic determinants (epitopes) that are recognized by the antibodies.

# 2. System Design and Implementations

## 2.1. Working Principle

The purpose of the microfluidic platform presented in this thesis is to investigate and analyze a biological content of a sample. The system aims to detect and most importantly, to **quantify** the amount of pathogens present within a liquid sample. The proposed platform is designed in such a manner so as to be applied not only for the quantification of *E.coli* (which is tested exclusively in this thesis) but also for any other disease-causing micro-agent.

The innovative aspect of the proposed device is that it utilizes a specialized single particle tracking system that analyzes dynamics and volumetric changes of a magnetic particle after microorganisms are bound to its functionalized surface. The attachment of the microorganisms on the surface of the MPs is ensured by an appropriate biological binding protocol. The protocol efficiency is first studied by adjusting various parameters and conditions and then the finest option is selected and applied as a final binding procedure. Next, the measurements are conducted, provided that the labeling protocol is consistent (i.e. the amount of liquid, proportions, as well as handling of the sample and environmental conditions, remain unchanged). Only the desired quantity of bacteria is altered, which in turn, is expected to increase/decrease the number of attachments [see Figure 2.1.1] and affect the particle's dynamics.

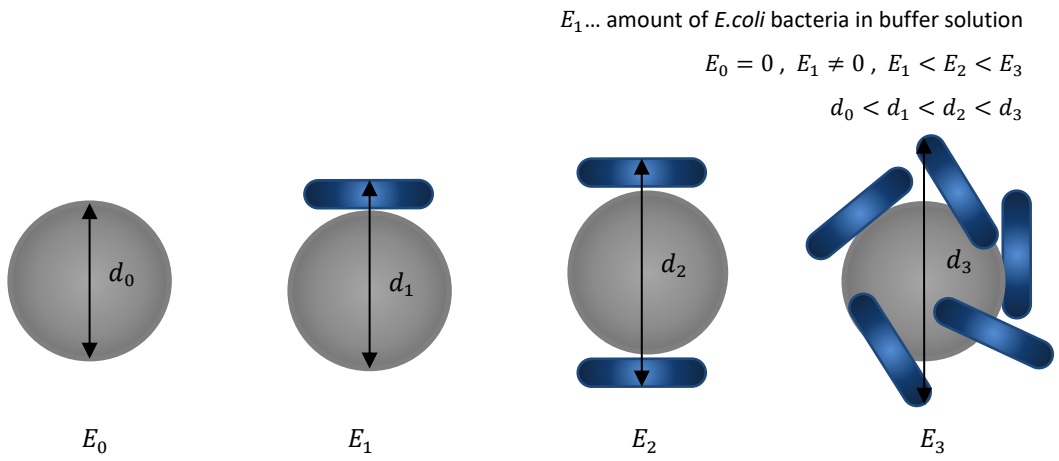


Figure 2.1.1: Schematic representation of volumetric changes of a particle after different *E.coli* attachments. The amount of the attachments depends on the amount of *E.coli* bacteria present in a buffer solution. The diameter $d_0$ corresponds to a reference diameter of a bare, unloaded MP without *E.coli* attached. The variables $d_1$, $d_2$ and $d_3$ denote the sizes of particles for which amount of *E.coli* bacteria within a buffer solution was increased.

The change in shape/volume and the resultant surface chemistry depend not only on the size/type of the attached pathogen itself but also on a formation of other layers/coating arising from an application of a binding protocol. A more detailed representation of these changes and a cross-section of a particle with coatings and various layers of a biological linkage system can be seen in Figure 2.1.2. Depending on the amount of attachment, the behavior and the dynamics of MPs suspended in a liquid would be changed. This thesis presents two methods for the investigation of particle dynamics: a direct one, by an optical investigation of a physical phenomenon commonly present in nature (Brownian motion) and an indirect one, by applying an external stimuli (a magnetic field gradient) and analysis of the particle's response to it. In the first method, dynamics are observed by means of dark field microscopy and information about the mikromarker's diameter is given. The second method utilizes fluorescence microscopy and tests the feasibility of a system to magnetically manipulate

the motion of differently loaded MPs (MPs with attached pathogens). In both cases, the liquids in which the particles are suspended are assumed to be static[26].

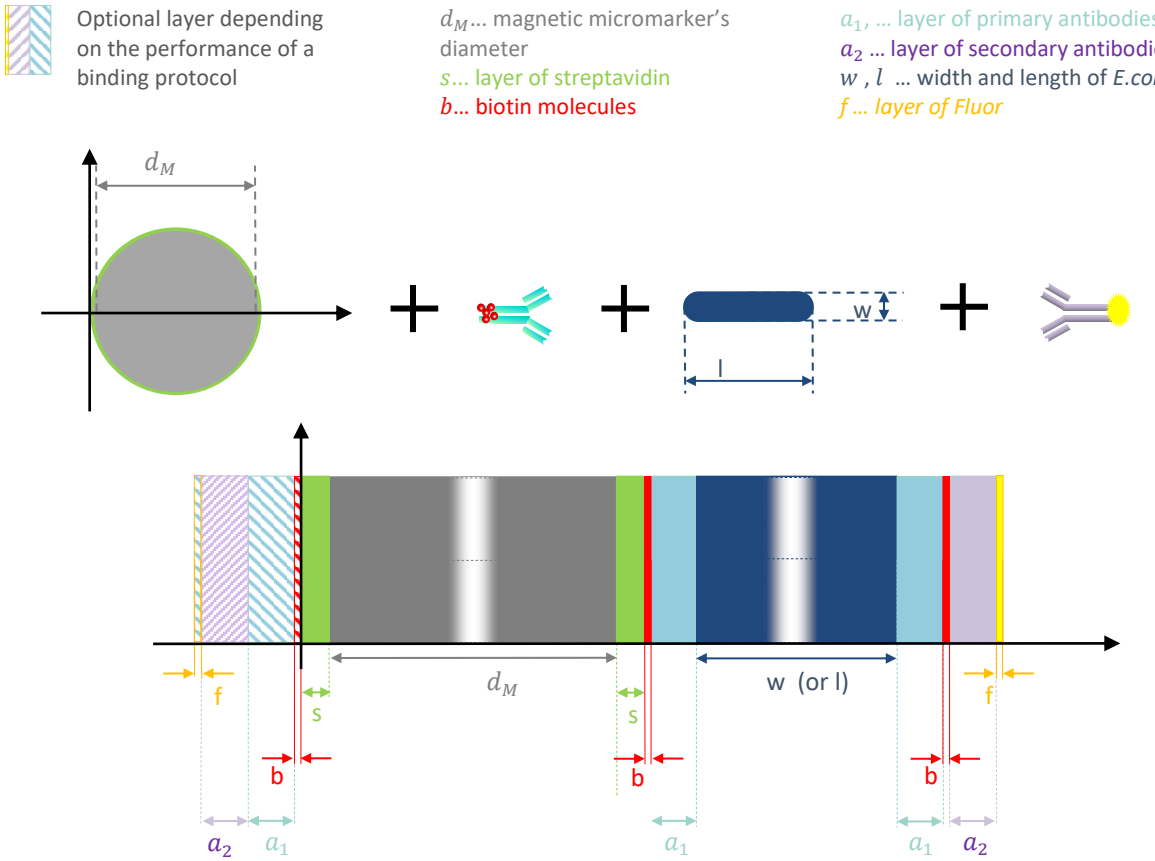


| | | Size | Description | Surface chemistry |
|---|---|---|---|---|
| **Micro-marker** | Dynabeads ™ M-280 Streptavidin | $d_M \approx 2.8\ \mu m$<br>$s \approx 105\ nm$ | Different micromarkers can be used. M-280 is covered with a monolayer (not multilayer) of streptavidin [101]. Size of streptavidin was taken from [102] | M-280 refers to hydrophobic [103] |
| | Dynabeads ™ M-270 Carboxylic Acid | $d_P \approx 2{,}8\ \mu m$ | Diameter includes also carboxylic acid layer [104] | M-270 refers to hydrophilic [103] |
| **Linkage system** | Biotinylated antibodies | $b \approx 30\ nm$ | Biotin molecules increase the size of streptavidin from 105 to 133 $nm$[102]. | Encapsulated within antibody |
| | | $a \approx\ 20\ nm$ | IgG Y-shaped antibody size is ~11 $nm$ [105] or ~20– 40 $nm$ [106] and depends on the measurement technique | Positive net charge [107] |
| **pathogen** | *E.coli* | $w \approx 0.5\ \mu m$<br>$l \approx 2\ \mu m$ | The binding side plays a role for irregular shape of pathogens | Net negative surface charge in DI water [108] |

Figure 2.1.2: Detailed representation of a change in particle size that is influenced by a coating, a biological linkage system and *E.coli* binding.

For the 1st method, it is the particle output **diffusive diameter** that defines the amount of pathogen present in the sample, while for the 2nd method it is the output **velocity** pattern.

[26] *There is an exception for y-axis in Brownian method, where sedimentation movement is observed [for a detailed explanation see Section 2.1.1].*

Particle dynamics are recorded by a camera and the trajectory of each individual particle is analyzed. This thesis tests the feasibility of the tracking software algorithm proposed in [109] in combination with a microfluidic platform as an automated and efficient data evaluation method for detection and quantification of pathogens.

Below the working principles of the two methods for the investigation of the dynamics of the particles are outlined. Both of them utilize the same biological binding protocol [see Section 2.1.4] and the same tracking software routine explained in Section 2.1.3. For the 2nd quantification method, the tracking procedure is extended with additional MATLAB scripts that are depicted in Appendix C.

### 2.1.1. 1st quantification method: combined dark field microscopy and Brownian motion

As previously mentioned in Section 1.3, the particles suspended in liquids undergo thermal fluctuations that are commonly known as Brownian motions. In this thesis, it is possible to track these tiny motions due to an intelligible combination of scattering (dark field) phenomena and an appropriate particle tracking system.

To follow the dynamic processes and interactions within a liquid sample the subsequent frames from camera's recordings are collected and analyzed. The camera's image exposure rate is selected in a way to capture differences in scattering between consecutive frames without disruptive motion blurring[27] (for more details about camera shutter speed and movie decomposition procedure see Section 2.1.3), which is of importance when applying particle tracking algorithm.

Provided that the particles are suspended in a static fluid where viscosity and temperature do not change over time and the same environmental conditions are kept for all sets of measurements, the diameters of the particles suspended in a fluid can be determined for each sample sets (FOVs) and compared. Variations in the micromarker's shape/diameter arise from the binding of biomolecules to its functionalized surface [see Figure 2.1.2]. Larger particles will collide more likely and more often with the surrounding buffer molecules whereas smaller particles will move more freely within the liquid. This results in a decreased MSD [see equation (1.3.7)] within a defined time interval $t$ for larger molecules and an increased MSD for smaller ones, respectively.

The extent of a particle's Brownian motion, according to Stokes-Einstein equation (1.3.3), is characterized by a diffusion coefficient $D$, which is dependent not only on a particle radius $r_s$ (i.e. output variable of an interest), but also on other variables like temperature $T$ and viscosity $\eta$ of a fluid. These two parameters are kept constant within measurements conducted in this thesis.

A schematic representation of the trajectory of Brownian motion of an individual particle together with a graphical explanation of MSD [see equation (1.3.6)] can be seen in Figure 2.1.3. In this thesis, the proposed system is capable of tracking multiple trajectories simultaneously from various FOVs and from different liquid samples.

Figure 2.1.3 represents the schematic trajectory of an individual particle suspended in a static fluid, where no motion is induced. In this thesis, however, the biological liquid containing the pathogen-loaded-micromarkers, is entrapped in a sample cell which is positioned **vertically** to the microscope stage. Such arrangement was introduced to avoid unwanted attachments of biological agents (i.e. attachment of *E.coli*/antibodies from the MP-*E.coli* complex) to a glass slide [for more details see Section 1.1.3].

Due to this vertical arrangement, Brownian motions are now appended with gravitational movements along the y-axis. Therefore, a displacement along the y-axis serves as a reference trajectory while the x-component of the calculated hydro-dynamic diameter $d_x$ of a hypothetical sphere corresponds to a diameter of a particle under investigation. In other words, in this thesis, in a 2D particle tracking system, only the horizontal component $d_x$ (diffusive diameter $d_p$ along the x-axis) is calculated as there is a strong sedimentation movement along the

[27] *Blurring is an artefact that depends on the exposure time defined by the camera shutter speed. With increasing blurring artefact, the contrast in intensity at the edges of particles decreases.*

vertical y-axis that overrides the Brownian motion. Therefore, in order to calculate Brownian MSD, y-components are excluded and the equation (1.3.6) takes the form:

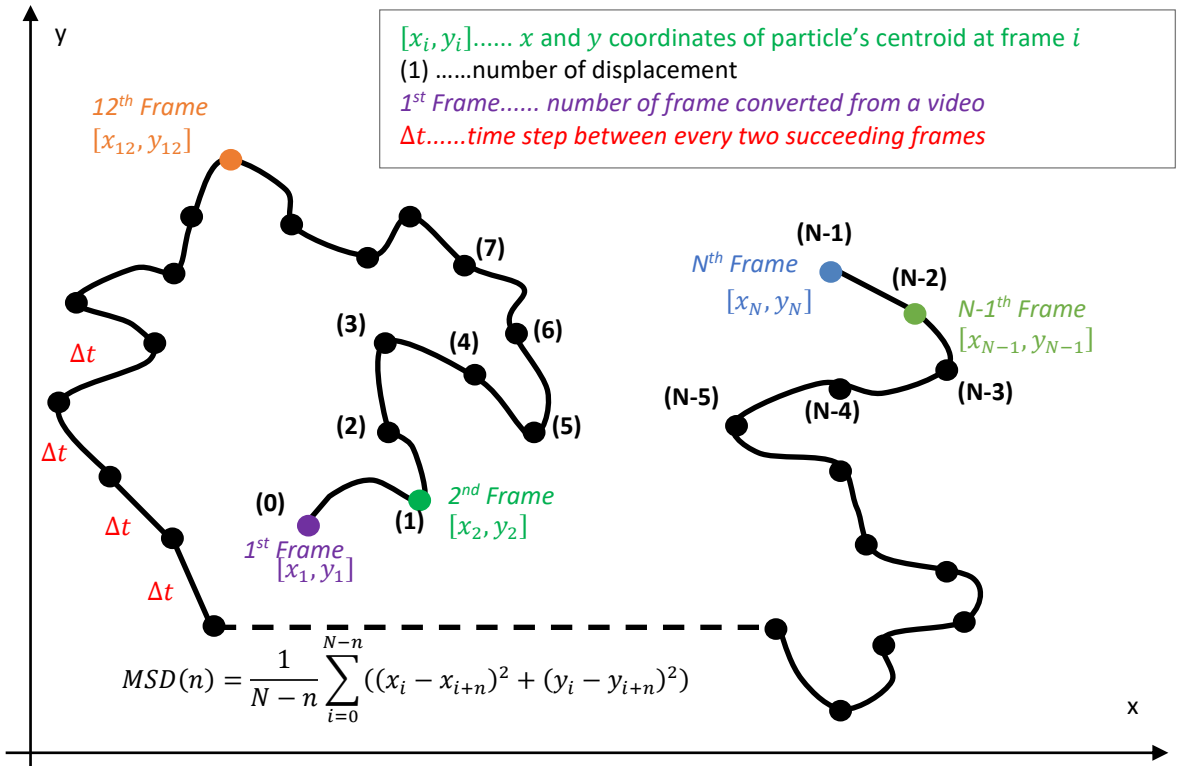


Figure 2.1.3: Principle of an MSD calculation from a schematic representation of 2D trajectory of an individual particle undergoing Brownian motion. Time interval $\Delta t$ between each succeeding frame $i = 1, \dots N$ stays unchanged, while $x_i$ and $y_i$ coordinates correspond to a variable position of the particle's centroid captured at a specific frame $i$.

$$MSD(n) = \frac{1}{N-n}\sum_{i=0}^{N-n}(x_i - x_{i+n})^2 \qquad (2.1.1)$$

The variable $DIM$ from the equation (1.3.2) is changed from 2 to 1 ($DIM = 1$) and thus the equation (1.3.7) is rewritten as:

$$d_p = \frac{k_B T}{6\pi\eta} \cdot \frac{4n\Delta t}{MSD(n)} \qquad (2.1.2)$$

where $d_p$ is now the diffusive diameter $d_x$ along the x-axis[28].
It should be noted however that the tracking (not the diameter calculations) of the particle trajectory along the y-axis is still kept. The working principle of the trajectory tracking procedure is explained in Section 2.1.3.

### 2.1.2. 2nd quantification method: combined magnetophoresis and fluorescence microscopy

The pathogen quantification principle is based on the decreased MP's velocity due to inhibiting factors such as Stokes' drag force and altered hydrodynamic shape of the MP after the pathogen is attached to it. In this thesis, the developed microfluidic platform with integrated microconductors (MCs) and a PDMS channel is used to manipulate the motion of MPs. The microfluidic channel is filled with the liquid of interest (each liquid containing differently loaded MPs) and experiments are conducted provided that the suspension liquid is static ($u = 0$ ). By controlling the DC current within the microconductors (switching it ON and OFF), a magnetic field gradient at each conductor at a time is created and the MP is set in motion. Once the magnetic particle reaches the position

[28] *Take into account that equation (1.3.7) defines a radius $(r_s)$ while (2.1.2) defines a diameter $(d_p = 2r_s)$*

where the magnetic field is at its highest (i.e. it is captured on the conductor where $I \neq 0$ ), the current is switched off. This procedure is repeated for each adjacent MC and continues until the MP travels the entire distance from the right (MC 1) to the left (MC 9) of the chip as seen in Figure 2.1.4.

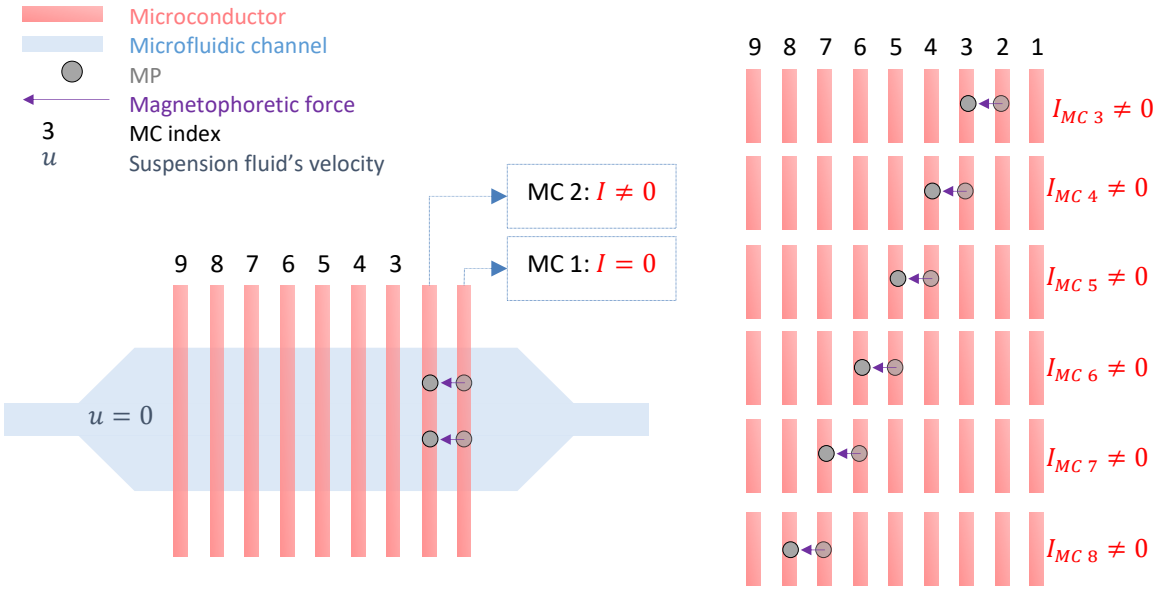


Figure 2.1.4: Schematic of the developed platform with integrated microconductors (MCs) and the microfluidic channel. An MP is manipulated from the right to the left by switching the current ON and OFF on adjacent MCs. The magnetic force is always directed along the gradient of the magnetic field (i.e. toward the MC where $I \neq 0$).

The operating principle of magnetophoresis is that the movement of a magnetic particle within a viscous fluid is determined by magnetic $F_m$ [see equation (1.2.5)], gravitational $F_g$ and drag $F_d$ [see equation (1.2.6) ] forces. The arrangement of these forces in this thesis' system is presented in Figure 2.1.5 A. The inertial forces are neglected[29] and the force balance equation is [110]:

$$F_m + F_g + F_d = 0 \tag{2.1.3}$$

Here the electrostatic DLVO force is a counterforce to the gravitational and y-component of the magnetophoretic $F_m$ forces. Therefore, the migration velocity $v_P$ of the single MP-*E.coli* complex, after combining equation (1.2.5), (1.2.6) and (2.1.3), can be written as:

$$v_P = \frac{V_{MP}\Delta\chi_v}{3\pi\eta d\mu_0}(\vec{B}\cdot\nabla)B \tag{2.1.4}$$

where $\vec{B}$ is the magnetic induction field, $V_{MP}$ is the volume of the magnetic particle, $\Delta\chi_v$ is the difference between volumetric magnetic susceptibility of the magnetic particle $\chi_{v_{MP}}$ and the surrounding fluid media $\chi_{v_{fluid}}$ , $\eta$ is the viscosity of the liquid, $d$ is the diameter of the MP together with the loading and $\mu_0$ is the magnetic permeability in free space. As seen from the above equation, the motion of the particle scales differently with the particle size and shape [111].

The behavior and dynamics of differently loaded MPs are observed with a video fluorescence microscope. Tagged *E.coli* bacteria are labeled with Fluor according to the procedure described in Binding Protocol. The recorded video is converted to grayscaled frames. The principle of software tracking of MPs trajectories is described in 2.1.3.

[29] $Re \ll 1$ *[see Section 1.1.1]*

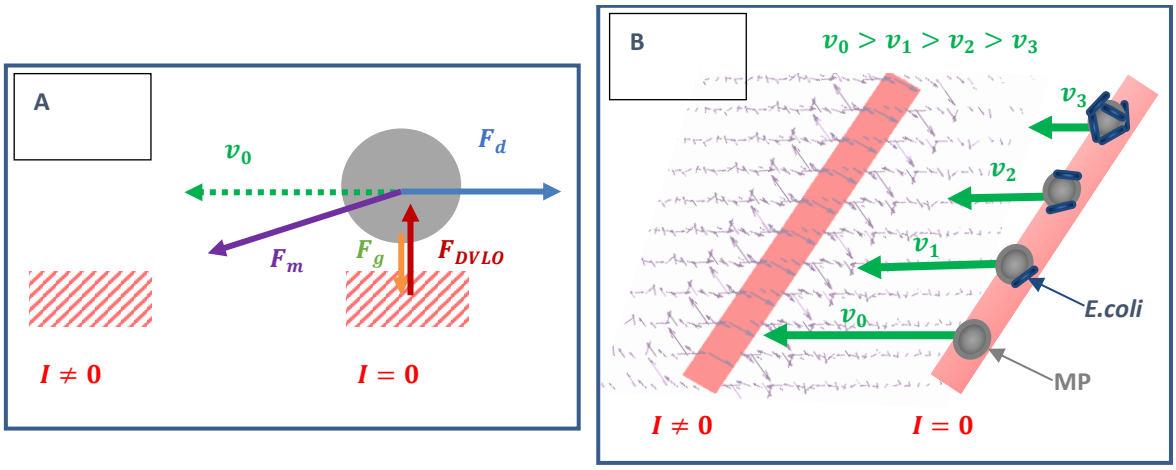


Figure 2.1.5: Working principle of magnetophoresis of MP suspended in fluid. The motion of MP arises due to the magnetic field gradient that is created by the left microconductor ($I \neq 0$). Picture A represents the forces acting on an individual MP. Picture B represents differently sized MP-*E.coli* complexes with various migration velocities $v$. The fluid in which MPs are suspended is static ($u = 0$). Their motion depends on the amount of *E.coli* attachment.

### 2.1.3. Particle Tracking Principle

In this thesis, a MATLAB script utilizing 2D particle tracking Crocker-Grier[30] algorithm [112] is used to link the exact position (centroids) of objects appearing over subsequent frames [113] [114]. Based on this approach, a single frame $i$ ($i = 1, \dots, N$) is processed to detect multiple bright spots (representing particles) over a dark background (here the variability in pixel intensity is used to 'find' a particle) [see Figure 2.1.6 (b)]. This procedure is repeated (for all the frames; $N$ is the total number of all frames) giving $x_i$- and $y_i$-coordinates (of each individual particle's centroid for each frame), which are then linked together to form trajectories [115].

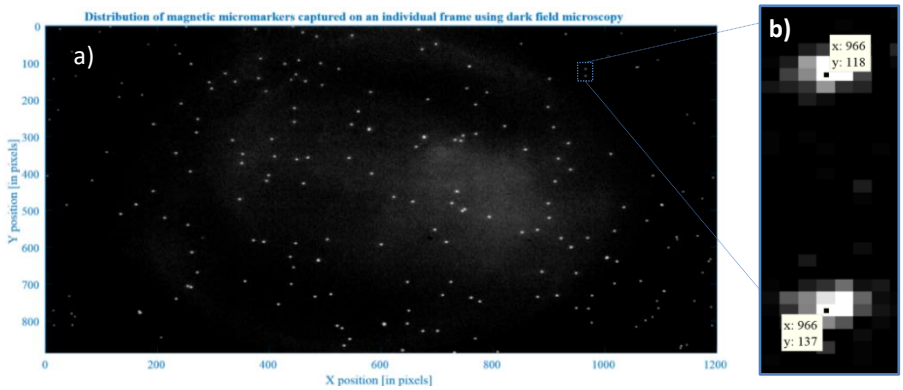


Figure 2.1.6: Magnetic micromarkers appear as bright spots on a dark background image. a) Multiple microparticles captured on a single frame $i$ and b) zoom in for two particles with assigned centroids- To each particle and for every frame, $x_i$ and $y_i$ coordinates of particles centroid are calculated.

Once particles are detected and their positions are known (for an entire sequence of video images), their locations are matched with successive and proceeding frames (i.e. it is determined which particle in a given frame most likely corresponds to the particle in the preceding frame). In order to avoid linking errors, parameters such as threshold, mask, noise length, object length, linking distance, minimum trajectory length [see Section below] must be properly adapted (i.e. while changing the magnification of an optical system or when using differently sized (magnetic)-micromarkers these parameters must be checked again).

[30] *Named after J. Crocker and D. Grier who described sets of image processing for video microscopy.*

### *Software Tracking Procedure/Routine*

During recordings of a particles' dynamics, an important parameter is the camera shutter speed. It defines a time step $\Delta t$ between successive frames. This parameter is given in frames per seconds (fps). To obtain sequence of video frames from a video (**converting** $.mov$ into $.jpg$), input parameters such as 'Start' and 'Stop' output frames (introduced to get frames only from desired cutoff from a video), frame output color and format are defined.

Next, after selecting the desired output frames for further analysis (combination of frames converted from multiple videos is also possible), a preview is provided [see Figure 2.1.7] to enable adjusting of parameters for a **detection procedure**.

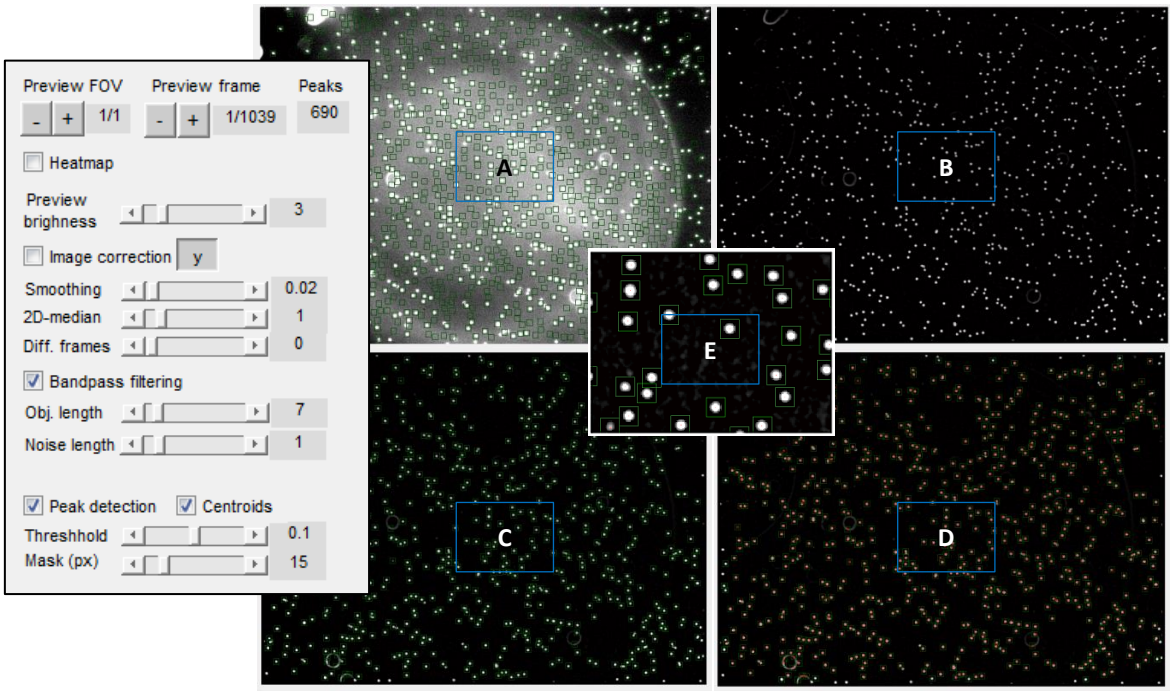


Figure 2.1.7: GUI enabling preview of selected frame for proper configuration of detection parameters. This particular frame was taken from a video that recorded Brownian motion of unloaded Dynabeads™ M-270 Carboxylic Acid. There are 690 particles detected on this frame. A is an original video frame before noise removal (before applying bandpass filtering), B is an image with increased brightness, C shows a preview with detected particles (embedded in green squared mask), D is the preview of the image with visible particles 'centroids (multiple red points. Regular spherical shapes of particles can be seen on zoomed picture E.

Proper adjustment of parameters highlighted in Figure 2.1.7 in the GUI box on the left, is crucial when recognizing MP-*E.coli* complex as one, single complex [see Figure 2.1.8 B] and not as two separate particles [see Figure 2.1.8 A]. At the same time, parameters should be chosen so that two neighboring micromarkers are recognized as separate [see Figure 2.1.8 C, D].

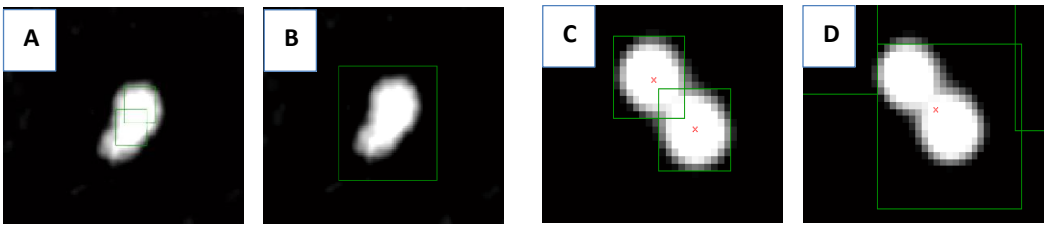


Figure 2.1.8: Particle detection and MP-*E.coli* complex recognition depends on proper adjustment of detection parameters. Pictures A and B represent a loaded MP (LMP). Pictures C and D represent unloaded MPs: In A, LMP is recognized as two separate objects (MP and *E.coli* are recognized separately) while in picture B the complex is identified as a whole. In picture C two neighboring particles are distinguished as separate objects, on D they are marked as one. Proper adjustment of parameters must be done to obtain reliable results.

Apart from the detection parameters, other user-defined variables must be set to specify the linking procedure. The most relevant parameters are highlighted in Figure 2.1.9 and are listed below:

- minimum and maximum size are introduced to specify the size range of particles whose trajectories are further analyzed (i.e. micromarker size range)
- minimum trajectory length - some of the particles at the border of the frames move outside the FOV or disappear due to photobleaching. This parameter defines the percent of frames for which particle is still tracked
- resolution - enable conversion of pixel units into real dimensions in micrometers. It is determined according to the procedure described in section 2.2.1. Resolution for 1st (Brownian) analysis must be defined in the dialog box from Figure 2.1.9, while for the 2nd (magnetophoresis) method information about resolution must be provided while executing the additional scripts and calculations (see Appendix C)
- time step $\Delta t$ or exposure time [in seconds] - is the time between two consequitive frames and is given by the camera shutter speed (for $25 fps$ $\Delta t = 0.04\ sec$)
- temperature and viscosity – variables which must be known before calculating the diffusive diameter from MSD [see equation (2.1.2)]
- minimum and maximum velocity - introduced in to avoid the analysis of unwanted particles (e.g. foreign objects/dirt which experience different motion than the particles of interest)
- linking distance – depends on the magnification of the optical system and size of a particle. It is a distance [in pixels] which a particle travels within time step $\Delta t$ . It is used to link positions of an individual particle between two consecutive frames. The larger the Brownian motion or the bigger the magnification, then the bigger the linking distance is.
- Different values for resolution, linking distance, minimum trajectory length as well as threshold, mask, object and noise length (left GUI box on Figure 2.1.7 ) must be set according to the type of the method used.

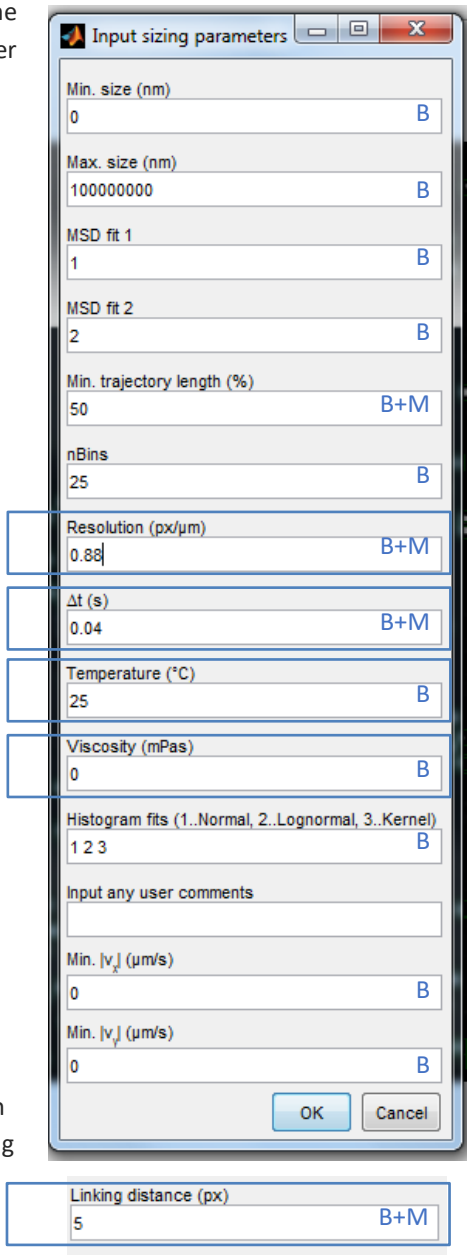


Figure 2.1.9: Input sizing parameter for linking procedure and MSD calculations.
B - parameters relevant in 1st (Brownian) quantification method;
M - parameters relevant in the 2nd (Magnetophoresis) quantification method

Figure 2.1.9 presents the screenshot of the values used in the 1st (B - Brownian) method. The linking values in the 2nd (M-Magnetophoresis) method are:

$$Min.trajectory\ length\ = 5\ \%$$
$$Linking\ distance = 25\ pixels$$
$$Resolution\ \approx 7.2\ pixels/\mu m\ \ \text{[for calculations see section 2.2.1]}$$

### 2.1.4. Binding Protocole

Another objective of this thesis is to investigate the efficiency of the biological binding protocol and to establish which parameters/activities significantly influence the quality of the attachments. Here, the objective is to determine whether the procedure described in Appendix D could also be applied for varying *E.coli* concentration and to establish if the amount of resultant attachment is related to the amount of *E.coli* originally suspended within a buffer solution.

Concentrations of antibodies/ *E.coli*/ MPs within buffer solution are altered. Additionally, the attempt to break/avoid agglomeration is performed. The procedure with the most satisfying results is validated.

## 2.2. Calculations

### 2.2.1. Resolution chart

The resolution for both optical systems (Brownian and Magnetophoresis) was determined with '1951 USAF Resolution Negative Test Targets, 3" x 3" [see Figure 2.2.1 ]. This subsection presents exemplary calculations for the resolution of the 2nd (magnetophoresis) optical system.

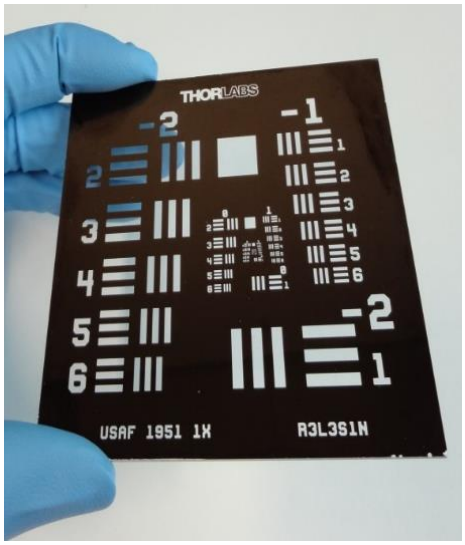


Figure 2.2.1: Negative 1951 USAF Resolution Test Targets 3" x 3" uses chrome coating with transparent pattern having high edge definition and contrast ratio. There are 3 bars within each element of a group displaced according to Ronchi grating rule.

The resolution test chart was placed on the microscope stage with adequate objective ($60\times$ magnification for magnetophoresis) and video recordings with the frame rate of $25fps$ and resolution $1920\times1080$ pixels were collected. The film was re-converted (in the exact manner as in the case of magnetophoresis videos) to a sequence of individual frames.

Since the width $w$ [in $\mu m$] of each individual bar in the Resolution Test Chart is known [see lookup table in Appendix B] and elements within a group are displaced according to Ronchi grating rule[31], the resolution $R$ in [ $pixels/\mu m$] of an optical system is given by:

[31] *Within a group the widths of bars and intervals are constant. The optical target has a high edge definition.*

$$R = \left[\left(\frac{(x_2 - x_1)}{2} \cdot \frac{1}{w}\right) + \left(\frac{(x_3 - x_2)}{2} \cdot \frac{1}{w}\right)\right] / 2 \qquad (2.2.1)$$

The variables $x_1$, $x_2$ and $x_3$ correspond to the selected positions of the peaks [in pixels], where the difference in intensity between neighboring pixels is the highest [see Figure 2.2.2]. The path chosen for the calculation is parallel to the width of the bars.

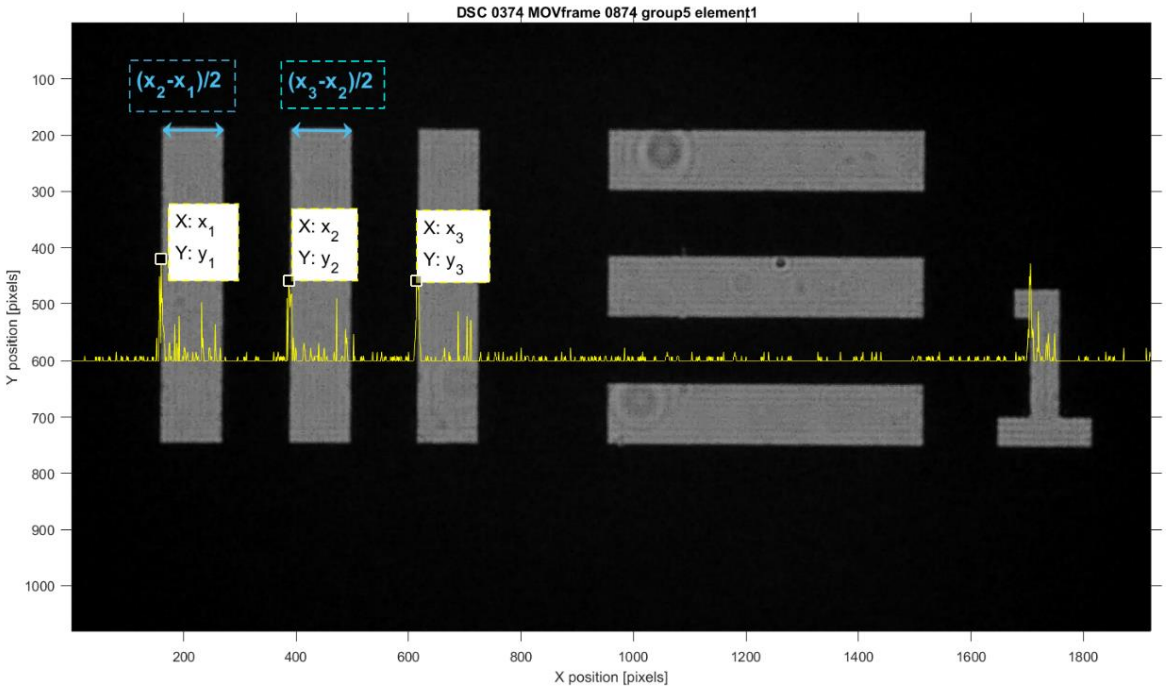


Figure 2.2.2: Selected video frame of bars from group 5 element 1 USAF resolution test chart seen under Nikon microscope 60 × objective magnification. The yellow line represents the output of the MATLAB diff(FigureName(ConstantYPosition,1:end)) function which calculates differences in intensities between neighboring pixels.

Specific outputs for $x_1$, $x_2$, $x_3$ peak coordinates can be seen on Figure 2.2.3. There are two different groups and elements (group 6 elements 2, 3 and with group 7 elements 1, 3) on one frame. The overall resolution of the magnetophoresis' optical system is 7,2 $pixels/\mu m$. It is calculated by averaging the outputs from various elements and groups. Exemplary calculations for the elements shown in Figure 2.2.3 are as follows:

Group 6 element 2: $\frac{(760-656)+(656-555)}{2} \cdot \frac{1}{2} \cdot \frac{1}{6{,}96} = 7{,}363$

Group 6 element 3: $\frac{90+93}{4} \cdot \frac{1}{6{,}2} = 7{,}379$

Group 7 element 1: $\frac{(1544-1488)+(1488-1432)}{2} \cdot \frac{1}{2 \cdot 3{,}91} = 7{,}161$

Group 7 element 3: $\frac{44+42}{4} \cdot \frac{1}{3{,}1} = 6{,}93548$

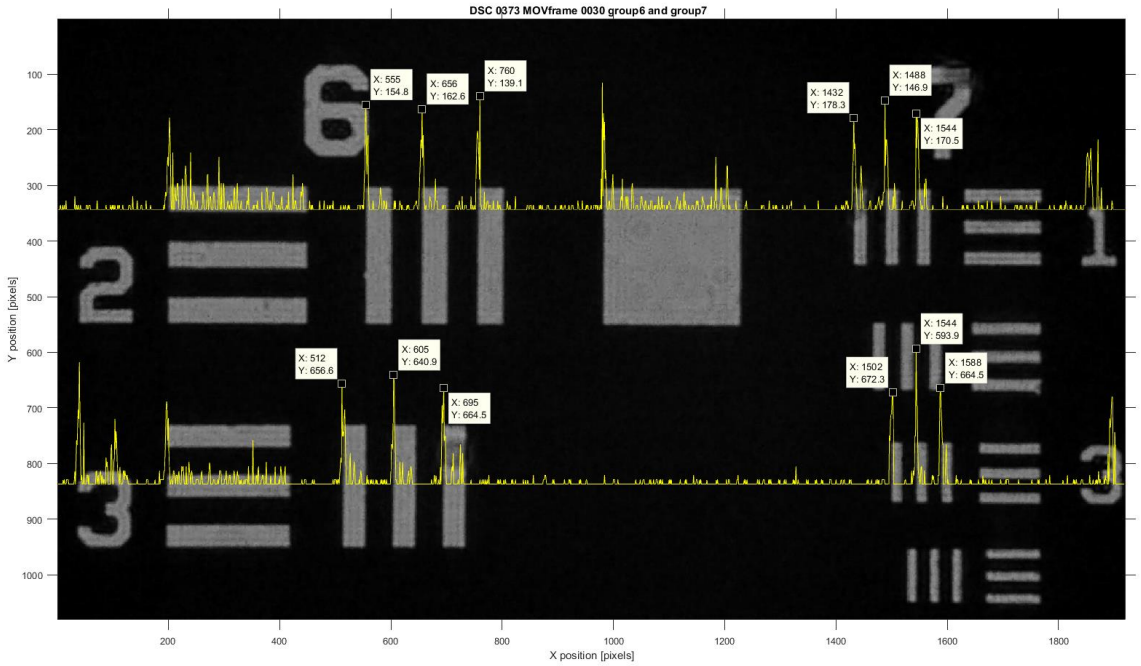


Figure 2.2.3: Selected video frame of bars from group 6 element 2,3 and group 7 element 1,3 from the USAF resolution test chart seen under Nikon microscope $60\times$ objective magnification. The yellow line represents output of the MATLAB diff(FigureName(ConstantYPosition,1:end)) function which calculates differences in intensities between neighboring pixels along the x-axis selected at constant Y. Only the positions [at pixels] of the peaks at the bar's boundary are depicted and outlined in boxplots.

Calculated in a similar manner, the overall resolution of the Brownian's optical system (1st quantification method) equals $0{,}88\ pixels/\mu m$.

### 2.2.2. Velocity calculations for magnetophoresis

To compare the dynamics of manipulated MPs, it is necessary to further process the raw data that were obtained from the tracking software routine. Additional scripts for data representation and velocity calculations were written in MATLAB [see Appendix C]. Scripts were run for each tracking attempts and particles motions' patterns were investigated and compared. Figure 2.2.4 shows exemplary displacements of one bare MP. The direction of movement is from the left to the right which can be concluded from the right-side plot. There are visible characteristic points on the trajectory that correspond to the moments when MP was captured on the MC (i.e. time intervals when the particle is not in motion $v_{MP} \approx 0$).

Similar plots were drawn for loaded MPs. The scripts nr.2-7 were written to combine the results obtained from all the measurements.

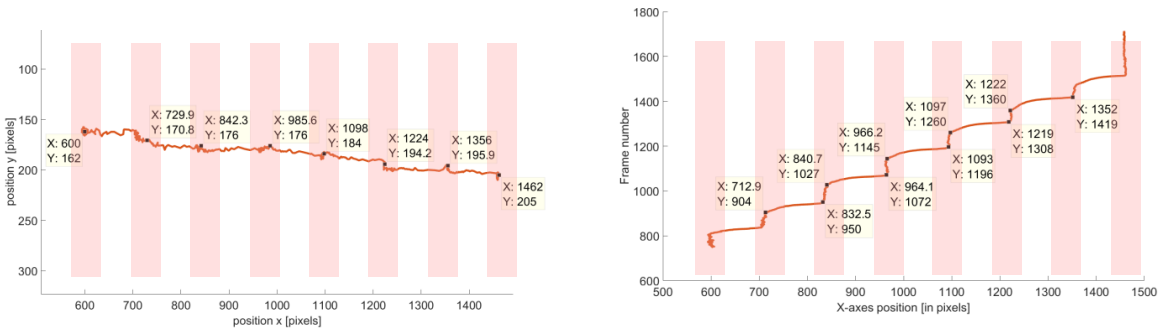


Figure 2.2.4: Method for representation of MP's motion over a sequence of frames for a single FOV). The figure on the left shows the trajectory of an individual MP with respect to x and y coordinates in [pixels]. The particle is manipulated from the most left MC to the right side. Tracking starts when the MP position is at [X:600, Y:162] and ends on [X:1462, Y:205]. There are visible changes in trajectory which indicate that MP was captured at the MC (estimated x and y positions of capture are given in data boxes). Other representation of MPs motion is shown on the figure on the right. Here the displacement in [pixels] over the sequence of succeeding frames is plotted.

## 2.3. Design Requirements and Considerations

The system's design was based on criteria such as portability, sensitivity, sample handling, costs-efficiency and biocompatibility. The system could be operated without the need for highly qualified personnel or for a demanding laboratory facility. Both platforms were designed in a way to conduct cheap, fast and specific diagnostic analysis. Since the working principle is based on the manipulation of tagged pathogens suspended in **static** fluid (without flow), neither complicated microfluidic structures nor pumping mechanisms were required. It should be mentioned that in the proposed microfluidic platform, additional functionalization (i.e. immobilization of antibodies on the chip's surface) was not needed. Therefore, the proposed system was all-embracing, multifunctional and easy to implement.

This subsection describes the design of the dark field microscopy system and the magnetophoresis based platform. The latter encloses schematics of the chip design together with the microfluidic channel's characteristics. Lastly, the additional considerations concerning surface modifications and MP's requirements are pointed out.

### 2.3.1. Dark-field microscopy system design

In this thesis, a straightforward and legible illumination technique for dark field microscopy was proposed. The sample stage was illuminated at such an angle in such a manner that the scattered light was detected by a camera, while the reflected light could not enter the optical path [see Figure 2.3.1 (a) and (b)]. As seen from Figure 2.3.1 (c) an image of bright spots (these are MPs) over a dark background was produced. The illumination system was positioned at the side of lens (epi-illumination) and accustomed in a manner to avoid unwanted saturation of camera pixels ( saturated pixels cannot provide direct information about incident irradiance [116]).The long working distance (WD) together with a low Numerical Aperture (NA) of an optical system's objective enabled broad focal depth [117][64]. Therefore a continuous observation of almost **all** the particles within a selected FOV was possible. Additionally, the long WD provided a comfortable application of the sample cell on stage and no additional coarse focusing was required if the same magnification arrangements were selected.

As previously mentioned (in Section 1.4.1) dark field microscopy requires clean working conditions. Furthermore, in order to reduce background noise scattering, smooth opaque surfaces are required. In this thesis, these conditions were sufficiently fulfilled by applying a cover glass on the top of the sample [see Figure 2.3.1 (b)].

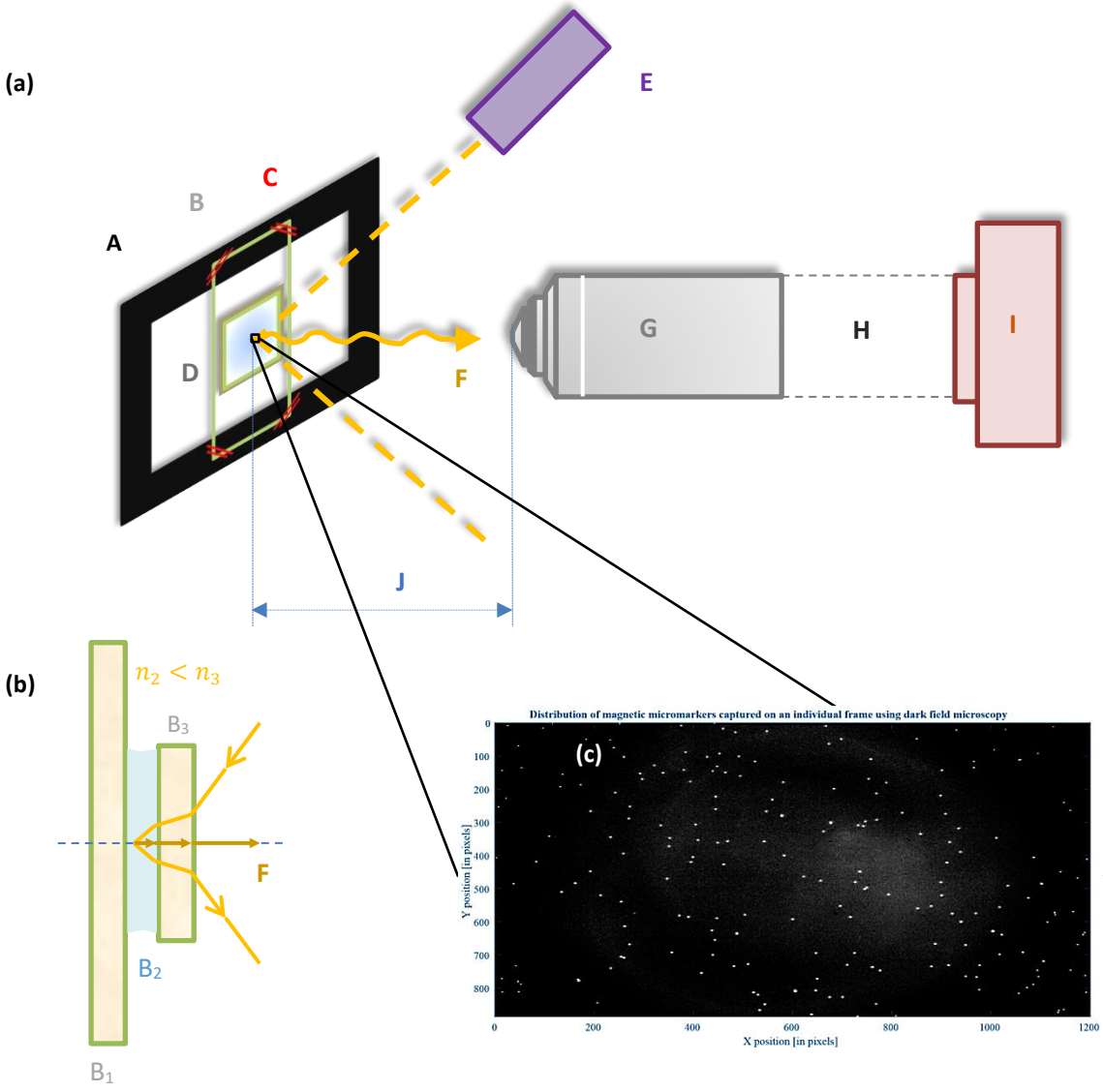


Figure 2.3.1: Dark-field video microscopy illumination system.
(a) schematic of the dark field microscopy system design where A is the vertical stage, B is the sample cell, C is the sample holder, D is the sealing of the sample cell, E is the light source, located on the same side as the objective G (Epi-illumination mode), J is the working distance of the objective, H denotes the optical train of a microscope and I is the mounted camera.
(b) cross-section of the sample cell with the entrapped liquid ($B_2$ is the biological liquid, $B_3$ is the cover glass and $B_1$ is the slide glass and n is the refractive index). The yellow lines F correspond to the simplified path of the reflected light and the light entering the objective (scattered light).
(c) represents an individual output frame image of a selected Field of View (FOV).

### 2.3.2. Chip design

An array of 9 rectangular, parallel MCs was integrated on the chip that was wire-bound to a specially designed PCB board. The chip's pads were bonded to the corresponding pads on the board (each pad was $100\ \mu m$ wide). The latter were lead to right-angle 10 pin wire-to-board connector and then through the flat ribbon cable to the experimental electronic circuit on the breadboard. On top of the chip, there was a microfluidic channel (PDMS) that was positioned perpendicularly to the MCs' array. This configuration facilitated the flow of MPs across the MCs.

The current on the MC was switched ON and OFF manually using toggle switches (which are to be replaced by an automated platform in the future). For this thesis' experiments, however, the manual manipulation is necessary since the manipulation concept itself, as well as the behavior of the MP-*E.coli* compound entrapped within the platform, had to be first analyzed. Moreover, the current and the buffer solution had to be adjusted and the performance of the tracking software for this particular method/concept had to be tested.

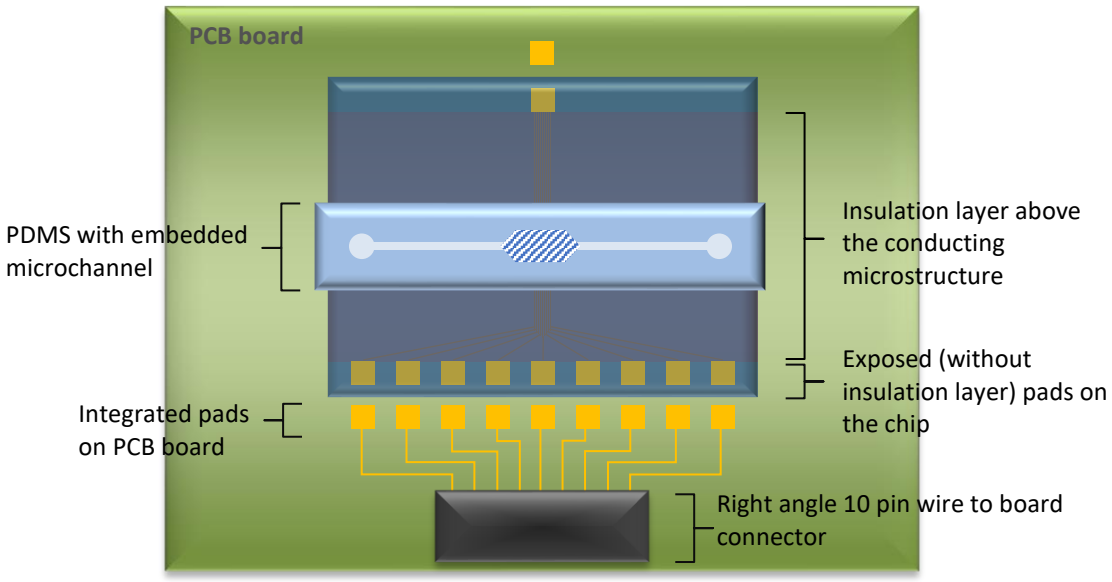


Figure 2.3.2: General idea of the platform's design

The dimensions of 9 parallel rectangular MCs were selected in a way to obtain sharp enough magnetic field gradient to be able to move MP. The height of the MC was 1 µm ($500\ nm$ of Au and $500\ nm$ of $SiO_2$) and was defined by the uniformity of the insulation layer (see red layer on Figure 2.3.3). This value had to be small enough to minimalize the unevenness on the outer surface of the chip (i.e. resulting in MCs with planar geometry). Remaining MCs' dimensions were: 10 µm in width separated by 8 µm. The simulations, as well as the explanation, why these particular values were chosen, can be found in previous works in [55]. The MCs were fabricated on a $500\ \mu m$ thick silicon wafer [see Figure 2.3.3]. The application of an insulation layer was essential since the chip's surface was in direct contact with the biological liquid. This layer however does not inhibit the bacterial bioadhesion to the chip (silicon-based materials are very susceptible to bacterial biofouling [118]). Therefore, another layer (i.e. biofilm) was additionally applied on the chip's surface [see Section 2.3.4].

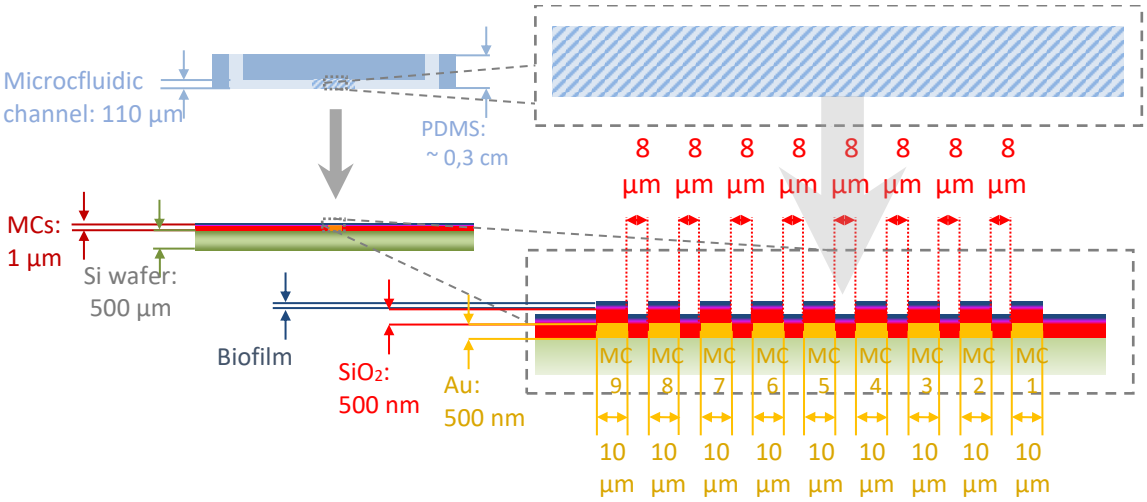


Figure 2.3.3: Schematics (not in scale) of the chip design with the integrated planar parallel MCs and their dimensions. The striped geometry corresponds to the wider part of the microfluidic channel which is in direct contact with the array of MCs and where the MPs' manipulation takes place.

### 2.3.3. Microchannel design

PDMS was chosen for the microfluidic channel for its transparency, which was an essential requirement for the optical microscope monitoring and software tracking. Moreover, PDMS was biocompatible and adhered to the chip's surface without slipping and in a reversible manner. Due to its elasticity and inertness, the channel's structure remained undamaged when applied on or removed from the chip. Therefore, this material could be used multiple times provided that any contaminants were cleaned after each operation.

The dimensions of the microfluidic channel [see Figure 2.3.4] were selected in a way to be large enough to diminish the influence of unwanted factors. That is, to ignore the effects of interfacial flow turbulences due to the chemistry and the hydrophobicity of the channel's wall. Moreover, the channel's dimensions were adjusted to study the dynamics of multiple MPs simultaneously.

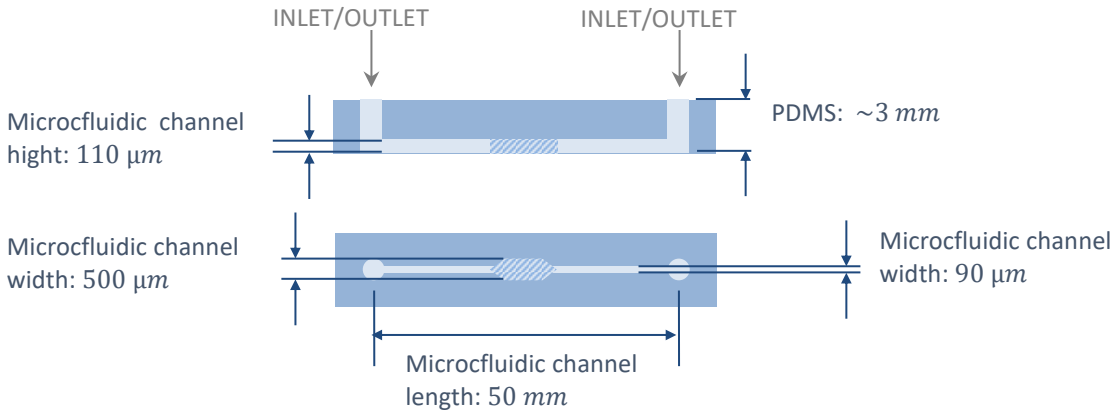


Figure 2.3.4: Schematic design of the microfluidic channel (light blue) molded in PDMS (darker blue) with the corresponding dimensions and the area for the manipulation (striped region). The channel is symmetric and therefore the injection of fluid from both sides of the channel is possible. It is applied on the surface of the chip in such a way that the microfluidic channel is on the bottom and in direct contact with the chip's outermost sodium alginate layer.

### 2.3.4. Surface chemistry

Surface modification was necessary to avert unwanted cell (or protein) interactions (e.g. adhesion) at the chip's surface. One of the strategies to fight against the adhesion of the bacteria was to apply a chemical modification on the chip with outermost Sodium Alginate (SA) layer. 'SA exhibit a 'brush like repulsive structure' that keeps bacteria apart [119].

Polyethylenimine (PEI) together with sodium alginate (SA) is layered over the insulation layer based on the layer-by-layer (LBL) electrostatic self-assembly (ESA). Treated with oxygen plasma [see 'surface modification' in section 3.1.1], the $SiO_2$ passivation layer becomes negatively charged, which enables attraction of positively charged PEI. The latter one due to the cationic character attracts anionic SA.

This modification applies only to the surface of the chip. The PDMS channel does not have to undergo this process since: a) MPs are not in close contact with the microfluidic channel walls and b) the material has an intrinsic high hydrophobicity that results in inhibition of bacterial adhesion itself.

### 2.3.5. Other utilities/additional considerations

The magnetic micromarkers utilized in this thesis' methods must have superparamagnetic properties. This enables manipulation of the multiple MPs that are smoothly resuspended within the buffer solution and prevents the unwanted aggregation. Apart from superparamagnetic properties, the MPs used in this thesis were selected based on the performance of the binding mechanism to the pathogen.

# 3. Platform development and characterization

This section covers the description of the experimental 'hands-on' procedures together with the findings.

Firstly, the steps involved in the fabrication of the platform components are outlined. Then, the instruments and materials encompassing the experimental setup are presented. Lastly, the research results and the graphical representation of the output tracking routine are demonstrated and discussed.

## 3.1. Fabrication

In order to evaluate the performance and validate the working principle [see Section 2.1.2] of the magnetophoresis, two platform components were fabricated in the ISAS' clean room: a chip with MCs and a microfluidic channel. The optimal methods for the fabrication were selected. For the channel, soft lithography was chosen due to its simplicity, cost-effectiveness and availability, whereas the conductive microstructures were fabricated with the thermal evaporation and lithographic methods. In this section, the step by step fabrication procedure together with the description of the enclosed techniques is explained.

For the 1st quantification method- Brownian approach- due to the already mentioned simplicity of the system design, no additional fabrication procedure was required. For the materials used in this method see section 3.2.1.

### 3.1.1. Conductive microstructures

The processes for the fabrication of the MCs are presented in Figure 3.1.1. The procedure is described below.

A silicon wafer served as the bottom substrate (step 1) on which a negative photoresist was spin coated[32] (step 2). The type of photoresist used was the 'image reversal[33] photoresist AZ5214' intended for lift-off-techniques. Next, Aquatar (anti-reflecting coating) was spin-coated onto the resist film. The photoresist was exposed to UV light through the 1st mask (step 3) and reversed baked. This treatment caused a reaction that resulted in cross-linking the exposed areas while unexposed areas remained photoactive (step 4). The second (flood) exposure without the mask was prepared (step 5) and photoactive areas were dissolved in developer (step 6). Then, Au (gold) film layer was deposited all over the surface by thermal evaporation[34] (step 7). The unwanted parts were removed by lifting the remaining photoresist off (step 8).

On the resulting microstructure, the insulating layer $SiO_2$ was formed by the means of Plasma Enhanced Chemical Vapor Deposition (PECVD) [35] (step 9). Here, the positive photoresist AZ6624 and Aquatar were spin coated (step 10). The structure was exposed through the mask (2nd mask) (step 11) (step 12). The exposed parts of the photoresist were dissolved (step 13). Afterwards, part of the passivation $SiO_2$ layer was removed by

[32] *Spin coating is a chemical thin film deposition technique where photoresist is centrifugally spread over the wafer.*
[33] *Image reversal relates to **reversal baking** that cross-linked the exposed areas while unexposed areas remain photoactive. Therefore, under the second (flood) exposure without the mask, these photoactive areas will undergo further chemical reactions.*
[34] *Thermal evaporation is physical deposition technique where hot source material evaporates and condenses on the substrate (i.e. chip's surface).*
[35] *Plasma enhanced chemical vapor deposition (PECVD) is a thin film deposition technique where gaseous $SiO_2$ (silane and oxygen precursor gases) is deposited to a solid state onto the new surface.*

oxygen etching[36] (step 14). The remaining photoresist was stripped (step 15). As a result, the structure, consisting of the insulated MCs and the uninsulated pads, was obtained.

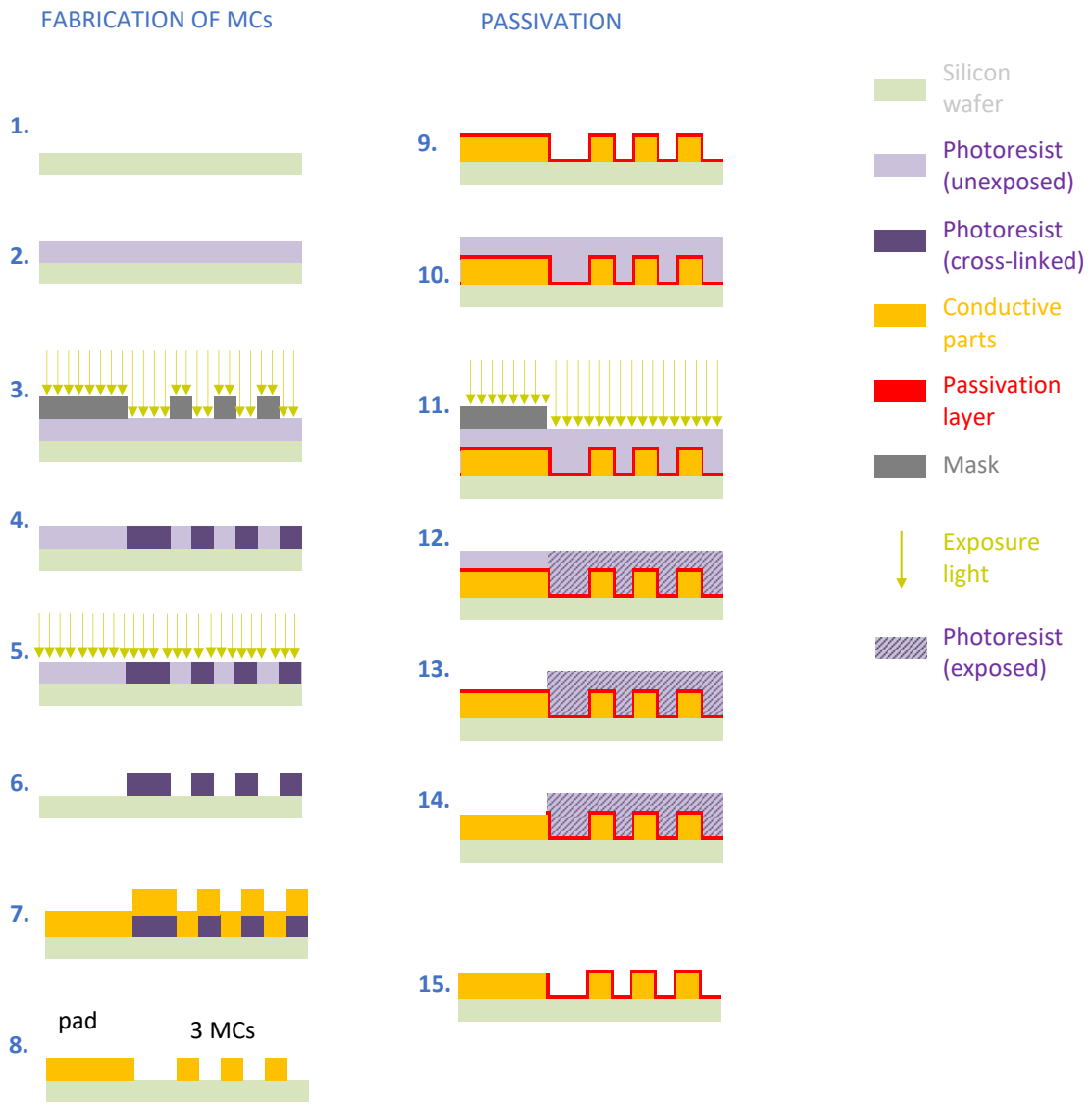


Figure 3.1.1: Step by step procedure of the fabrication of the conducting microstructures. The steps 1-7 on the left side correspond to the fabrication of the MCs and the pads, while the steps 8-14 describe the formation of the insulation layer on the MCs only. The following steps correspond to: 1. The bulk silicon, 2. Photoresist spin coating, 3. Photoresist exposure 4. Photoresist cross-linking, 5. Second exposure, 6. Photoresist removal, 7. Gold thermal evaporation, 8. Striping of the photoresist, 9. $SiO_2$ PECVD, 10. Photoresist spin coating, 11. Photoresist exposure, 12. Photoresist development, 13. Removal of the unexposed photoresist, 14. Oxygen plasma etching of the unwanted areas of the passivation layer, 14. Striping of the photoresist.

[36] *Oxygen etch is a processing used to modify properties of a surface. During the process, oxygen reacts with the elements from the surface of the material creating volatile etch products. As a result the outer layer of the material is etched.*

*Surface modification*

The fabricated microstructure was additionally surface modified to prevent biofouling[37]. Here, the surface was functionalized by means of plasma etching which improves adhesion properties prior to coating (i.e. oxygen plasma encourages hydroxylation[38] [120] which allows binding of the next layer via reactive $-OH$ groups). In order to complete a surface modification step [see Figure 3.1.2], the chip was:

1. Rinsed with acetone, isopropanol and DI water to remove contaminants
2. Dried for $30\ min$ at $150°C$ at a hot plate
3. Oxygen Plasma etching[39] (here hydroxylation of the $SiO_2$ passivation layer took place).
4. Dipped for $10\ min$ in the branched, polyethylenimine (PEI) $2\ gL^{-1}$ solution that served as an adhesion promoter and rinsed with DI water.
5. Dipped in sodium alginate also for $10\ min$ $2\ gL^{-1}$ , rinsed in DI water and dried carefully with Nitrogen.

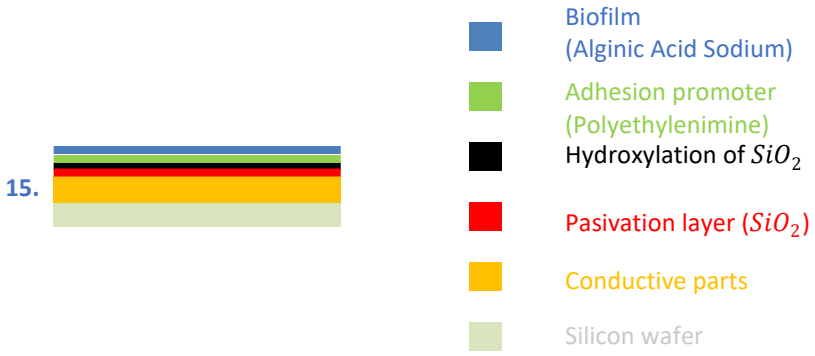


Figure 3.1.2: Schematic representation of the chip's surface modification. The outer most layer is a sodium alginate biofilm which was adhered with the help of adhesion promoter (polyethylenimine) after the $SiO_2$ hydroxylation took place.

In this thesis, the measurements were conducted using two chips. Both of them had the same surface modification.

### 3.1.2. Microfluidic channel

The fabrication process of the microfluidic channel is presented in Figure 3.1.3. It is a commonly used soft lithography fabrication method for PDMS channels. The steps are described below.

On a glass wafer substrate (step 1) the negative[40] type dry film photoresist ('Ordyl SY300') was laminated (step 2). The mask was aligned and the light-sensitive material was exposed to the UV light (step 3). The exposed areas of the photoresist were hardened while the unexposed were dissolved in Ordyl SY developer (step 4) and removed (step 5). The obtained structure served as a mold (step 6) on which liquid PDMS was slowly poured (step 7). This viscous mixture was composed of 10 base units ('Sylgard 184') and 1 unit of a curing agent and it was hardened by heating at $70°C$ for 1h on the hot plate. The obtained elastomeric PDMS channel was slowly pulled off (step 8) from the mold. Lastly, the PDMS material was punched with beetles (step 9) in order to provide access to the channel (i.e. inlet and outlet) for the sample injection.

[37] *Biofouling is an accumulation of microorganisms on wetted surfaces.*
[38] *Hydroxylation is a chemical, oxidative process that introduces a hydroxyl group (-OH) into a compound.*
[39] *Oxygen plasma etching removes surface organic leftovers and also promotes the formation of a uniform and stable coverage of –OH on the $SiO_2$ layer.*
[40] ***Negative** photoresist is a type of photoresist whose unexposed areas are dissolved in the photoresist developer.*

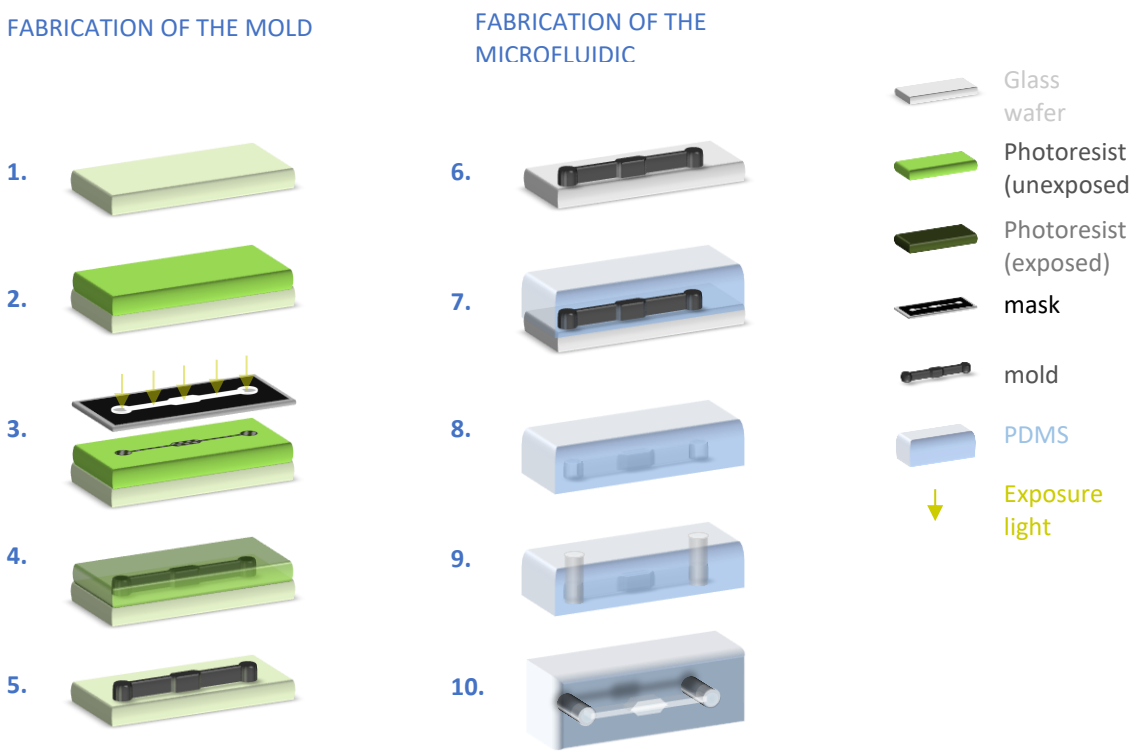


Figure 3.1.3: The microfluidic channel's fabrication using soft-lithography. Steps 1-5 (on the left) show the fabrication of the desired mold. This mold is later used in steps 6-8 to obtain the desired geometry within the PDMS material. The steps correspond to: 1. The bulk silicon wafer, 2. The lamination of the photoresist, 3. The photoresist exposure with the mask, 4. The photoresist development, 5. The removal of the unexposed photoresist, 6. The mold structure on the bulk wafer, 7. The PDMS pouring and hardening, 8. The PDMS peeling, 9. The Inlet and Outlet drilling, 10. Rotated view of the PDMS channel for visualization purposes

In order to create many PDMS channels simultaneously, a multiple molds' arrangement, as seen in Figure 3.1.4, was proposed. The bottom of the polypropylene square petri dish served as the bottom substrate for the fabrication of molds. The desired amount of the PDMS was slowly poured into the container to get the desired height of the channel.

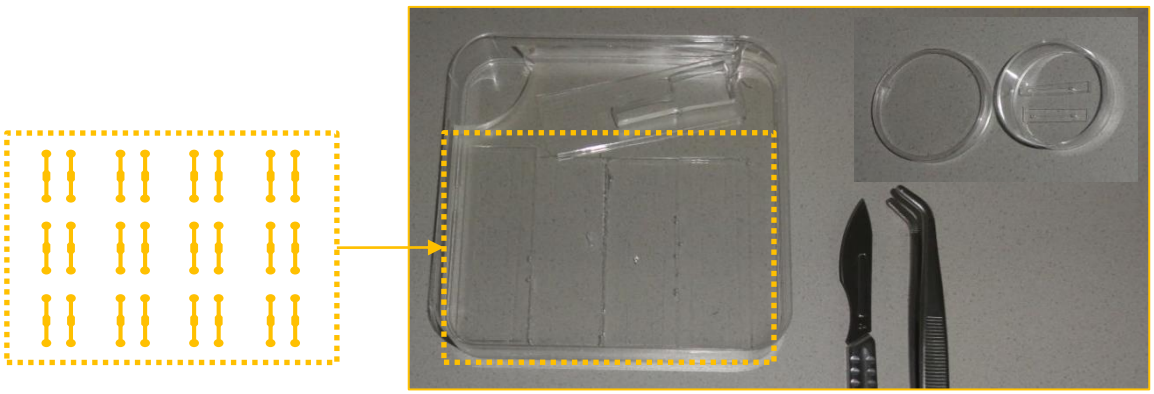

Figure 3.1.4: The PDMS channels fabricated using a multiple mold arrangement method on the polypropylene square petri dish as a bottom substrate. Individual channels were cut off with a sharp razor blade, gently peeled out from the container using tweezers and stored in a sterile, mini petri dish.

## 3.2. Experimental setup

In this section, the materials, the instruments and the experimental setup utilized for this thesis' experiments are presented.

### 3.2.1. Dark-field

The sample stage was illuminated with a conventional halogen light source (KL 1500 LCD-cold light infrared-free) with two light guides [as shown in Figure 3.2.1]. The video was recorded with a high-speed camera ((MIKROTRON EoSens MC 1362) which was connected to the computer with the particle tracking software installed.

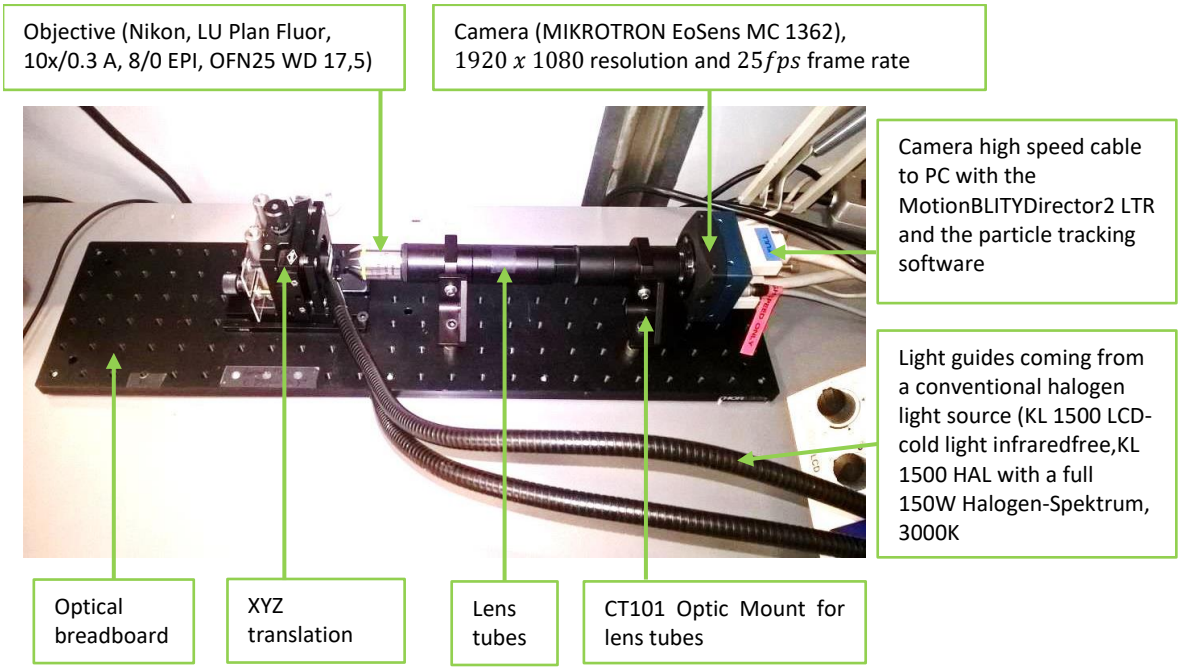


Figure 3.2.1: Experimental setup for the combined dark field microscopy and the Brownian quantification method. The optical system was mounted using thorlab optomechanical components.

The materials used to confine the liquid ($10\ \mu l$ drop) are: $\sim 40 \times 20 \times 0.17\ mm$ cover slip on the bottom and $20 \times 20 \times 0.17\ mm$ cover slide on the top). This sandwich like structure was sealed with a nitrocellulose based lacquer.

### 3.2.2. Magnetophoresis

The experimental setup employed for the magnetophoresis quantification method is shown in Figure 3.2.2. The microfluidic platform, placed under the optical microscope, was connected to the electronic breadboard and DC power supply. The videos were recorded using a Nikon Camera D5100 and stored on the PC where they were later processed using the 'particle tracking software'. In order to avoid error displacements, the camera was tightly screwed to the microscope C-mount adapter.

In this thesis' experiments, fluorescence microscopy was employed to obtain the strong image contrast between the MP-*E.coli* complex and the background. High-intensity light source i.e. High-Pressure Mercury Vapor Arc-Discharge lamp was used to evoke the sufficient photon excitation from the fluorophore (Alexa Fluor from the

secondary antibody). To start the excitement, the IGNITION button was pressed; appropriate filter on the block turret was selected and the filter block was removed from the epi-illumination light path.

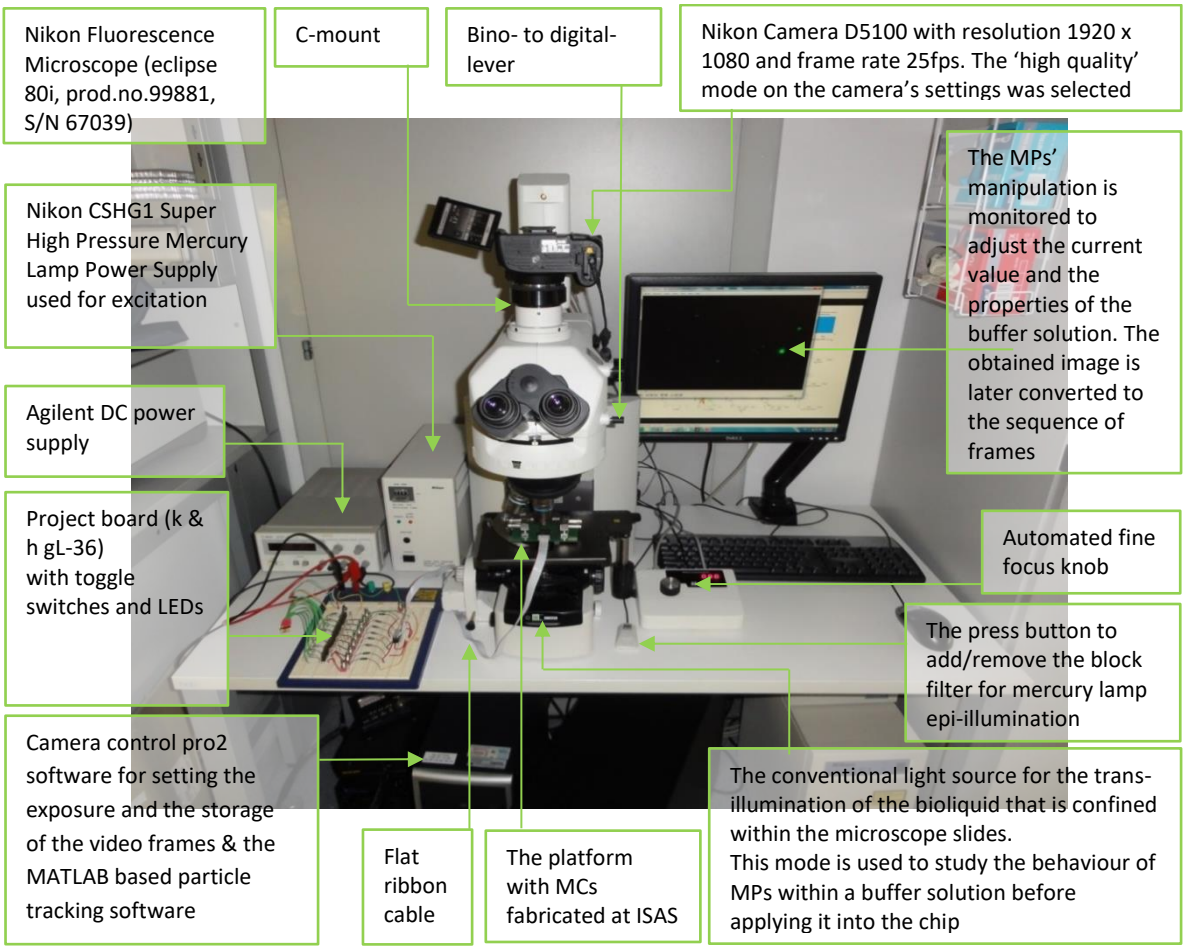


Figure 3.2.2: The experimental setup for the combined magnetophoresis and fluorescence microscopy quantification method.

The proper lens was selected to have high adequate magnification and a long enough working distance (here, the height of the microchannel is of relevance). A close-up of the microfluidic platform placed under the microscope can be seen in Figure 3.2.3. The resolution calculations for this particular objective were made before running the particle tracking software [see 2.2.1]. The same objective was used for all the measurement sets: A Plan Fluor objective with $2.6 - 1.8\ mm$ working distance and $60\times$ magnification. The FOV was adjusted in order to eliminate the tracking errors that come from the scattering of light on the channel's wall.

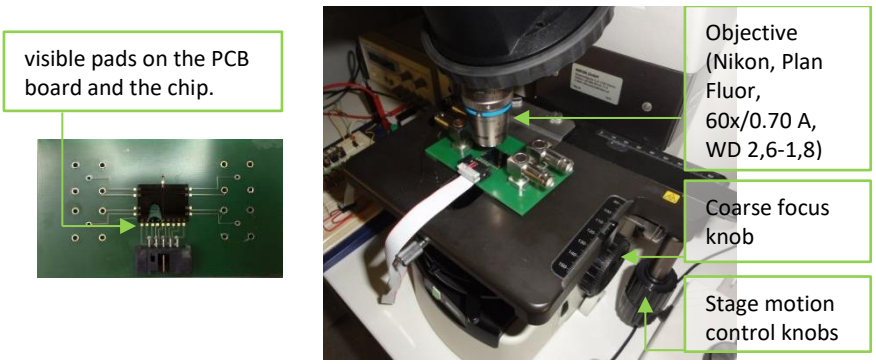


Figure 3.2.3: The microfluidic platform placed on the fluorescence microscope stage under $60\times$ magnification, Plan Fluor objective with $2.6 - 1.8\ mm$ working distance. After the measurement set with varying *E.coli* concentration was conducted, the new chip was sealed to the same PCB board and measurements were repeated.

After each use, the chip was washed with DI water and carefully (not to break the bonding) dried with Nitrogen. One channel per chip was used in this thesis experiments.

The sample was applied by pipetting a drop ($2\ \mu L$) of the liquid into the channel's inlet. Underpressure was applied at the outlet in order to fill the channel and the excess was removed with swabs. The no flow condition is checked under the microscope. After each measurement, the PDMS channel was rinsed with Acetone, Isopropanol and DI water and dryied with Nitrogen.

Figure 3.2.4: The channel is filled with the bioliquid through syringe-pressure driven flow

### 3.2.3. Sample preparation and application

This subsection covers a detailed description of the equipment and the materials that were used during the preparation of the biological sample. The exact procedure is stated in Appendix D and was repeated for all of the samples. Note that the underlined values were adapted and the impact of these adaptations on the protocol's efficiency was analyzed. Appendix D is the final version of the protocol that was later applied to all the sets of magnetophoretic and Brownian measurements.

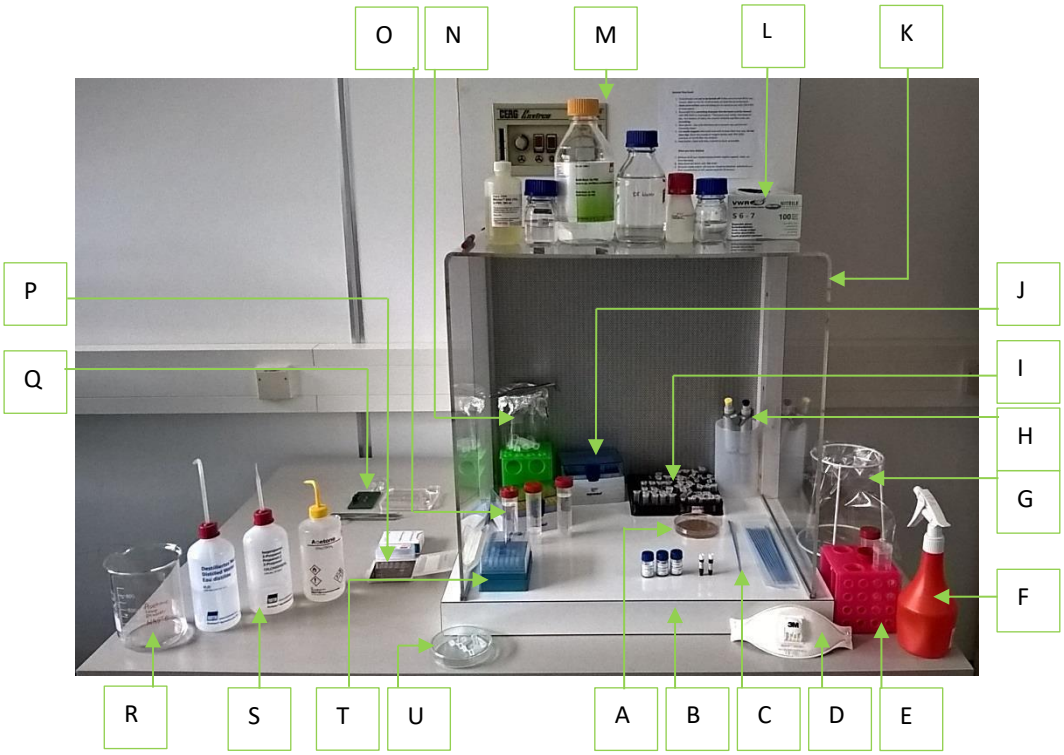


Figure 3.2.5: The experimental setup for biological sample preparation:

A. *E.coli* in PETRI DISH
B. MPs and antibodies
C. INOCULATION LOOP
D. 3M Aura Disposable Respirator FFP3 against bacterial infection
E. Test Tube Rack(pink) to keep TEST TUBE VIALS with biological disposal steady and safe
F. Isopropanol atomizer
G. Waste DISPOSAL BAGS
H. 3 × Eppendorf PIPETTES
I. Plastic VIAL RACK (black) to store the sample vials
J. Pippete TIPS: 1mL
K. LAMINAR FLOW HOOD
L. Nitrile gloves
M. Chemicals for the buffer solutions
N. 1 mL Plastic HINGE-CAP VIALS stored in 1L GLASS BEAKER and closed to avoid contaminations
O. TEST TUBE VIAL with portioned PBS-Tween, PBS-BSA and DI water (red lid)
P. USAF RESOLUTION TEST CHART
Q. Microfluidic platform. All of the platform components are stored in sterile plastic containers.
R. 1L GLASS BEAKER for waste disposal produced by the chip's and the channel's washing
S. plastic WASH BOTTLES with acetone, isopropanol and DI water
T. 100µL pipette TIPS
U. 2 mL plastic HINGE-CAP VIALS stored in glass PETRI DISCH

While following the biological binding protocol, the aseptic conditions were maintained and precautions were taken to avoid the non-specific binding and the contamination of the sample (i.e. before starting working in the laminar flow cabinet, all of the items were sterilized one-by-one with isopropanol). The work was conducted using gloves, white coat and respiratory mask to provide a barrier to antibodies, bacteria and irritating chemicals. The experimental setup can be seen in Figure 3.2.5.

The buffer solutions used in the final measurements were as follows: DI water for the magnetophoresis and PBS-BSA (0.1%) for the Brownian method. The latter (PBS-BSA (0.1%)) additionally served as a washing agent to remove contaminants from the sample. PBS in non-toxic and could be safely used for resuspension purposes without breaking the bonds between antibodies and *E.coli*. The other solution used for washing purposes was a *PBS-Tween (0.01%)* solution. The Tween stability and its relative nontoxicity allow it to serve as a detergent for MPs or bacterial washing. It also served as a binding buffer to reduce non-specific binding.


Figure 3.2.6: Chemical components required for preparation of washing and binding buffers: *Blocker™ BSA (10%) in PBS, Roti®-Stock* $10 \times$ PBS*, DI water and Tween® 20*

To ensure a uniform dispersity and even attachment of MPs/*E.coli* within the solution, the instruments presented on Figure 3.2.7 were used. In our experiments, $4.7 \times 10^3\ rpm$ were set on the $60\ mm$ rotor radius centrifuge instrument. The Relative Centrifugal Force (RCF)[41] acting on the sample amounted to $RCF = 1482 \times g$, where $g$ is the standard acceleration of free fall.

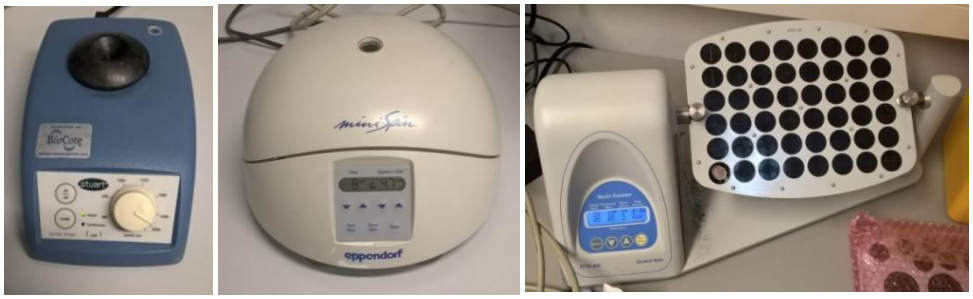


Figure 3.2.7: A) Stuart SA8 vortex mixer to mix the sample content and provide uniform attachment, B) Minispin Eppendorf centrifuge with a 12-place Fixed-angle rotor for 1.5–2.0 ml tubes (F-45-12-11) used to centrifuge the bacteria for washing purposes. Multiple washing was conducted during the sample preparation so as to eliminate the risk of non-specific binding. C) INCUBATOR&MIXER: multi-rotator Grant-bio PTR-60 to yield the binding between biological utilities and MPs.

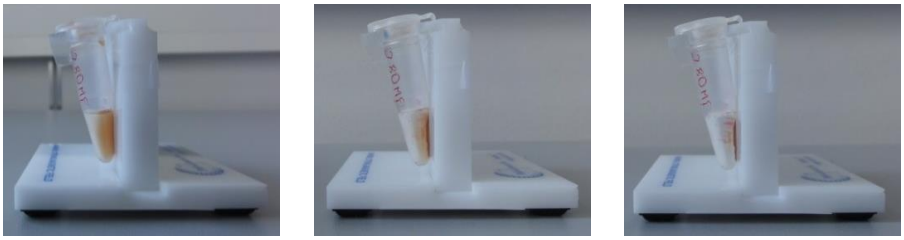

Figure 3.2.8: Washing of LMP by the use of Multi-three Microcentrifuge Tube Magnetic Separator. There is a visible MPs' attraction towards the magnet (to the right) with time. During the experiments it was observed that MPs cannot be kept on the magnetic stand longer than $3\ min$ because numerous agglomerations are created. The solvent was carefully removed after placing (gently!) the pipette's tip on the opposite (left) side of the vial's wall.

[41] Relative Centrifugal Force is calculated according to the equation: $RCF = 10^{-3} r_{mm} \frac{2\pi N_{RMP}^2}{60} \cdot \frac{1}{g}$ , where $N_{RMP}$ is a rotational speed, $r_{mm}$ is a rotor radius and g is a standard acceleration of free fall.

The requirements stated in section 2.3.5 for the type of MPs used, are met by the 'Dynabeads® M-280 Streptavidin'. These MPs have a mosaic matrix structure [see Figure 1.2.5] with an evenly doped mixture of maghemite ($Fe_2O_3$) and magnetite ( $Fe_3O_4$) within a highly cross-linked[42] porous polystyrene matrix. This composition is additionally enclosed within the protection polymer shell and covered with covalently coupled streptavidin [for more details see Appendix C]. The diameter of the single M-280 is $2{,}8\ \mu m$.

Figure 3.2.9: Antibodies were portioned into smaller vials and stored at -5°C (long term). Before the first use, the vials were defrosted and then kept together with MPs at 3°C (short term). Originally MPs are kept in buffer preservatives, therefore before adding any biological compound, they have to be washed magnetically 3x times.

Specific binding of the MP280 to the *E.coli* was achieved through 'Rabbit polyclonal Anti-*E.coli* primary antibody (ab20640)' [see Appendix F]. These antibodies target 'O' and 'K' *E.coli* strains and are additionally biotinylated through the amine-reactive group. The biotin from the antibody will attach to the streptavidin on the MP [for better theoretical explanation see Section 1.5]. The bacteria used in this thesis were of the wild-type K-12 strain of *E.coli.* This harmless strain was chosen as an alternative to the hemorrhagic[43] O157:H7 *E.coli* strains. Secondary antibodies that serve to label the *E.coli* with the Fluor ('Alexa Fluor® 488') are 'Goat Anti-Rabbit antibodies (ab150077)'. They are targeting the heavy and light chains of Immunoglobulin G [see Appendix F and Figure 3.2.9].

Apart from the MP-280, other MPs are also used to validate the systems' feasibility: 'Dynabeads™ M-270 Carboxylic Acid with diameters of $2{,}8\ \mu m$ .

The *E.coli* was cultured by heating the dry AGAR[44] at $37°C$, letting agar to melt and providing the nutrients for the growth. The procedure was prepared twice: first for the *E.coli* used in the Brownian method and later for the *E.coli* used in magnetophoresis method.

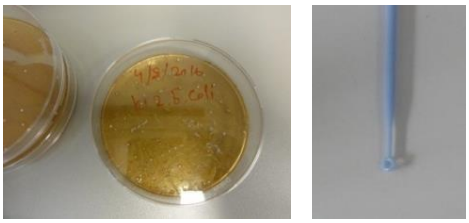

Figure 3.2.10: On the left: plastic disposable petri dish layered with solid plain nutrient AGAR (dark yellow) and the wild-type *E.coli* K-12 strain. There are visible scratches on the agar made by the inoculating loop. On the right: disposable, biologically inert polymeric Smear 1 $\mu l$ Loop used for bacteria intake. The container is quickly closed after the looping to avoid contamination. The storage temperature was 3°C.

To confirm the presence of *E.coli* attachment each sample was pipetted on the glass slide and analyzed under a fluorescence microscope using a drop of immersion oil (due to the oil immersion lens). It was done during validation of the binding protocol as well as before each measurement was started.


Figure 3.2.11: Additional verification of the attachment under immersed oil fluorescence microscopy

[42] *A high cross-linking is a tight bond that links one polymer chain to another and makes the material to be rigid*
[43] *Hemorrhagic refers to pathogenic bacteria that are causing inflammation*
[44] AGAR is a surface for a bacterial growth. It is derived from the polysaccharide agarose.

## 3.3. Experiments and Results

This section presents the findings of the research, focusing on the four key themes: 1) improvement of the biological binding protocol; 2) feasibility of this protocol for different *E.coli* concentrations; 3) feasibility of the Brownian quantification method and 4) feasibility of the magnetophoresis quantification method. The results are represented graphically, analysed and discussed.

### 3.3.1. Binding protocol improvement and comments

In the first part of the experiments, the binding protocol was controlled by altering the amount of the buffer solution and other liquids at different stages (protocol's steps) with different parameters applied.

It was found that when the value in step 8 in Appendix D was adjusted to $200\ \mu l$ (for $1cm$ *E.coli* 'intake'), the extent of unattached *E.coli* clusters created within the sample was reduced, while the attachment to MP was still achieved. Throughout the volumetric changes of the buffer solution, the MP's concentration and formation of agglomerations were lowered. A greater surface area available for *E.coli* binding has emerged and as a result, the numerous, visible Loaded Magnetic Particles [as seen in Figure 3.3.1(A)&(B)]] were formed. Furthermore, nearly all, the so-called 'bridges' [see Figure 3.3.1(C)]] were eliminated. This improvement was proposed to be applied before the 1h incubation process, where the 'final loading' takes place.

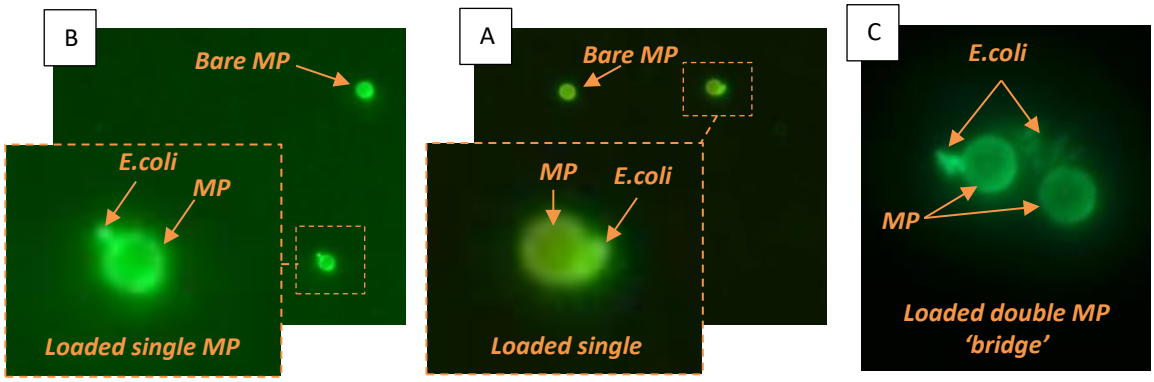


Figure 3.3.1: Through the analysis of the samples by means of fluorescence microscopy (Nikon oil $40\times$) the quality of the binding protocol can be evaluated.
Figure A: Output of $1\ cm$ *E.coli* concentration sample prepared according to the procedure from Appendix D. There is an evident *E.coli* attachment for the zoomed particle, while no noticeable attachment can be seen for 'bare MP'.
Figure B: Representation of another exemplary attachment for the same sample.
Figure C: Common agglomeration formed before the improvement of the binding protocol. There is a large *E.coli* cluster that serves as a 'bridge' connecting two individual MPs. Such agglomerations results in false readings and errors in the tracking procedure (particles adhere to the glass surface immediately after application) and therefore are avoided.
Different background intensities of the photos correspond to different time and intensity of the exposure

The performance of the binding protocol and the impact of further modifications were carefully studied. The results are reported below:

- Step 8 (from $200\ \mu l$ to $40\ \mu l$ and to $60\ \mu l$): Decreasing amount of buffer solution from 200ul to 40ul resulted in vast *E.coli* concentration and therefore numerous *E.coli* clusters without MPs attached. Frequent agglomerations were found due to 'bridges'. Similarly, for $60\ \mu l$ sample, long *E.coli* chains with agglomerations were observed.
- Step 12 (from $1\ \mu l$ to $2\ \mu l$): An increase of the amount of MPs resulted in formation of agglomerations (there were more agglomerations present for the $2\ \mu l$ sample.
- Step 12 (from 40ul to 50ul and 30ul): By increasing the amount of antibody-*E.coli* solution to $50\ \mu l$(while keeping the same amount of MPs), long *E.coli* chains and numerous MPs' clusters were observed. For

decreased amount of *E.coli*-antibody complex (i.e. $30\ \mu l$) no significant difference in the output binding was observed.

The above investigations were carried out under a fluorescence $40\times$ microscope. The particles, which at first seem to be unattached, might have had an attachment that was hidden behind or in front of the plane of observation. Since the above three modifications have not significantly improved the efficiency of the binding protocol, thus they were not applied in further experimentations.

Other observations collected within this subsection and which might be useful for preparations for future samples are:

- Strong vortex oscillations detach *E.coli*.
- The more bacteria are in the sample, the more agglomerations (also bridges) are created.
- Although the carried out untrasonification broke agglomerations, it is not further applied in the procedure due to undesired damage in *E.coli* bond. After analyzing the samples under the fluorescence microscope it was observed that some agglomerations were reduced, however others were still present (the biggest agglomerations found for the sample prepared according to the final protocol (2 cm *E.coli*) was 3 MPs attached to each other). Unfortunately, around 50 % of the *E.coli* attachments were broken. Instead of sonification (sonification might damage the proteins), careful sample care is preferable, where no strong vortex is applied.
- Additionally, it is recommended to keep the sample in constant motion to prevent accumulation of MPs which would normally facilitate the formation of unwanted clusters.
- Moreover, the binding protocol must be carried out in sterile conditions because the antibodies are polyclonal. It means that they may bind to other ubiquitous *E.coli* types which could have been transferred to the sample.

### 3.3.2. Feasibility of the binding protocol for bigger *E.coli* concentrations

Before starting the software tracking procedure, it was necessary to confirm whether the final protocol is also suitable for longer *E.coli* smears (i.e. *E.coli* intake) [step 1 Appendix D]. It was checked, if there was an evident relationship between *E.coli* in the solution and the number of *E.coli* rods attached to individual MPs.

The attachment for $\underline{1\ cm}$ inoculation was already confirmed in Figure 3.3.1(A)&(B). In the next figures, the binding results for $\underline{2\ cm}$, $\underline{4\ cm}$ and $\underline{6\ cm}$ *E.coli* inoculations are presented.

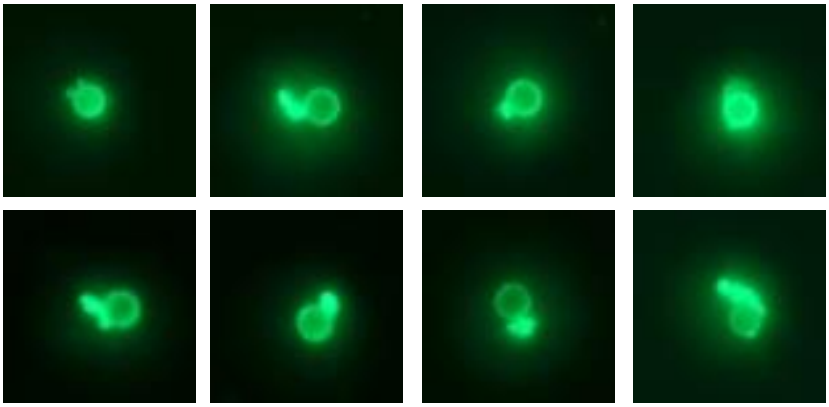

Figure 3.3.2: $c = [2\ cm]$ LMPs observed in sample 9 under fluorescent microscope (40x oil). The attachment of multiple rod-shaped *E.coli* to spherical MP is clearly visible. The orientation of the attachments and the orientation of the particle within the FOV are at random.

While comparing Figure 3.3.1(A)&(B) to Figure 3.3.2, it can be seen that there is a visible increase in attachments per single MP for the $\underline{2\ cm}$ sample as in comparition to the $\underline{1\ cm}$ sample. For the $\underline{2\ cm}$ sample, the attachments consist of multiple *E.coli* rods that are bound together (due to antibodies) creating tight visible clods. The arrangement of the attachments is arbitrary. As for the bigger *E.coli* concentration ($\underline{4\ cm}$), the number of the

attached *E.coli* is increased even more [see Figure 3.3.3]. The estimated ratio of the MP's volume to the amount of the biological component has declined. Short *E.coli* chains were observed. Some of the bacteria experience tiny movements that probably arise from whipping of their flagella [see Figure 1.5.1].

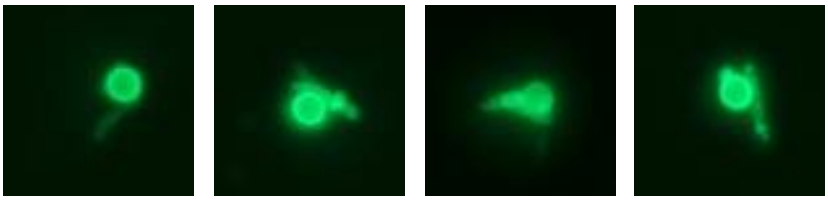

Figure 3.3.3: $c = [4\ cm]$ LMPs from sample 12 seen under fluorescent microscope (40x oil). Attached *E.coli* formed chains and clods.

As for the $\underline{6\ cm}$ sample, extensive attachments were reported. Figure 3.3.4 shows long *E.coli* chains that sometimes were even wandering around single MPs (few individual cases were observed). The attachments were confirmed for almost all of the MPs. The time required to magnetically wash this sample was also different as in comparison to samples where *E.coli* concentration was smaller. It seems that the biological component influenced the gathering of the MPs on the magnet's wall due to collisions [see equation (1.2.6)]

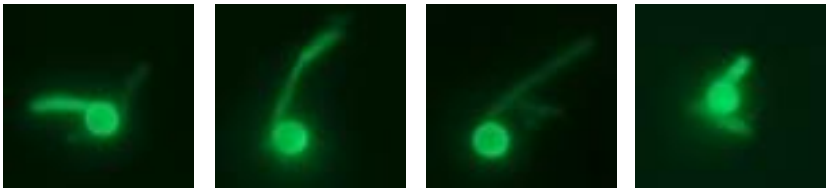

Figure 3.3.4: $c = [6\ cm]$ LMPs observed in sample 23 under fluorescent microscope (40x oil). Very long *E.coli* chains were observed for this sample.

It is apparent from the figures above that with increasing concentration of *E.coli*, there is also an increase in attachments and therefore the volumetric change of the MP-*E.coli* compounds.

Once the attachment was proved (verified), the 1st quantification method (Brownian method) could be started. The results from the tracking procedure are expected to vary along different *E.coli* concentration. Only these samples were further analyzed (i.e. for Brownian or Magnetophoresis tracking), for which the attachments could be clearly visible under the fluorescence microscope.

### 3.3.3. Brownian quantification method

The first set of measurements examines the diameters of bare, reference MPs (without *E.coli* loadings). The tracking results are represented in the form of a normalized histogram, where the height of each bar is equal to the probability of selecting an observation within that bin interval [121]) (i.e. the height of all the bars sums up to 1)[45], while the x-axis (axis of our interest) correspond to the calculated hydrodynamic diameter. The normalization was introduced in order to be able to compare distributions of all samples with different amounts of detected particles (i.e. different amount of observations). The short script nr.1, written for representation of the calculated hydrodynamic diameter distribution, is included in Appendix C.

Sample with bare magnetic particles M-280 Steptavidin (without the layer of biotinylated antibodies) was prepared by pipetting $1\ \mu l$ of original MPs (M-280 Streptavidin) into $200\ \mu l$ of PBS-BSA (0.1%). The $10\ \mu l$ drop of this mixture was applied on the glass slide. The highest peak interval ranges between $2200$ and $2300\ nm$ [see Figure 3.3.5]. The values above $10000\ nm$ are outliers resulting from impuritues (e.g. dust) and are not included in further analysis (aslo in the case of other samples). Based on this reference distribution and assuming that the change of diameter correspond to the size of *E.coli* attached, the following regions are defined:

[45] *This is a 'probability' type of normalisation where the bin value $v_i$ is estimated according to the equation: $v_i = c_i/N$ , where $c_i$ is the number of elements in the bin and $N$ is the number of all elements in input data.*

i. $0\ nm < d < 2100$ nm — unnatached *E.coli* suspended in the buffer solution
ii. $2100\ nm < d < 2800\ nm$ — bare MPs (without loadings)
iii. $2800\ nm < d < 4500\ nm$ $\sim 2\ \mu l$ ) — LMP (single *E.coli* loading since *E.coli* width is$\sim 0.5\ \mu l$ and length
iv. $4500\ nm < d < 7000\ nm$ — LMP (multiple *E.coli* loadings)
v. $7000\ nm < d < 10000\ nm$ — agglomerations or numerous *E.coli* loadings on single MP
vi. $d > 10000\ nm$ — impurities (dust): outliers

The above regions are estimated for the analysis of the next samples where the biological component is already present. It is assumed that the maximal size of the single LMP (i.e MP loaded with single *E.coli* rod) equals to $2.8\ \mu m + 0.5\ \mu m = 3.3\ \mu m$ or $2.8\ \mu m + 2\ \mu m = 4.8\ \mu m$ depending on the binding's arrangement. Since the highest peak on Figure 3.3.5 is shifted to the left, so are the other regions.

The resultant distribution has a right-positively skewed shape. If values above 4500 nm are treated as outliers (due to the formation of double MPs or big agglomerations or the presence of impurities), the distribution's trend would strive toward Gaussian distribution. The highest number of counts lie in the light green area (bare MP) and equals to 38.7% of all counts. The highest bar ( $2200$ to $2300\ nm$) is in close proximity to the expected diameter which is $2800\ nm$.

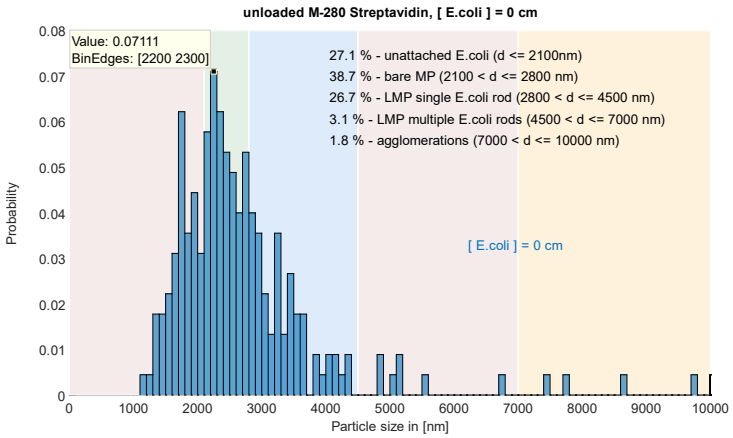


Figure 3.3.5: SAMPLE 0; Normalized histogram distribution for the calculated hydrodynamic diameter for unloaded M-280 Streptavidin; $c = [0\ cm]$

SAMPLE 17 was prepared following strictly the binding protocol presented in Appendix D. There are two characteristic peaks on the output graph. The peak with the highest probability lies between $2500\ nm$ and $2600\ nm$ , which is a different range as in comparision to reference $0\ cm$ *E.coli* sample. The other marked peak $(4100 - 4200\ nm)$ corresponds probably to LMPs (with more arrachments). The distribution is shifted to the right in comparition to bare MPs. The values of the calculated hydrodynamic radius are therefore greater then for the reference sample. There are some small diameters (below $1000\ nm$) which could correspond to deattached bacteria (as in comparition to reference sample where no diameters below$1100\ nm$ are present because no *E.coli* was added to that sample). Throught the analysis of the histograms it is possible to evaluate which distribution would correspond to $0\ cm$ and which one to $1\ cm$ *E.coli* concentration.

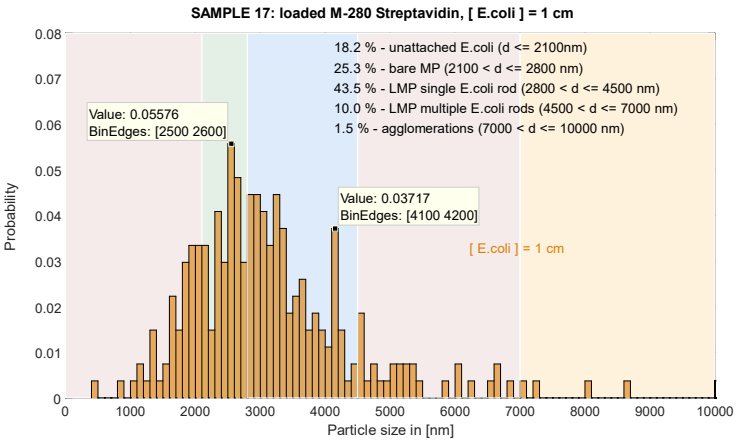


Figure 3.3.6: SAMPLE 17; Normalized histogram distribution for the calculated hydrodynamic diameter for *E.coli* attached M-280 Streptavidin $c = [1\ cm]$

SAMPLE 18 was prepared in the same manner (the same procedure) and on the same day as the SAMPLE 17. The distribution of this sample does not overlap with the distribution of SAMPLE 17. This was caused by the change of the amount of liquid that was applied on the glass slide (instead 10ul as in sample 17, 20ul was applied). The additional dynamics due to the excess of liquid on the glass slide could affect the distribution

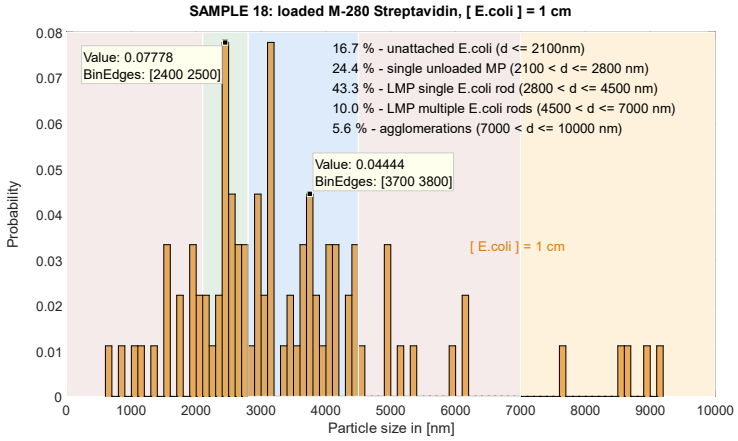


Figure 3.3.7: SAMPLE 18; *E.coli* attached M-280 Streptavidin $c = [1\ cm]$

To study the influence of binding protocol's parameters an additional SAMPLE 0707 was prepared. SAMPLE 0707 was resuspended in smaller amount of buffer PBS BSA (0,1%): in step 8 [see Appendix D]: it was $40\ \mu l$ instead of $200\ \mu l$ and in step 13: instead $200\ \mu l$, $100\ \mu l$ of buffer solution was used (as in comparison to SAMPLE 17 and SAMPLE 18). Due to an increased condensation of bacteria (step 8) the bigger attachments were present (more *E.coli* at this protocol's step resulted in more attachments). This relationship is illustrated on the distribution graph, where the highest peaks were moved to the right. Therefore the sensitivity of tracking to different *E.coli* concentrations is proved again.

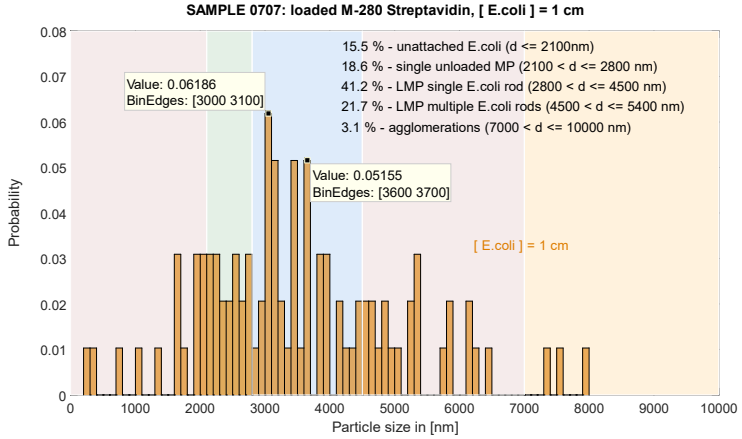


Figure 3.3.8: SAMPLE 0707; *E.coli* attached M-280 Streptavidin $c = [1\ cm]$

The procedure was followed according to Appendix D and 10ul drop was applied (similarly to SAMPLE 17).

The distribution is shifted to the right in comparison to SAMPLE 17. There is more attachment. The counts corresponding to 'unloaded MP' has decreased while for LMPs has increased. There are characteristic peaks at $3400 - 3500\ nm$ and $4600 - 4700\ nm$ which corresponds to LMPs. The relationship between changing concentration ($0\ cm$ vs $1\ cm$ vs $2\ cm$) and the distribution can be already observed at this point.

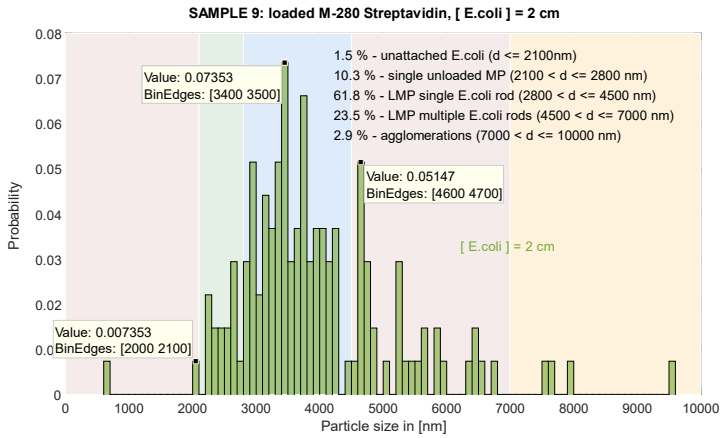


Figure 3.3.9: SAMPLE 9; *E.coli* attached d M-280 Streptavidin $c = [2\ cm]$

The next 3 samples were prepared following strictly the protocol from Appendix D (the same as SAMPLE 17 and SAMPLE 9). A $10\ \mu l$ sample drop was applied. Since bacteria have not grown uniformly on the agar plate, the $4\ cm + 1\ cm$ scratch was taken. The distribution shows that almost all MPs were loaded with bacteria (what was confirmed by fluorescent microscopy observations [see Figure 3.3.3]). The histogram is shifted to the right.

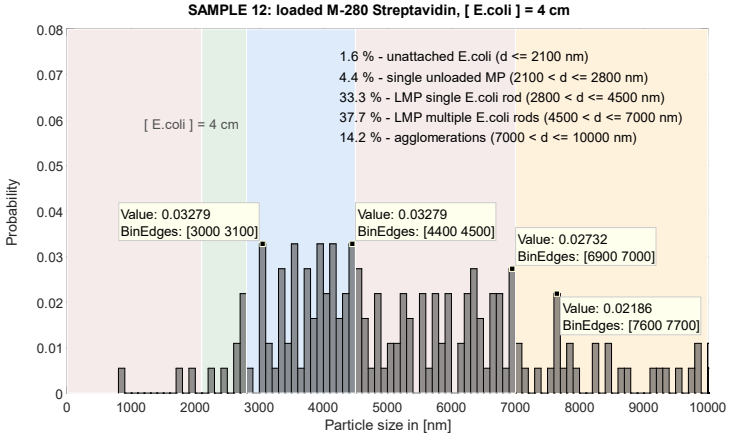


Figure 3.3.10: SAMPLE 12; *E.coli* attached M-280 Streptavidin $c = [4\ cm]$

The additional sample for $4\ cm + 1\ cm$ concentration was prepared (sample was prepared on the same day parallel to the SAMPLE 12 so as to keep all of the incubation conditions unchanged) and to test if the results for all 4cm samples are similar.

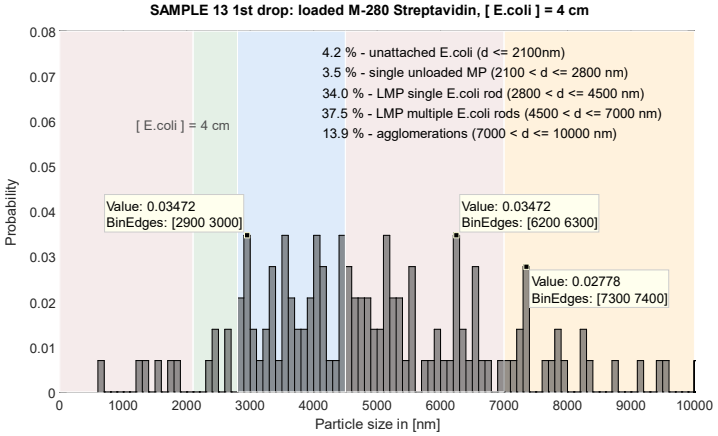


Figure 3.3.11: SAMPLE 13A; *E.coli* attached M-280 Streptavidin $c = [4\ cm]$

The measurement was repeated for SAMPLE 13. The 2nd drop was applied. Although the distribution is not an exact copy as the 1st drop, the percentages of observations within previously defined areas are comparable.

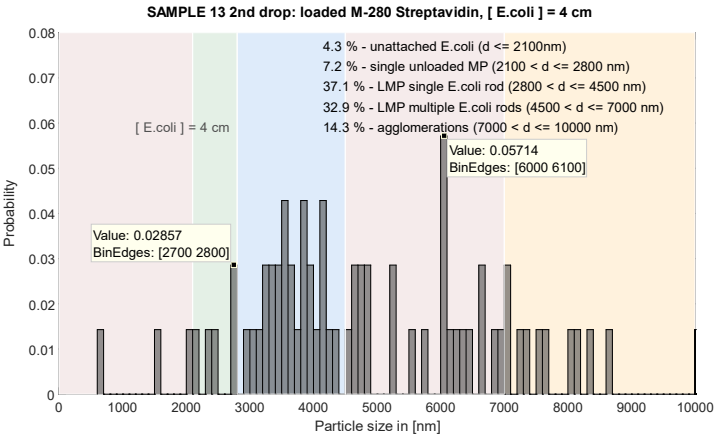


Figure 3.3.12: SAMPLE 13B; *E.coli* attached M-280 Streptavidin $c = [4\ cm]$

The last two samples were prepared in the same manner as SAMPLE 12, 13, 17 and 9 including the same 10 µ$l$ amount of drop applied on the glass slide. Only the concentration was changed to 6 $cm$.

While analyzing the distribution, no significant high peaks in 'single unloaded MP' area are present. Thus it is evident that all MPs were loaded. It can be said that the distribution is shifted to the right as in comparison to previous samples. The counts in light pink area 'multiple *E.coli* rods' loadings have increased.

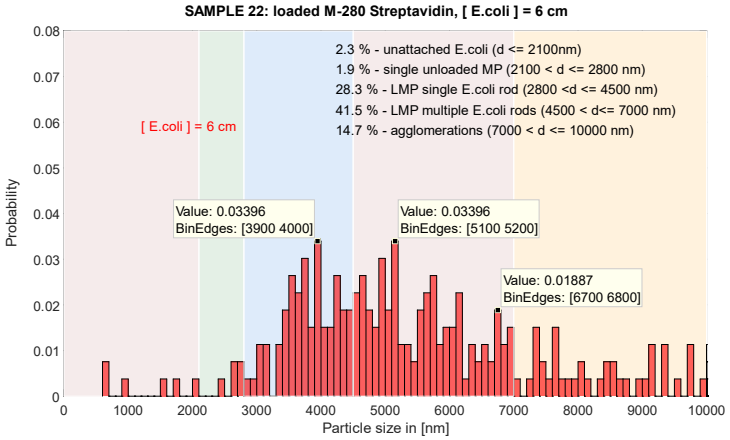


Figure 3.3.13: SAMPLE 22 ; *E.coli* attached M-280 Streptavidin $c = [6\ cm]$

The measurement from SAMPLE 22 was validated by SAMPLE 23 (incubation conditions unchanged).

Obtained results have a similar distribution and percentage of counts within specified areas as for SAMPLE 22.

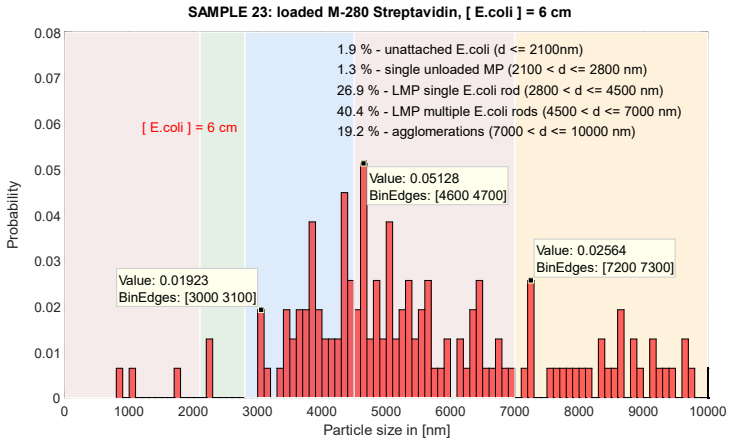


Figure 3.3.14: SAMPLE 23; *E.coli* attached M-280 Streptavidin $c = [6\ cm]$

Therefore it can be said that the calculated hydrodynamic diameter is related to the *E.coli* concentration (the bigger the concentration is, the bigger the radius gets). The short script written for representation of the above data is also included in Appendix C.

Several issues were identified during measurement's procedure. It was observed, that only these samples (FOVs) could be tracked, which do not experience any artifact movements (i.e. jolt (shock) disruptions or other displacements that originate in liquid's non-uniform dispersion). Therefore, it is important to always apply the same amount of liquid and to proceed with the sample very carefully. While pipetting and sealing, air bubbles must be avoided and cover slide must not slide. The area of the sample chamber is $20\ mm \times 20\ mm$ which gives numerous potential FOVs for observation. None of these FOVs should comprise slip edges because it creates unwanted scattering (at the edges). Furthermore, there is a significant correlation between MPs' glass adhesion and concentration of *E.coli* within a liquid. MPs with 'multiple *E.coli* rods' loadings are more likely to adhere to the glass surface, therefore the tracking procedure is carried out immediately after pipetting.

Apart from the above-presented distributions, other parameters that describe the MPs' dynamics within the liquid were plotted and analyzed. An exemplary output of the results obtained for sample 0 $cm$ can be seen in Figure 3.3.15. Here, information about the mean displacement (MD) during $\Delta t$, the positions of the particles on the frame with time, the velocities along y and x axis for individual particles, as well as the counts of all tracked particles within different FOVs is given.

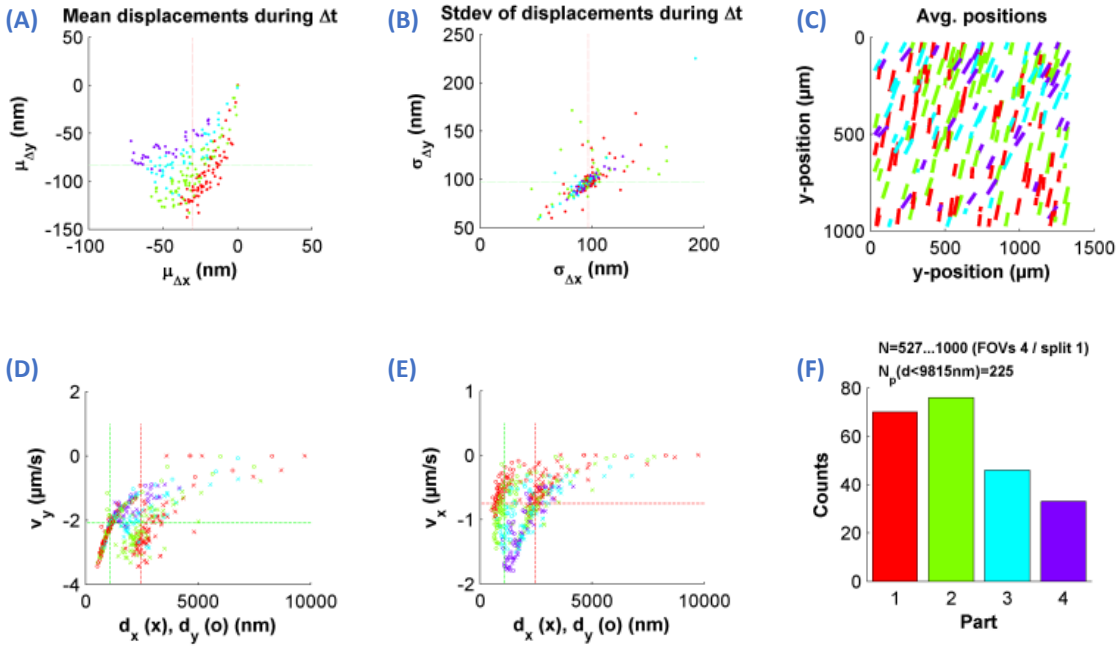


Figure 3.3.15: Figure: Graphical data representation of the Tracking Software output for sample 'bare MPs'. $d_x$ is the calculated hydrodynamic diameter from 1D Brownian motion along horizontal x-axis.

(A) – calculated Mean displacement $\mu_{\Delta x}$ , $\mu_{\Delta x}$ during $\Delta t$ in $[nm]$
(B) – standard deviation of displacements during $\Delta t$
(C) – x and y positions (with time) of detected particles on multiple FOVs in $[\mu m]$
(D) – sedimentation averaged particle velocity $v_y = \mu_{\Delta y}/\Delta t$ in $[\mu m/s]$
(E) – horizontal average particle velocity $v_x = \mu_{\Delta x}/\Delta t$ in $[\mu m/s]$
(F) – counts of tracked particles for all collected FOVs (there are 4 FOV for this sample). The number of particles should be big enough to obtain reliable results.

Such plots were also drawn for other samples.

Similar plots were drawn for all the samples and following results were reported:

- Plots (F): The number of particles tracked for all of the samples ranges between 70 (sample 13 2nd drop) and 269 (sample 17). The counts of tracked particles for all collected FOVs were big enough to obtain reliable results. The final concentration [step 14 Appendix D] of MPs within the liquid was adjusted sufficiently.
- Plots (C): From the 'Average position' graphs it can be seen, that the displacements of the particles within an individual FOV are matched (in length and direction). Therefore, it can be said that no significant artifact movements have occurred during the procedure.
- Plots (D): For almost all samples, the distribution of sedimentation velocities $v_y$ ranges as follows: $0\frac{\mu m}{sec} < v_y < -4\frac{\mu m}{sec}$ . It represents the theoretical sedimentation value that was calculated according to [122] and equals to 1.7 $\mu m/s$ [46] . Obtained velocities have indicated that only the sedimentation movement in the y direction '(no jolt y-direction movements) was present. The exceptions were: sample 18 (increased amount of drop 20 $\mu l$), where instead of sedimentation, an upward motion is observed, sample 12: there is no clear sedimentation visible and even an upward motion appears, sample 13_2nd drop: velocities ranges between $-0.5$ and $+0.5$ $\mu m/sec$. Based on the sedimentation it is not possible to determine the trends in concentrations (the increase of attachment has not significantly influenced the range of the particle's vertical velocity). Therefore, additional velocity considerations on the x- axis are required.

[46] *Theoretical sedimentation velocity $w_s$ for bare M-280 Streptavidin particle of diameter $d$ was calculated according to the equation: $w_s = 4\Delta g d^2/3Av_k$ , where $g$ is the gravitational acceleration, $v_k$ is the fluid kinematic viscosity, A is a constant ($A = 24$) , $\Delta = \rho_s/\rho - 1$ , where $\rho_s$ is spherical particle's density and $\rho$ is density of fluid.*

- Plots (E): It seems that the particles' average velocities $v_x$ along x-axis tend to decrease with increasing *E.coli* concentration. This is explained by the Brownian motion theory, according to which smaller particles travel longer distances (they are 'faster', more diffusive particles) than the bigger ones for the same time interval $\Delta t$ .
- Plots (A): The median values for Mean Displacements [$\text{'MD during } \Delta t'$ ] were calculated: $-34.05\ nm$ (plain MP), $-20{,}5\ nm$ (sample 17), $-18.6\ nm$ (sample 9), $-16.27\ nm$ (sample 13_1st drop), $-1.34\ nm$ (sample 22), $-2.21\ nm$ (sample 23). The relationship between the *E.coli* concentration and the MD is demonstrated (with increasing concentration, there is a decrease in the MD). The MD for sample 12 and sample 18 (the motions experienced by them differ from the rest of the samples) are $7.19\ nm$ and $17.52\ nm$ respectively.
- Plots (B) Standard deviations[47] for single particle displacement during $\Delta t$ for the above samples, are comparable and they range from $50\ nm$ to $\sim 150\ nm$ .

To compare/summarize all of the samples, a non-parametric kernel smoothing function[48] was estimated to find a fit for the above-presented histograms[49]. The density is evaluated for each individual sample at 10000 equally spaced points that cover the entire range of the data with an exclusion rule: 10000. Plots are drawn with MATLAB script nr.1 [Appendix C], where following parameters are set: smoothing type: epanechnikov, Bandwidth:$Auto$, Domain:$-Inf\ <\ y\ <\ Inf$. The results are presented in Figure 3.3.16. The samples with impeccable trajectory motions (i.e. without draft/jolt motions) are highlighted with solid lines.

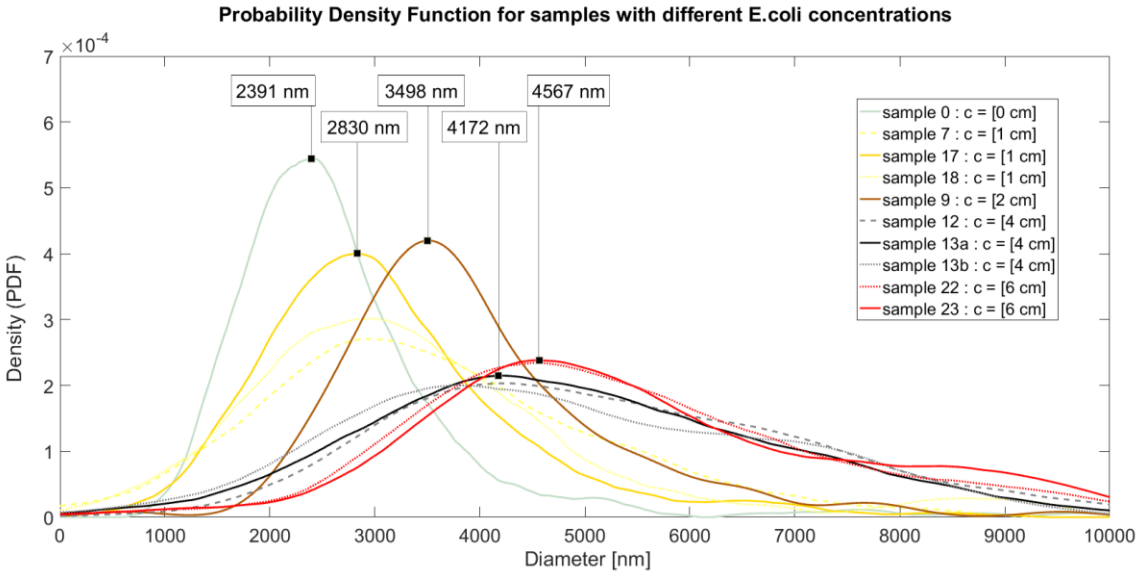


Figure 3.3.16: Quantification of *E.coli* content by acquiring the range of values of the calculated hydrodynamic diameter. This figure represents the fitting curves for samples with various *E.coli* concentrations ($0\ cm$, $1\ cm$, $2\ cm$, $4\ cm$, $6\ cm$). There is an obvious trend towards an increase in estimated particle diameter with greater *E.coli* concentration. To all samples the same fitting parameters were applied as follows: Distribution: non-parametric (kernel), Exclusion rule: 10000, Smoothing type: epanechnikov, Bandwidth: $Auto$, Domain: $-Inf\ <\ y\ <\ Inf$

[47] *Standard deviation for all mean displacements within* $\Delta t = 00.4\ sec:\ s = \sqrt{\sum_{i=0}^{N}(x_i - \bar{x})^2/(N-1)}$

[48] *''Kernel density estimation is a non-parametric approach to estimate the Probability Density Function (PDF) of a random variable. It is closely related to histogram and additionally endowed with smoothing and continuity options.''*

[49] *In the 'pdf ' type of 'normalisation', these are the bar* ***areas*** *that sums up to 1 (as in comparison to previous type of 'normalisation' i.e. 'probability' where instead of 'areas' we had '****heights****'[see footnote 45]). In 'pdf', the bin value* $v_i$ *is estimated according to the equation:* $v_i = c_i/Nw_i$ *, where* $c_i$ *is the number of elements in the bin,* $N$ *is the number of all elements in input data and* $w_i$ *is the width of the bin.*

The findings presented in Figure 3.3.16 confirm the association between calculated hydrodynamic diameter and bacteria concentration. The peak values for the samples: sample plain, sample 17, sample 9, sample 13, sample 23 ascend in the following manner: $2391\ nm$, $2830\ nm$, $3498\ nm$, $4172\ nm$, $4567\ nm$ respectively. It means that the calculated hydrodynamic diameter has increased by the values which correspond to width/length of *E.coli* rods[50] depending on the arrangement of binding.

The cumulative probability function was also drawn to represent the probability that the value of a random variable falls within a specified range (within a specific diameter size) [see Figure 3.3.17]. If the probability of 0.5 is assumed the diameters of sample plain, sample 17, sample 9, sample 13, sample 23 will take the value less than or equal to $2470\ nm$, $2945\ nm$, $3722\ nm$, $4595\ nm$ and $5180\ nm$ respectively.

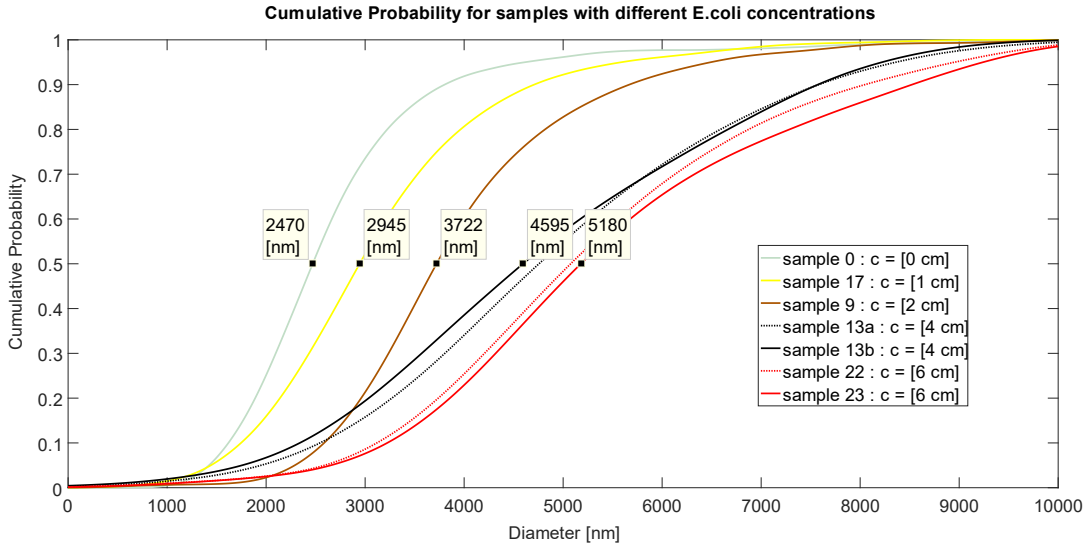


Figure 3.3.17: The cumulative probability functions for the samples containing different amount of E.coli bacteria. The probability of 0.5 is assumed.

Since the calculated hydrodynamic radius is slightly shifted to the left (i.e. it is in close proximity, but still not precisely 2800 nm), additional verification of the feasibility of the tracking system was necessary. The tracking of bare Dynabeads™ M-270 Carboxylic Acid MPs was carried out and the distribution of calculated hydrodynamic radius can be seen in Figure 3.3.18. After applying the same fitting parameters as in the Figure 3.3.16, the $2726\ nm$ peak was obtained. This proves the high accuracy of the system since the claimed ($\sim 2800\ nm$) and the calculated diameter of the particle overlap.

Since the results obtained for the carboxylic MPs coincide with the specifications [see Appendix E], which proves the feasibility of the tracking system, additional verification of size of streptavidin MP was conducted and compared to the calculated one. The sizes of MPs were obtained by means of Scanning Electron Microscopy (SEM[51]) [see Figure 3.3.19]. The conducted measurements showed that some of the measured diameters accurately overlap with the specifications seen in Appendix E while some deviate up to $\pm 100\ nm$ .

[50] *In this thesis experiments, the layer of linkage system was very thin in comparison to the sizes of micromarker and pathogen. Therefore, the layer of streptavidin, biotin, antibodies and Fluor could be neglected. Only the diameter of MP and the width/length of E.coli was taken into consideration.*

[51] *SEM produces images by scanning the sample's surface with a focused beam of electrons in a raster manner. Signals resulting from interactions of these electrons with the sample surface are detected and high resolution (up to 100 nm) and great magnification (30,000×) is achieved.*

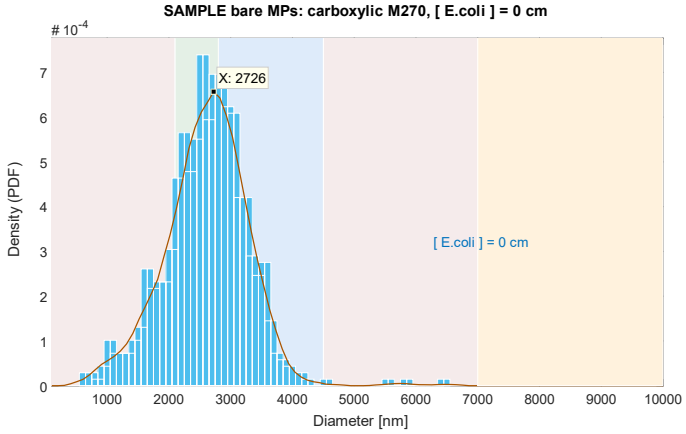


Figure 3.3.18: The Probability Density Function fitted to the estimated distribution of calculated hydrodynamic diameter for SAMPLE; bare Dynabeads ™ M-270 Carboxylic Acid $c = [0\ cm]$

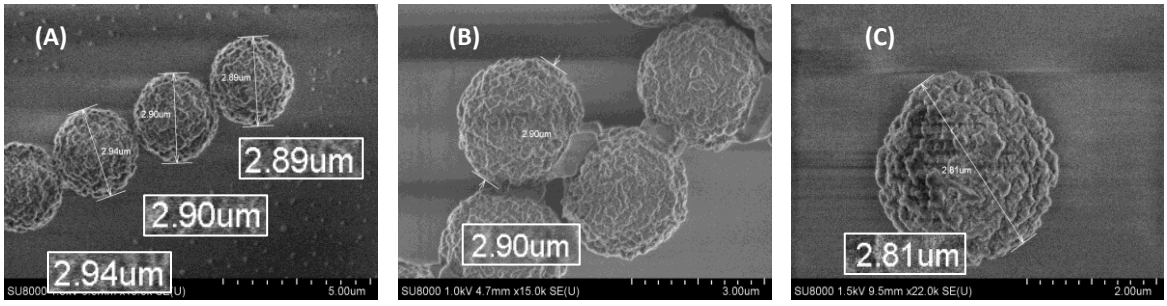


Figure 3.3.19: SEM images of bare MP-280 Streptavidin and their sizes

- (A)&(B): 15000 ×, $WD = 4.7\ mm$, $U_{accelerating} = 1000\ V$, $U_{deceleration} = 0\ V$, $I_{Emission} = 6200\ nA$, $Condition_{Vacc} = 1\ kV$
- (C): 22006 ×, $WD = 9.5\ mm$, $U_{accelerating} = 1500\ V$, $EmissionCurrent = 9000\ nA$, $Condition_{Vacc} = 1.5\ kV$

The shift for streptavidin particles cannot be explained by the means of different functionality as in comparison to carboxylic MP. The groups on the surface of carboxylic MPs are less functional than for the ones on streptavidin MPs. Therefore, in this sense, the streptavidin particles are less 'diffusive' and if the functionality would play a role, than the calculated hydrodynamic diameter for M-280 streptavidin would be greater than that of M-270 carboxylic (which is opposite to the results). Therefore, the possible explanation for obtaining the value in the proximity of (instead of precisely) $2800\ nm$ is:

1. Different physical properties resulted in varying molecule interactions:
    a. hydrophobic and hydrophilic nature of M-280 and M-270 respectively [see Figure 2.1.2], or
    b. variability of 'diffusive double layer' [see Section 'DVLO Force'] ($-COOH$ particles represent a charge therefore their diffusive double layer was greater resulting in the bigger diameter).
2. The viscosity of the PBS-BSA 0.1% solution was greater than the assumed viscosity of water which resulted in smaller calculated diameter [see equation (2.1.2)].
3. There was a temperature change caused by heating up of the room due to illumination and running PCs. The value of this parameter directly impacts the value of the calculated hydrodynamic diameter [see equation (2.1.2)].
4. There might be some systematic error related to the sample application procedure or measurement technique.

### 3.3.4. Magnetophoresis quantification method

*DC power supply* supplied microconductors with a constant DC voltage value of $12\,V$. The current in every individual MC was $53\,mA$.

Sample with unloaded MPs was prepared with no *E.coli* bacteria being present in original (intake) sample (i.e. *E.coli* smear: $0\,cm$). The preparation procedure was carried out in a way to keep the concentration and the incubation's parameters unchanged (the protocol from Appendix D was followed excluding the 'C. Bacteria washing' steps). That is, instead of using bare MPs, they were additionally coupled with primary and secondary antibodies. Furthermore, secondary antibodies (additionally labelled with Fluor [see Theory]) served for visualisation purposes to obtain images with high contrast (bright spots over the dark background) which was essential for the tracking software. Since an even luminescence of Fluor around MP was observed, it can be said, that the antibodies were evenly distributed over the spherical MPs surface creating a uniform surface.

Once the particles were injected in the PDMS channel and the 'no flow' condition was satisfied, the manipulation started.

After obtaining videos free of artifacts, the sample could be finally used in the software tracking procedure [see page 26]. The Figure 3.3.20 represents all tracked particles within $1800$ frames (i.e. the centroids of bright spots that correspond to particles). As previously stated in the Section: 'Software Tracking Procedure/Routine', frames were collected at $25\,fps$ (with high quality' and 'high sensitivity' settings) and the frames' dimensions were $1920x1080\,pixels$.

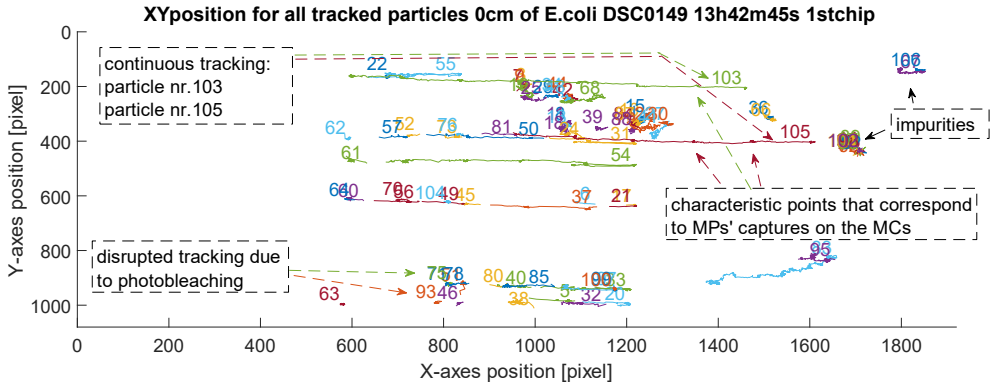


Figure 3.3.20: 1st chip, Sample $0\,cm$ : Positions for all detected and tracked particles over the sequence of frames ($1920x1080\,pixels$) collected at $25\,fps$. The particles were manipulated horizontally. There are some characteristic points visible on these trajectories. They correspond to the position of the MP as it was captured at a MC. There are over $105$ trajectories detected for this sample.

It was observed that the MPs within $0\,cm$ sample exhibited a strong photobleaching effect (stronger than samples where concentration of *E.coli* $c \neq [0\,cm]$). This might explain why the tracking trajectory for same particle was interrupted (as in the case of two particles that at the very bottom of the Figure 3.3.20). Photobleaching could be related to the freshness of antibodies, smaller amount of antibodies attached to bare MP as in comparison to LMP, rotation of a particle around its axis or Joule heating due to current.

The particles were set in motion horizontally i.e. along the x-axes of the frame (along $1920\,pixels$ width). The pixels were converted into real dimensions by applying the previously calculated resolution $Res = 7.2\ pix/\mu m$ [see Section 2.2.1]. The displacement of tracked particles over the sequence of frames is presented on Figure 3.3.21. From this graph, the estimated x-positions corresponding to the beginning and end of motion could be extracted (i.e. these are the sharp edges on the graph that indicate the current switching). From these positions (i.e. data enclosed in the Data Cursors on the Figure 3.3.21) the velocities for the total displacement (i.e. between

two neighbouring MCs) were calculated according to the MATLAB script nr.4 in Appendix C. Figure 3.3.21 represents the data box and the velocities for particle $nr.103$ (green) only.

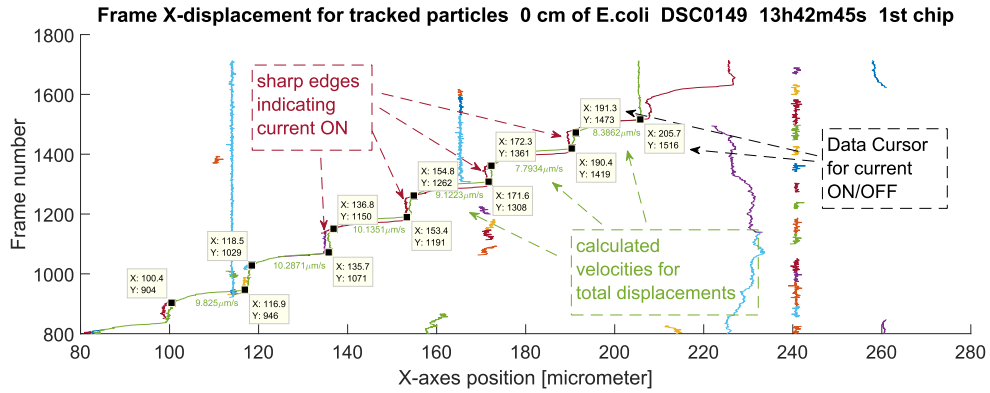


Figure 3.3.21: 1st chip, Sample $0\ cm$ : The displacement of tracked particles over the sequence of frames. There are two characteristic manipulation's paths for: particle $nr.103$ (green) and particle $nr.105$ (dark red).

The two plots above were drawn for all of the samples with varying concentrations (i.e. first the plot of 'positions for all the detected and tracked particles within a sequence of frames in pixels, was drawn and then the 'The displacement of tracked particles over the sequence of frames'). For all of the samples, successful manipulation and tracking were achieved. Also, the script nr.4 was applied to calculate the velocities for all of the samples with varying concentrations$c = [0cm], [1cm], [2cm], [3cm], [4cm]$. One more example (2nd chip, $c = [2cm]$) is depicted below [see Figure 3.3.22 and Figure 3.3.23].

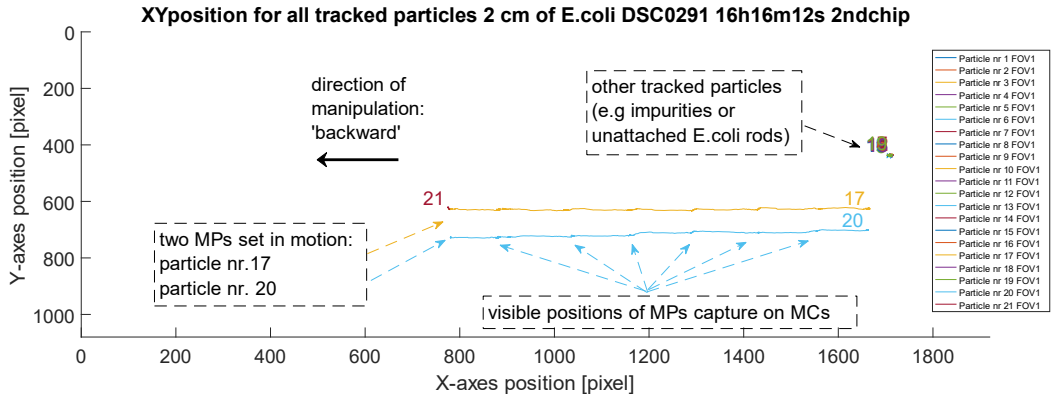


Figure 3.3.22: 2nd chip, Sample $2\ cm$ : Positions for all the detected and tracked particles over a sequence of frames $(1920x1080\ pixels)$ recorded at $25\ fps$. There are some characteristic points visible on these trajectories. They correspond to the position of the MPs as they were captured above the MCs There are over $21$ particles (including impurities) detected for this sample. Particle $nr\ 17$ and particle $nr\ 20$ correspond to two different LMPs that were set in motion due to the magnetic field gradient.

For this sample, two MPs were present on the recorded FOV. The outputs of the tracking routine were excellent due to the uninterrupted trajectories. There were only a few impurities detected. Such a good quality of the tracking process is a result of the high fluorescence intensity of the MPs, sufficient sample washing and setting appropriate parameters (as a result no background noise was tracked).

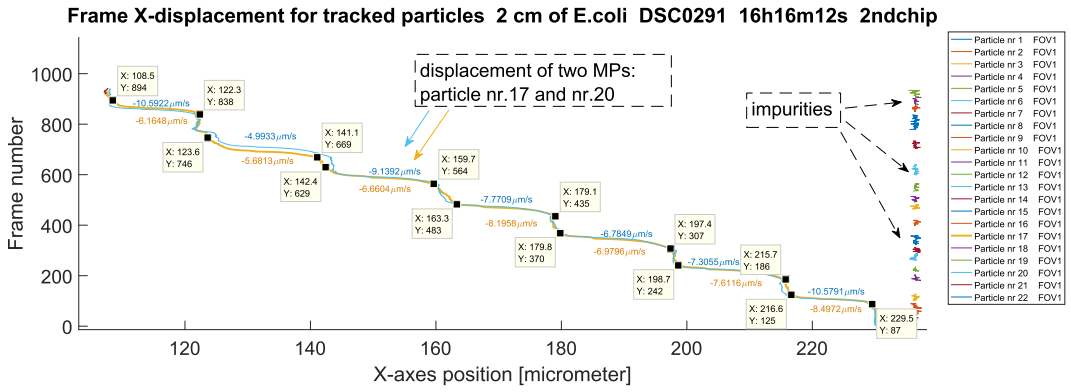


Figure 3.3.23: 2nd chip, Sample 2 $cm$ : The displacement of tracked particles over the sequence of frames. There are two characteristic manipulations of MPs: particle $nr.17$ (yellow) and particle $nr.20$ (blue). The rest of the tracked particles are impurities (on the right) and can be clearly differentiated from MPs.

The plots of the movement along x-axis for two MPs overlap, which is accurate because both of the MPs are loaded with the same *E.coli* concentrations ($c = [2\ cm]$).

After the analysis and calculations of the velocities for all samples (for two different chips), the script nr.5 {Appendix C] was executed and the data were represented in the form of box plot [see Figure 3.3.24 and Figure 3.3.25]. All of the MP (for all samples and both of the chips) were manipulated with the same current value: $53\ mA$.

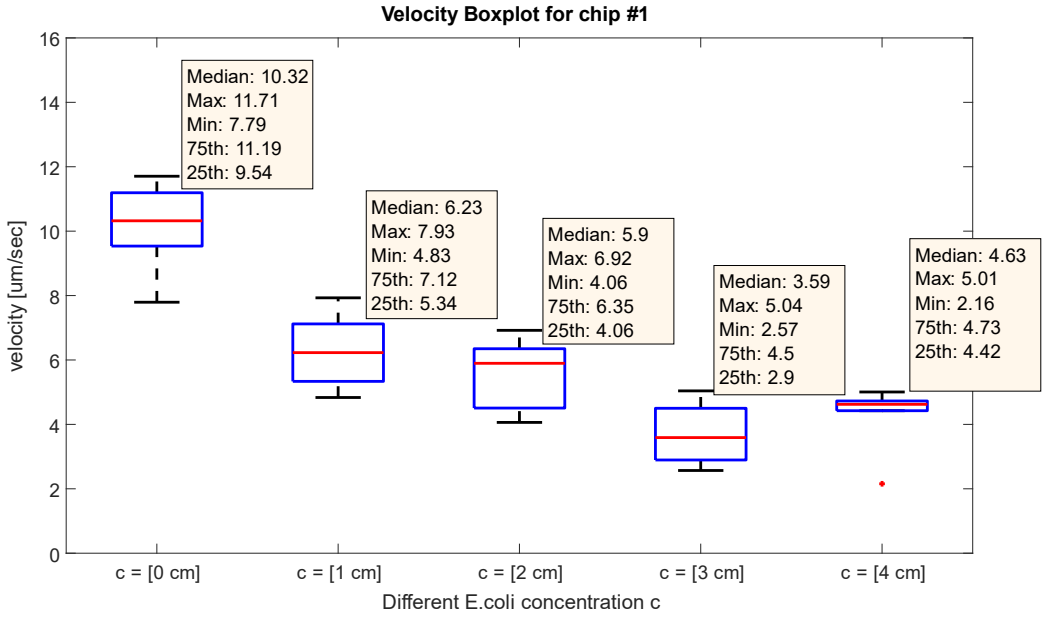


Figure 3.3.24: 1st chip: The velocities of manipulated MPs for different *E.coli* concentrations

With a 95% confidence, we can conclude that for the 1st chip the true medians differ [123] among various concentrations. The size of whiskers[52] (black) contains the information about the size of events (i.e. the amount of velocities collected within a given *E.coli* concentration). Their length is specified as 1.0 times the interquartile range. It can be seen that the size of the whisker for the $4\ cm$ sample is the smallest. The velocities collected within that sample contain information about only little jumps. These could affect the calculated median velocity and creation of outliers (displayed by '+' marker). The upper and lower limits of the segments (blue) define the75th and 25th percentile which correspond to the 3rd and 1st quartile of data. From the graph, it can be seen that the velocity of manipulated MP drops with increased concentration.

[52] *The length of whiskers is specified as 1.0 times the interquartile range*

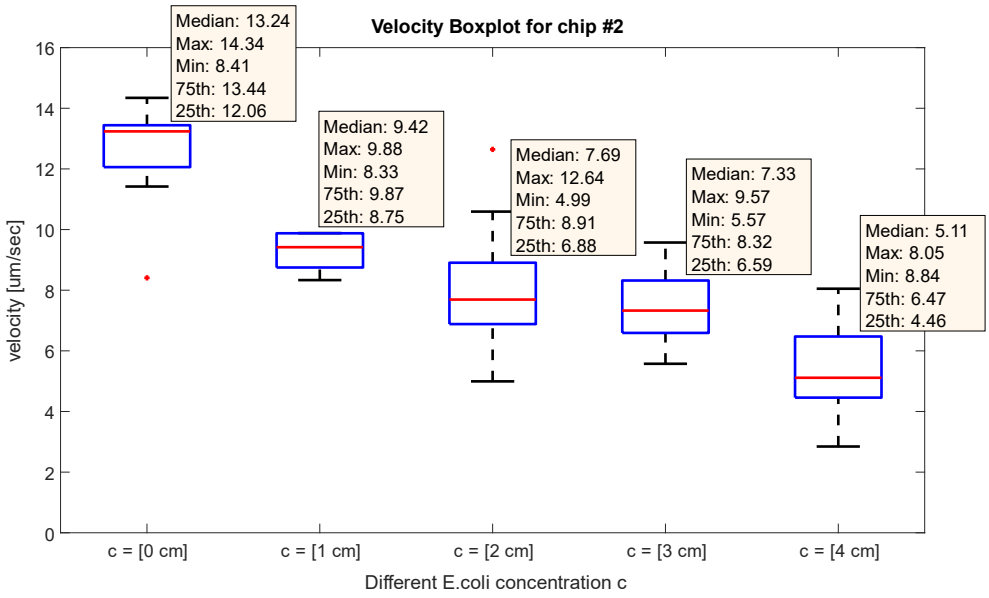


Figure 3.3.25: 2nd chip: the velocities of manipulated MPs for different *E.coli* concentrations

Similarly, as for the 1st chip, the decrease in velocity as a response to an increased *E.coli* concentration, was observed [see Figure 3.3.25].

The box-plots above represent the velocities for the total displacement for the single MPs ' jumps. It could be however seen already during the experiments, that the particles moves with an increased velocity while approaching the MC. In order to compare the changes of velocities with time, the script nr.6 [see Appendix C] was written and Figure 3.3.26, Figure 3.3.27 and Figure 3.3.28 were plotted. A smoothing spline was fitted to the data.

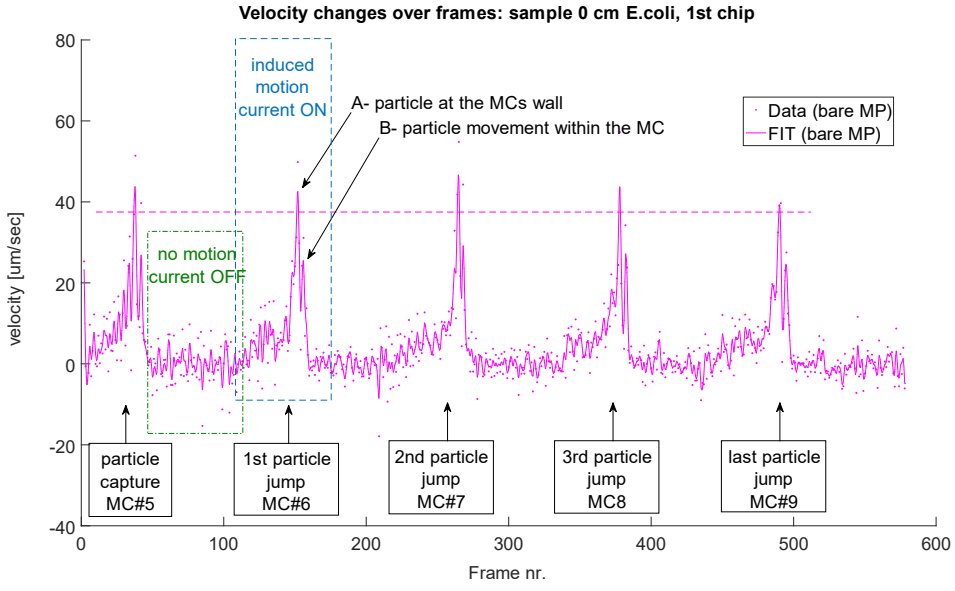


Figure 3.3.26: 1st chip, 0cm sample, particle nr.54: the velocity changes of a MP moving across the MCs sampled at at $\Delta t = 0.04\ sec$. The MP was first captured at MC#5. Afterwards it was moved over MC#6, MC#7, MC#8 until it reached MC#9.

From the obtained graph, it can be concluded that there is an exponential growth of the MP's velocity. There are also two peak velocities for each manipulation. The first peak (higher one) corresponds to the velocity achieved at the MC's edge while the second one represents MP's motion above the MCs until it reaches the center of MC.

Similar plots were drawn to compare differently loaded particles. Figure 3.3.27 represents the changes of velocities for three MPs: one bare MP (there was no attachment visible) and two LMPs.

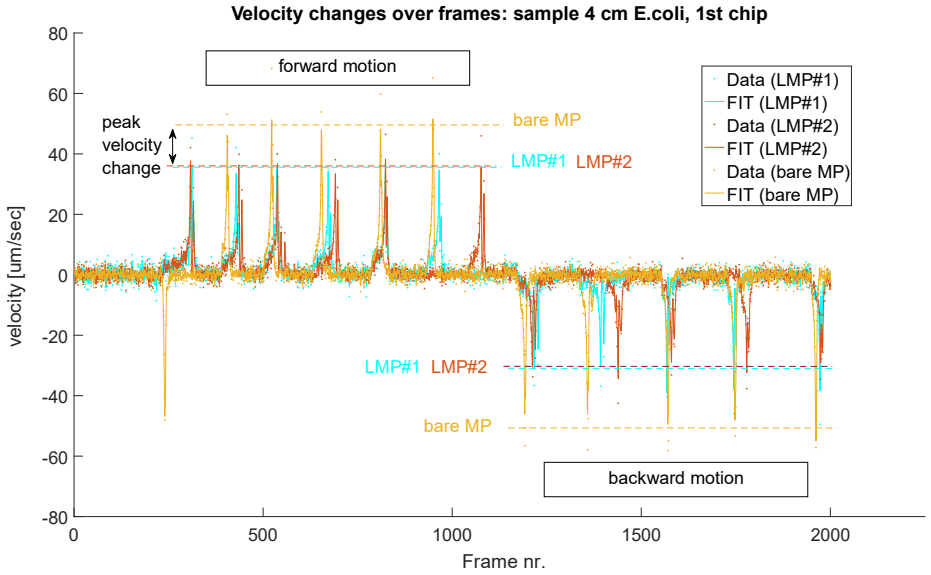


Figure 3.3.27: 2nd chip, 4cm sample: the velocity changes ($\Delta t = 0.04\ sec$) over time for three different MPs moving across the MCs.. The MP was manipulated from the left to the right (forward) and then the direction of manipulation was changed to backwards.

It was observed that for big *E.coli* loadings (i.e. very long chains or multiple rods around *E.coli*) the rotation around the MPs' own axes took place when the direction of the manipulation was changed. This can be explained by the non-uniformity in *E.coli* distribution around the MPs.

Figure 3.3.28 represents the velocity changes for four different magnetic objects (each of them having different volume). The concept of 'velocity change due to volumetric variations' is proved here again. There are visible differences in peak velocities for bare MP, LMP and double MP. The movement experienced by the double MP is the fastest because this particle had the greatest amount of magnetic volume $V_{MP}$ [see equation (2.1.4)] in reference to its non-magnetic volume. Single LMP moved slower that single unloaded MP, because the ratio of magnetic to non-magnetic material is also different here. The non-magnetic volume increases with *E.coli* attachemts (as in the case of LMP).Therefore the hydrodynamic force exerted on single LMP was greater than on the unattached MPs.

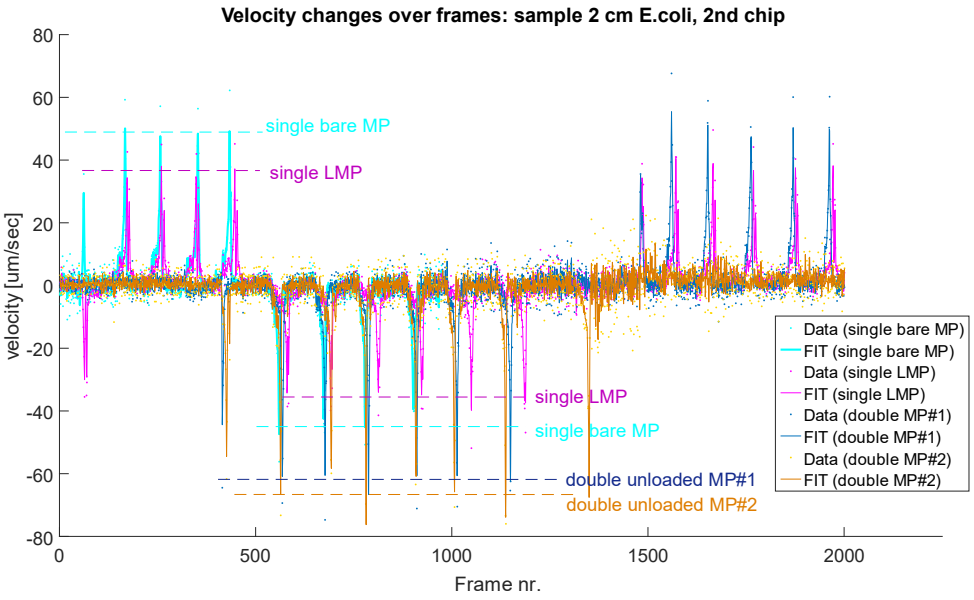


Figure 3.3.28: The velocity changes over the sequence of frames calculated for four different objects: bare MP, LMP and two double MPs. There is a visible difference in peak velocities between the tracked objects.

Lastly, the plots were drawn (see script nr.7 in Appendix C) to verify the lengths of the MPs' displacements and compare them with the real dimensions of the MCs. The chip was designed to have $10\ \mu m$ wide MC that are distenced at $8\ \mu m$ [see Figure 2.3.3]. The difference between the calculated data cursor (positions of MP where its velocity was at the highest) from Figure 3.3.29 gave the value of the distance for a single 'jump' manipulation:

$$(184.4\ -148.7)/2 = 17.85\ \mu m \approx 18\ \mu m \qquad (3.3.1)$$

which corresponds to the real distance between two MCs (i.e. calculations obtained from the tracking coincide with the real dimentions of the chip's design).

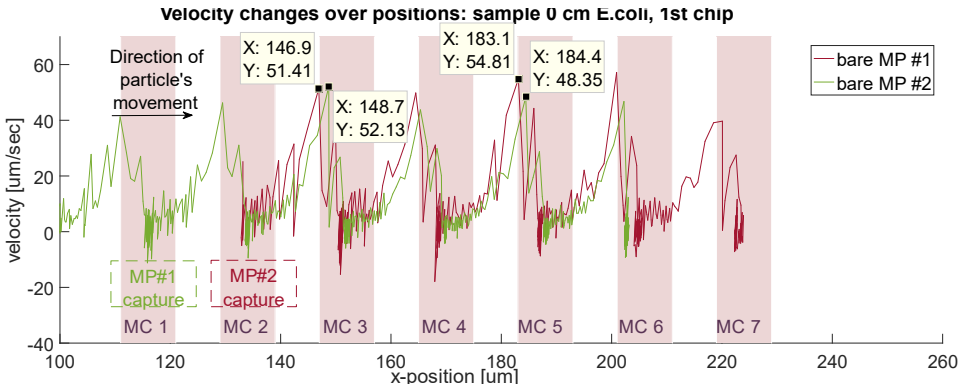


Figure 3.3.29: 1st chip, 0cm: the velocity changes over the x-positions for two bare MPs (green and dark red lines) and estimated positions of MC (seven pink areas). The X-positions for peak velocities were extracted from the graph to verify the distance covered by the manipulated MP. Calculations were compare it to real dimensions of MCs.

The same distance was also calculated for the 2nd chip $(150.7 - 114.6)/2 = 18.05\ \mu m$, which also proved the reliability of the tracked trajectories [(see Figure 3.3.30).]

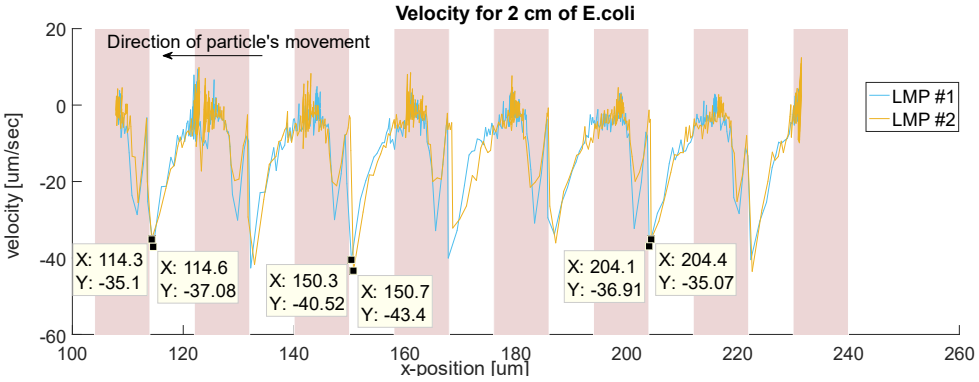


Figure 3.3.30: 2nd chip 2cm: the velocity changes over the x-positions for two LMPs and estimated positions of MCs. The X-positions for peak velocities were extracted from the graph to verify the distance covered by the manipulated MP. Calculations were compared with real dimensions of MCs.

# 4. Conclusions and Outlook

The main goal of the current study was to analyze the effect of volumetric changes of bacteria-conjugated-MPs on their Brownian and Magnetophoresis dynamics while being suspended in micro-sized liquids. In this thesis, the feasibility of the particle tracking software was tested and an *E.coli* bacteria binding protocol was evaluated. Returning to the hypothesis posed at the beginning of the study, it is now possible to state that both of the presented methods can be utilized for detection and quantification of biological agents. The relevance of the MP-*E.coli* compound's dynamics is clearly supported by the findings obtained from the tracked trajectories. The results of the investigation showed that the Brownian's displacement and the magnetophoresis's velocity vary with different *E.coli* attachments. It was found that with the increase of *E.coli* amount within the original (intake) sample, the mean squared displacements or the velocity of the 'induced-motion' particle was decreased. Therefore, it can be said that the parameters obtained from these methods emerged as reliable predictors for *E.coli* concentrations.

Theoretical assumptions are proved by empirical findings and the following conclusions can be drawn. For the Magnetophoresis method: the changes in LMPs' induced velocity are associated with their overall, non-magnetic volume due to the Stokes' drag force (greater volume and altered hydrodynamic shape affected the motion). For the Brownian method: the calculated hydrodynamic diameter obtained from the analysis of the tracked particle's trajectory relates to the diffusive abilities of differently loaded MPs.

The presented work makes several noteworthy contributions to understanding the dynamics of biological microliquids: the behavior of LMPs imposed to magnetic field gradient, the formation of MP-*E.coli* compounds under various environmental conditions or random, non-imposed microscopic movements of *E.coli* and/or MPs.

Perhaps the most serious disadvantages of the presented methods are: adjusting the sample so that the number of individual particles within the microscope FOV view is sufficient for obtaining reliable tracking results (Brownian) or avoiding biofouling on the chip for very big *E.coli* concentrations (Magnetophoresis). Notwithstanding these limitations, the platforms offer quick, inexpensive and compact approaches for *E.coli* detection and quantification and have several practical applications. Although they were restricted to experimental examination of *E.coli* comprised solvent, the studies have confirmed that micro-size precision is achievable and therefore the system could be also applied for obtaining clinical information about the diverse liquid contents where other pathogenic micro-agents are present.

## 4.1. Future improvement

Further research in the field of surface modification would be of a great help for Brownian method if 2D tracking is achieved to get even more accurate results. This suggestion, together with the improved camera settings (fps) could provide more detailed information about thermal fluctuations within the liquid. Dynamic response of bacteria exposed to different external conditions could be examined and x- and y-displacements could be compared. It is suggested that the association of factors such as temperature and viscosity is investigated in future studies and different buffer solutions are tested.

Considerably more work needs to be done to apply peak detection algorithm for graphs obtained from the magnetophoresis method. To avoid errors arising from manual switching ON and OFF the current, an automated platform should be applied and synchronized with the appropriate sequence of frames for the manipulation along the MCs array. By introducing such programmable, fully automated microcontroller, the exact time of the start and the stop of the motion could be determined and high accuracy and high precision of the calculated velocity together with reduced operation's time would be achieved. Another possible area of future research is

to investigate the effect of antibodies outer charge on the chip's biofouling and developing improved chip's surface modification.

Moreover, the calibration of the systems and validation of the results must be conducted to determine the real ranges corresponding to the specific concentration of bacteria within samples.

# Appendix A SPIE Conference proceedings

## Dark field imaging system for size characterization of magnetic micromarkers

A.Malec, C.Haiden, G.Kokkinis, F. Keplinger, I.Giouroudi

Vienna University of Technology, Institute of Sensor and Actuator Systems, 1040 Vienna, Austria
Austrian Centre of Competence for Tribology, 2700 Wiener Neustadt, Austria

*Email: ioanna.giouroudi@tuwien.ac.at: phone +43 1 58801 76691

**ABSTRACT**

In this paper we demonstrate a dark field video imaging system for the detection and size characterization of individual magnetic micromarkers suspended in liquid and the detection of pathogens utilizing magnetically labelled *E.coli*. The system follows dynamic processes and interactions of moving micro/nano objects close to or below the optical resolution limit, and is especially suitable for small sample volumes (~ 10 µl). The developed detection method can be used to obtain clinical information about liquid contents when an additional biological protocol is provided, i.e., binding of microorganisms (e.g. *E.coli*) to specific magnetic markers. Some of the major advantages of our method are the increased sizing precision in the micro- and nano-range as well as the setup's simplicity making it a perfect candidate for miniaturized devices. Measurements can thus be carried out in a quick, inexpensive, and compact manner. A minor limitation is that the concentration range of micromarkers in a liquid sample needs to be adjusted in such a manner that the number of individual particles in the microscope's field of view is sufficient.

**Keywords**: magnetic markers, dark field video imaging, pathogen detection, Brownian tracking

### 1. INTRODUCTION

#### 1.1 Brownian Motion & 2D-Tracking

The label-free dark field video microscopy method, aimed to enhance contrast, object edges and refractive index gradients, is producing an image comprised of bright spots (corresponding to moving diffusive particles) over a dark background. After filtering frames and reducing noise, hundreds of bright intensity pixels were assigned to equivalent micromarkers on subsequent frames and tracked over time in order to generate trajectories. Random collisions of micromarkers with surrounding molecules due to thermal energy defined as Brownian motion (i.e., small diffusion movement) is described by the Stoke-Einstein equation:

$$D = \frac{k_B T}{3\pi\eta d_P} \qquad (2)$$

where T is the absolute temperature, *D* the diffusion constant determined from trajectory analysis, $k_b$ the Boltzmann constant, $\eta$ the solvent viscosity, and $d_P$ is the marker diameter. For this approach only the resistance

to flow due to liquid viscosity was taken into account (there were no strong interaction forces between particle and sample container observed).

### 1.2 Dark Field Video Scattering Microscopy

When a dark-field image is desired, the illumination setup must be arranged in such a manner that only the scattered light can enter the objective. This can be achieved by applying a sub-stage condenser with a patch stop to provide a hollow cone of light that reaches the specimen (the $NA_{sub\text{-}stage\ condenser}$ has to be ~15% higher than the $NA_{objective}$ )[1], or, if possessing a phase-contrast microscope, a combination of a 100x phase contrast annular ring with a 10x or 20x objective can be used. A dark field image can also be produced by connecting a digital image processor (designed to remove low-frequency components of Fourier spectrum by spatial filtering) to a bright field microscope[2], as well as by inserting an opaque stop in the central plane in conjugate to the aperture plane. In our experiments, a straightforward dark-field microscopy method is used to illuminate the sample from above, so that scattered light is detected by camera, while reflected light is not recorded. This produces an image of bright spots (objects of interests) over a dark background which can be further employed to determine the dynamics of such objects.

### 1.3 Bacterial Samples & their Detection

*E. coli* is a gram-negative, commonly present in nature, rod-shaped bacteria of approximately ~ 0.5 µm width and 2µm length[3]. *Its* envelope consists of three layers: the cytoplasmic membrane, the peptidoglycan (a rigid structure determining the rod shape), and the outer membrane, covered with different surface proteins serving as a binding targets for antibodies[4]. Depending on the strain, *E.coli* can have optionally a flagella assembly (including the K-12 wild strain used for our experiments[5]), and can persist relatively long in sterile soil or water environment, even up to 50 days (the K-12 strain W3110)[6]. Due to its small size optical microscopy studies regarding its quantitative dynamics over a life cycle or in response to modifications of external/internal conditions are limited by optical resolution. When it comes to E. coli detection there are many strategies already available: plating and culturing and the use of biochemical tests, modified agar methods, enzyme-linked immunosorbent assays including immunomagnetic electrochemistry, chemiluminescence enzyme immunoassay, ELISA, immunomagnetic separation with fluorescence staining, FBA ( Fluorescent Bacteriophage Assay) combined with flow cytometry, solid phase fluorescent capillary immunoassay and TRFIA (Time Resolved Fluorescence ImmunoAssay). More recent approaches include Polymerase Chain Reaction (PCR), evanescent-wave fibre optic biosensor, PCR-acoustic wave sensor combination, Surface Plasmon Resonance sensor, interferometric array sensors, impedance (EIS- Electrochemical Impedance Spectroscopy), magnetic (GMR) and cantilever sensors (PEMC- Piezo Excited Millimeter Size) [7].

## 2. MATERIALS AND METHODS

In this research work, magnetic markers Dynabeads ™ M-280 coated with streptavidin and purchased by ThermoFisher[8] were used to label the biological target (wild type K-12 E.coli strain) by the means of Abcam@ ab20640 biotinylated rabbit polyclonal antibody anti-*E. coli*[9]. The loading of the magnetic marker was achieved by strong noncovalent binding between the streptavidin layer of the marker and the biotin molecules attached on the surface of the antibody (such that the biotin-streptavidin lock-and-key coupling system can only be broken under harsh conditions: pH4, high temp or salt concentration[10] ).

For the detection a dark field video microscopy setup was used consisting of: a conventional halogen light source KL 1500 LCD 3000K, an optical system mounted from Thorlabs opto-mechanical components, a camera (MIKROTRON EoSens MC 1362), an objective (Nikon, 10x/0.3 A, WD 17,5) and a camera software (MotionBLITYDirector2 LTR). The image resolution of the system was determined with the use of Thorlabs 1951 USAF Negative Resolution Test Targets, 3" x 3"[11].

**2.1 Tracking Working Principle**

MATLAB script utilizing 2D particle tracking Crocker- Grier algorithm is used to link the exact position (centroids) of objects appearing over subsequent frames[12-13]. Based on this approach, a single frame is processed to detect multiple bright spots (representing particles) over a dark background image (here variability in pixel intensity is used to 'find' a particle). This procedure is repeated (for all of the frames) giving x- and y-coordinates (for each individual particle) which are then linked together to form trajectories[14]. Knowing these displacements, three equations (1), (2) and (3) are used to calculate the particle diameter $d_p$. First, the mean square displacements MSD for each single particle at different time intervals $n\Delta t$ is calculated:

$$MSD = \frac{1}{N-n}\sum_{i=0}^{N-n}((x_i - x_{i+n})^2 + (y_i - y_{i+n})^2) \qquad (3)$$

where $N$ is the total number of frames under investigation, $n$ is related to the- displacement number and is in the range of $n = 1,2,3,\ldots,N-1$, $x_0$ is the x-axis position of a particle in a reference frame and $x_N$ is the position of a particle along the x-axis in the last frame. Substituting the result from equation (1) into the following equation,

$$MSD = 2 * DIM * D * n\Delta t \qquad (4)$$

with $DIM$ - number of dimensions, lead us to $D$ - diffusion coefficient described by the well-known Stokes-Einstein relation in (1) from which $d_p$ can eventually be determined. In our measurements, in 2D particle tracking only the horizontal component $d_x$ (diffusive diameter along the x-axis) is taken into consideration as there is strong sedimentation movement along the vertical axis. Y-components in (2) will not be considered and for equation (3) and $DIM = 1$.

## 3. EXPERIMENTS

**3.1 Resolution**

Using a resolution test chart, the size of a pixel on the recorded frame (determined by camera resolution and the optical system magnification) was calculated to be 0.88 pixels/μm.

**3.2 *E. coli* Sample Preparation**

K-12 wild-type Escherichia coli bacteria were cultured on a plastic disposable petri dish layered with solid plain nutrient AGAR (derived from the polysaccharide agarose) with growth temperature at 37°C and storage temperature at 3°C. Bacteria undergoing investigation equivalent to 1cm gentle stretch intake were washed (centrifuged for 8 min at $4.7 \times 10^3\ rpm$) and vortexed (for 1min $at\ 10^4 rpm$) 3 times in 1 ml 0.01 M PBS–Tween 20 (0.01% v/v). 20 ml of this reconstituted E. coli was mixed with 7μl of original concentration Abcam@ ab20640 biotinylated rabbit polyclonal antibody anti-*E. coli* and incubated for 1h on a multiple rotator (room temperature) to yield binding. Afterwards the sample was again washed 5 times and re-suspended in 100 ml of 0.01 M PBS–BSA (0.1% w/v). Multiple washing was conducted continuously during sample preparation so as to eliminate the risk of unspecific binding. Simultaneously, 100 ml of original concentration Dynabeads ™ M-280 Streptavidin (MPs) was magnetically washed and vortexed 3 times in 1ml 0.01 M PBS–Tween 20 (0.01% v/v) and condensed back to 100 ml. Afterwards the two samples were combined: 1 ml of washed MPs and 40 ml of previously prepared immune complex (E. coli-ab20640), sample were left for 1h to incubate on a multiple rotator to induce uniform biotin-streptavidin binding along the antibody-MP suspension. Next, a PBS-BSA washing buffer was added and the vial was left on a magnetic stand for approximately 1,5 min (during this time, MPs are attracted on the side wall towards the magnet). The sample should never be left on a stand longer than 3min, because otherwise numerous agglomerations are created. Apart from MPs attracted to each other, agglomerations are also imposed by antibodies, which act as 'linkers' between MPs, creating so called 'bridges' with attached *E. coli* among them. In the last step of the binding protocol, the supernatant was carefully discarded from the vial and left *E. coli*-loaded-MPs that were re-suspended in 100 ml (sample B) or in 200 ml (sample C & D) PBS-BSA.

**3.3 Sample Application and Particle Tracking Set-up**

A drop (10µl) of the protocol output product was pipetted on, and covered by, a coverslip (approximately ~ 0.17 mm thickness each), forming a sandwich-like-structure. To avoid spontaneous, permanent attachments of antibodies to the glass surface, the liquid was kept in a constant motion while sealing and mounting on a vertical stage forthwith. This straightforward sample arrangement was proposed to enforce gravitational sedimentation movement, also, to prevent adherence of biological components to coverslips.

The illuminating system was arranged at an angle so that 1$^{st}$ and higher order diffracted light rays can enter the objective lens, (but not the illuminating light 0$^{th}$- order light rays). Videos collected at a rate of 25 frames per second were converted to 1000 frames for each sample (see Figure A1).

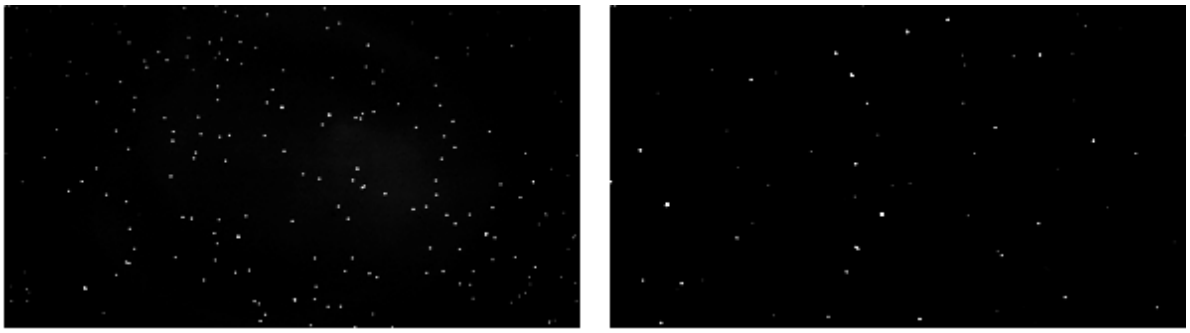

Figure Appendix A1: Darkfield images of samples with bare MPs (on the left) and with MP-E.coli complex (image on the right) after filtering and noise reduction. Small beacon in background corresponds probably to dust however it could be unwashed E. coli as well).

Selected image exposure rate (i.e. 0.04 for each image) was sufficient to capture differences in scattering without disruptive blurring under easy to handle conditions (PBS-BSA as buffer solution having acceptable viscosity, sample treated at room temperature: ~ 25°C - no extra heating/cooling required). Therefore, these attributes, together with commercially available and inexpensive materials (no sub-stage condenser required), constitute a system that is easy to implement. The length of the disc-shaped, individual bright spot (corresponding to one MP), was approximated to 5-7 pixels (i.e. for this optical setup).

The detection of spots in the images (peak detection) was done for sequences of >1000 images. After defining the size of an object, together with other parameters such as mask around a particle (15-17 pixels), pixel noise length (1 pixel), threshold for minimum relative pixel brightness of an object (0.02) and applying bandpass filtering, peck detection generates coordinate data of all peaks in all recorded frames

Tracking of bright spots movements along 1000 successive frames was achieved by linking their position using an estimated linking distance between two subsequent frames (default value of 5 pixels was chosen). This is the maximum displacement of a particle between two consecutive frames and must be set carefully to avoid tracking errors resulting from false particle assignment. Among all tracking paths per multiple objective field of view (sample A, C & D) and per one field of view (sample B), there were: sample A - 219 particles, sample B - 97 particles, sample C - 90 and sample D - 268 particles respectively, specified for further calculations (each path satisfying the requirement of minimum trajectory length of 50 % - i.e. half of the duration of the total processed recordings).

To check if the obtained results were reliable, sample B, C and D were additionally examined under fluorescence microscope (Nikon eclipse 80i with super high pressure mercury lamp under 40x /1.3 oil objective) for presence of *E. coli* attachments (see Figure A2). The biological protocol was extended by adding Abcam@ ab150077 donkey polyclonal antibody anti Rabbit (this secondary antibody was conjugated with fluorophore Alexa Fluor® 488)[15], followed by 10 min incubation and magnetic wash (crucial to reduce fluorescent background noise). Noticeable *E. coli* labeling was observed in all 3 samples for several MPs.

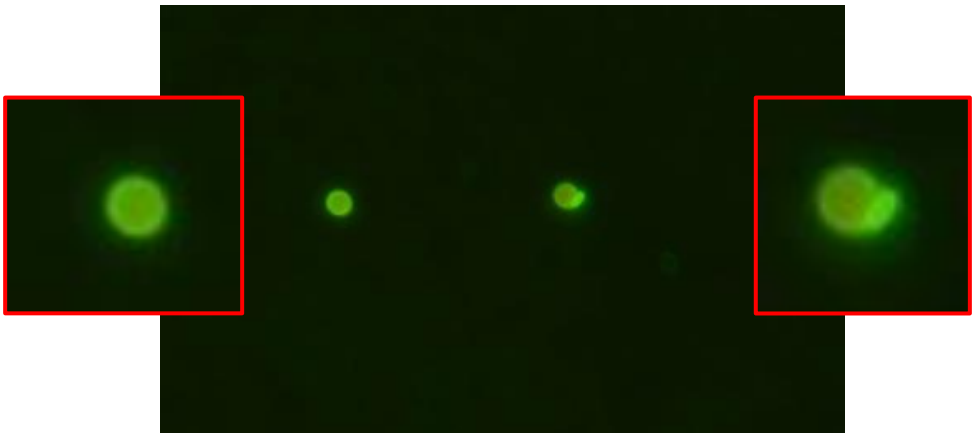

Figure Appendix A2: Fluorescent image of visible E.coli labeling by a magnetic particle M-280 streptavidin (on the right) under 40x oil magnification. No visible E.coli attachment for the MP on the left.

## 4. RESULTS

To illustrate the results, histograms with estimated size ranges for different objects (Figure A3) and corresponding distribution fitting curves (Figure A4) were prepared.

The fitting curves suggest, that there is a visible shift to the right along the x-axis between reference (bare MPs) and *E. coli* loaded MPs. It has been found that there is a good match between this shift (786 nm for sample B), 586 nm-sample C and 491nm-sample D) and the real size of the attached biological component: the streptavidin size of a macromolecule or protein:~ 15-20nm, the size of biotin ~ 32Å, the Y-shaped antibody size ~ 13nm, and the size of E.coli ~ 0.5 µm. One question still unanswered is whether the difference between calculated peak diameter for bare MPs (2367nm) and their actual size (2800 nm) comes from temperature changes (e.g. heating of sample), induced motion of a liquid, contamination of the sample or maybe from the distribution fitting method. The findings are of direct practical relevance and work on the remaining issues is continuing and will be presented in future work.

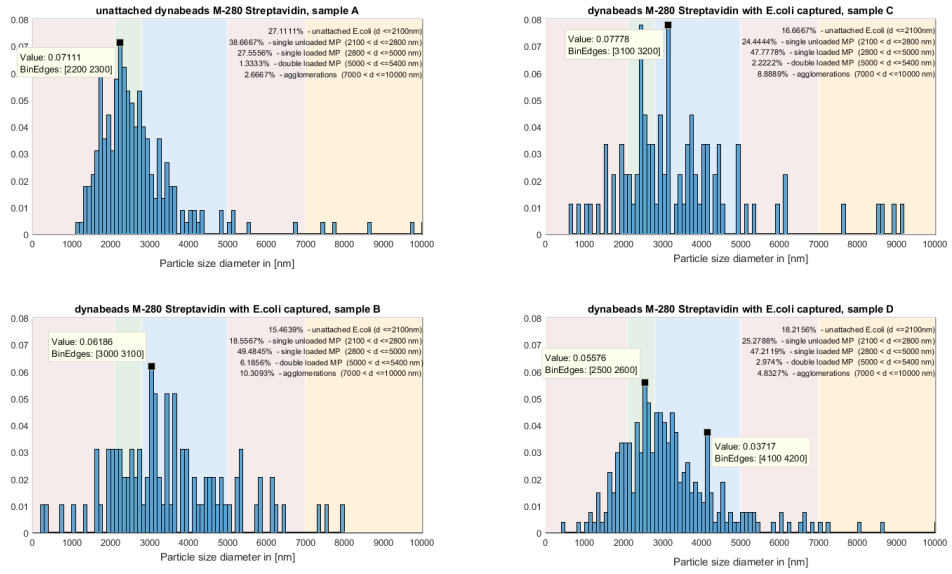


Figure Appendix A3: Graphics representing particle size distribution for 4 samples. Sample A – bare MP without E. coli. Sample B, sample C and sample D – MP with attached E. coli (1cm wild type K-12 bacteria intake cultured on AGAR petri dish). Histograms are created in MATLAB using the 'probability' normalization. The height of each bar is equal to the probability of selecting an observation within 100 nm bin interval. Height of all the bars sums to 1. $v_i = \frac{c_i}{N}$, where $v_i$- is the bin value, $c_i$- the number of element in the bin and N – the number of

elements in the input data. Coloured areas correspond to estimated ranges for different particle groups resulting from a binding protocol.

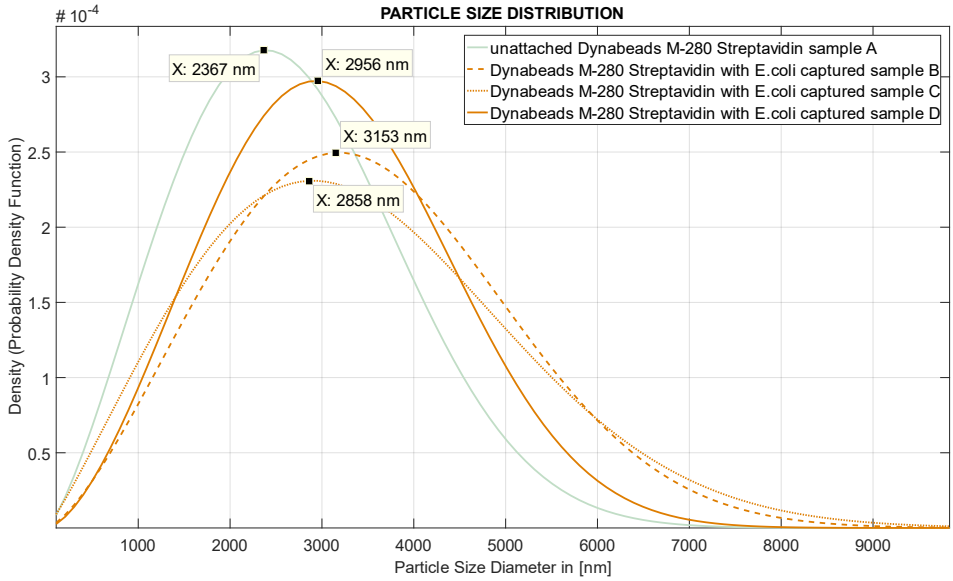


Figure Appendix A4: Weibull distribution fitting curves applied for data from Figure  with corresponding highest peaks. There is a visible shift to the right along the x-axis for samples B,C & D (orange) where E. coli was added in reference to the bare MP -sample A (light green).

## 5. CONCLUSIONS AND OUTLOOK

The results obtained indicate that the developed dark field video imaging system is a compact, inexpensive approach for the detection of biological markers and pathogens suspended in a small volume liquid sample. In our future research, we intend to conduct experiments to determine whether the proposed technique is applicable not only for E. coli detection but also for quantification. Further study of the issue using different E. coli concentrations would be of interest. This approach has the potential to be applied not only for detection of E. coli but also for a variety of microorganisms if the appropriate biological binding/labeling protocol is provided as well as for obtaining information about dynamics in life cycle of single/multiple *microorganism(s) in response to condition/environmental changes.*

## REFERENCES


[1] Boas, David A., Constantinos Pitris, and Nimmi Ramanujam. Handbook of Biomedical Optics. CRC Press, 2016: 485-486

[2] Wayne, Randy O. Light and Video Microscopy. Academic Press, 2013: 111-113

[3] Reshes, Galina, Sharon Vanounou, Itzhak Fishov, and Mario Feingold. “Cell Shape Dynamics in Escherichia Coli.” Biophysical Journal 94, no. 1 (January 1, 2008): 251–64. doi:10.1529/biophysj.107.104398.

[4] Navarre, William Wiley, and Olaf Schneewind. “Surface Proteins of Gram-Positive Bacteria and Mechanisms of Their Targeting to the Cell Wall Envelope.” Microbiology and Molecular Biology Reviews : MMBR 63, no. 1 (March 1999): 174–229.

[5] Maurer, Lisa M., Elizabeth Yohannes, Sandra S. Bondurant, Michael Radmacher, and Joan L. Slonczewski. “pH Regulates Genes for Flagellar Motility, Catabolism, and Oxidative Stress in Escherichia Coli K-12.” Journal of Bacteriology 187, no. 1 (January 2005): 304–19. doi:10.1128/JB.187.1.304-319.2005.

[6] Bogosian, G, L E Sammons, P J Morris, J P O’Neil, M A Heitkamp, and D B Weber. “Death of the Escherichia Coli K-12 Strain W3110 in Soil and Water.” Applied and Environmental Microbiology 62, no. 11 (November 1996): 4114–20.

[7] Mohammed Zourob,Souna Elwary,Anthony Turner. “Principles of Bacterial Detection: Biosensors, Recognition” Springer. 978-0-387-75112-2

[8] “DynabeadsTM M-280 Streptavidin - Pub. No. MAN0014017 - Rev. A.0 - MAN0014017_Dynabeads_M280_Streptavidin_UG.pdf.”. https://tools.thermofisher.com/content/sfs/manuals/MAN0014017_Dynabeads_M280_Streptavidin_UG.pdf.

[9] “E-Coli-Antibody-Biotin-ab68451.pdf.”. http://www.abcam.com/E-coli-antibody-Biotin-ab68451.pdf.

[10] Claire-Marie Pradier and Yves Jean Chabal, Biointerface Characterization by Advanced IR Spectroscopy (Elsevier, 2011). page 84

[11] “QTN007815-E0W - R3L3S1N-AutoCADPDF.pdf.” https://www.thorlabs.com/drawings/ab79cd0ca3ab6f98-700D0C2F-5056-0103-79E4DEFFF59E299E/R3L3S1N-AutoCADPDF.pdf.

[12] Haiden, Christoph et al. ‘Sizing of Metallic Nanoparticles Confined to a Microfluidic Film Applying Dark-Field Particle Tracking’. Langmuir 30.31 (2014): 9607–9615. ACS Publications. Web.

[13] Haiden, C. et al. ‘A Microfluidic Chip and Dark-Field Imaging System for Size Measurement of Metal Wear Particles in Oil’. IEEE Sensors Journal 16.5 (2016): 1182–1189. IEEE Xplore. Web.

[14] Haiden, C. et al. ‘Concurrent Particle Diffusion and Sedimentation Measurements Using Two-Dimensional Tracking in a Vertical Sample Arrangement’. Applied Physics Letters 108.9 (2016): 094101. aip.scitation.org (Atypon). Web.

[15] “Goat Anti-Rabbit Alexa Fluor® 488 (IgG H&L) (ab150077).”. http://www.abcam.com/goat-rabbit-igg-hl-alexa-fluor-488-ab150077.html.

## ACKNOWLEDGMENTS

The Institute of Sensor and Actuator Systems acknowledges the financial support of the Austrian Science Fund (FWF) with Project No. P28544-N30. Parts of this work were also funded by the Austrian COMET Programme (Project K2 XTribology, No. 849109).

# Appendix B Lookup table for '1951 USAF resolution test chart'

| | Width of 1 line [in µm] | | | | | | | | | | |
|---|---|---|---|---|---|---|---|---|---|---|---|
| | Group Number | | | | | | | | | | |
| Element | | -2 | -1 | 0 | 1 | 2 | 3 | 4 | 5 | 6 | 7 |
| | 1 | 2000 | 1000.00 | 500.00 | 250.00 | 125.00 | 62.50 | 31.25 | 15.63 | 7.81 | 3.91 |
| | 2 | 1781.80 | 890.90 | 445.45 | 222.72 | 111.36 | 55.68 | 27.84 | 13.92 | 6.96 | 3.48 |
| | 3 | 1587.40 | 793.70 | 396.85 | 198.43 | 99.21 | 49.61 | 24.80 | 12.40 | 6.20 | 3.10 |
| | 4 | 1414.21 | 707.11 | 353.55 | 176.78 | 88.39 | 44.19 | 22.10 | 11.05 | 5.52 | 2.76 |
| | 5 | 1259.92 | 629.96 | 314.98 | 157.49 | 78.75 | 39.37 | 19.69 | 9.84 | 4.92 | 2.46 |
| | 6 | 1122.46 | 561.23 | 280.62 | 140.31 | 70.15 | 35.08 | 17.54 | 8.77 | 4.38 | 2.19 |

Table B.1: Lookup table for width in [µm] of one bar within a specific group and element in USAF Resolving Power Target 1951.

# Appendix C MATLAB scripts

### MATLAB script for representation of MPs' dynamics (Brownian)

```
%% Script 1 to represent distribution (normalized histogram) of the calculated hydrodynamic radius and the PDF fit curve. Below script covers only a single sample representation: 'samplePlainMP'. For representation of multiple samples simultaneously, GUI was created. Within the GUI, different parameters can be edited (in textbox and sidebars) including limits for outliers and estimated areas for attachments.GUI script is not enclosed here.

[filename, folder]  = uigetfile('*.xls', 'Select excel file');%The desired output of the tracking software is selected here by the user. 'OUT-sizes(1000).xls' file.
Analyzed_File = fullfile(folder, filename);
data=load(Analyzed_File);
samplePlainMP=data(:,9);% selecting 9th column where calculated hydrodynamic radius were saved
samplePlainMP = samplePlainMP(:);% Force all inputs to be column vectors
%% --- Plot normalized histogram independently and calculate the procent of counts within defined limits/lines
h=histogram(samplePlainMP,'Normalization','probability','BinMethod','fd');
h1=get(gca, 'Children');h1.BinWidth=100;
line1=2100;line2=2800;% line3=4500nm; line4=7000; line5=10000; %seting the limits for areas for estimated MP-E.coli size
sorted=sort(samplePlainMP);
    positionIndex=find(sorted<=line1,1,'last');
    k=0;
    for i=1:positionIndex
        k=k+1;
    end
CountsBelowFirstLine=k;
suma=size(samplePlainMP,1);
CountsBelowFirstLineinProcent=CountsBelowFirstLine*100/suma;% counts of unattachedE.coli
% CountsBetweenSecondandFirst=CountsBelowSecondLine-CountsBelowFirstLine;
% %% counts for different regions were calculated analogously.
%% --- Create fit "samplePlainMP FIT"
figure; XGrid = linspace(0,10000,1000);% y = linspace(x1,x2,n) generates n points. The spacing between the points is (x2-x1)/(n-1).
Excluded = (samplePlainMP > 0 & samplePlainMP < 10000);% Create vector for exclusion rule '10000'; % Vector indexes the points that are included
Data = samplePlainMP(Excluded);
pd1 = fitdist(Data,'kernel','kernel','epanechnikov','support','unbounded');% defining properties of fitting curve
YPlot = pdf(pd1,XGrid); %probability density function
hLine = plot(XGrid,YPlot);hold on;
% --- Plot data originally in dataset "samplePlainMP data"
[CdfF,CdfX] = ecdf(samplePlainMP,'Function','cdf');  % compute empirical cdf
BinInfo.rule = 5; BinInfo.width = 100; BinInfo.placementRule = 1;
[~,BinEdge] = internal.stats.histbins(samplePlainMP,[],[],BinInfo,CdfF,CdfX);
[BinHeight,BinCenter] = ecdfhist(CdfF,CdfX,'edges',BinEdge);
hLine = bar(BinCenter,BinHeight,'hist');
xlabel('Diameter [nm]');ylabel('Density')
% The above code was modified to obtain multiplePDF fitting curves on one plot.
```

### MATLAB script for representation of MPs' dynamics (Magnetophoresis)

```
%before running the script 'linked' variable from output tracking routine of a corresponding manipulation attempt must be loaded into a workspace. 'linked' variable contains, inter alia, information about positions of MPs' centroids over the sequence of frames


%% Script 2 written to represent the particle XY axis displacement in [pixels]
Res=6.1; % resolution, resolving power of a chart in [pixels/micrometers]
DistBetweMC=20 % real distance between centroids of adjacent microconductors in [micrometers]
MinDistPart=3 % minimum distance along x-axis displacement that must be traveled by a particle to be further analyzed. '3' means that particle had to move at least at the distance of three MCs (i.e. 3*20=60 micrometers)
DistLim= DistBetweMC*MinDistPart*Res
sample=0; video=' DSC0149'; tracking=' 13h42m45s'; chip='1stchip'; % video currently being analyzed
```

```
np=[]; legendInfo=[];
[rFOV, cFOV]=size(linked{1,end}); %% cFOV- give information how many data(FOVs) were loaded
figure1 = figure('Name',['XY position for all particles  ' num2str(sample) 'cm of E.coli ' video
' ' tracking ' ' chip]); hold on;
for j=1:cFOV
    [r, np]= size(linked{1,end}{1,j});np=np-2; %%np-give information about number of detected
particles in a specific FOV
    for i=1:np
        time=[];
        [rp, cp]=size(linked{1,end}{1,j}{1,i});%% rp- give information about specific single
detected particle, i.e. how long was its trajectory
        for k=2:rp
            time=[time,0.04*k];%%0.04 corresponds to 25fps
        end
        maxXpos=max(linked{1,end}{1,j}{1,i}(:,1));
        minXpos=min(linked{1,end}{1,j}{1,i}(:,1));
        DisplXaxis=maxXpos-minXpos;
        if DisplXaxis>DistLim
            p=plot(linked{1,end}{1,j}{1,i}(:,1),linked{1,end}{1,j}{1,i}(:,2));%%      plotting
displacement along X and Y axes in [pixels]
            label(p,[num2str(i) ],'location','right')% indexing particles
    %         p.Color(4)=i*(1/np);%for better visualization purposes
    %         p.LineWidth=(4/np)*(np+1-i);%for better visualization purposes
            [legSizR, legSizC]=size(legendInfo);
            legendInfo{legSizC+1}=[ 'Particle nr. ' num2str(i) '    FOV' num2str(j) ];
        end
    end
end
legend(legendInfo);xlabel({'position x [pixels]'});ylabel({'position y [pixels]'});
title({['Frame XPosition for selected particles  ' num2str(sample) 'cm of E.coli ' video ' '
tracking ' ' chip]});
xlim([0 1920]);ylim([0 1080]); % to display entire FOV (not only a specific displacement) for
comparison purpose with other manipulation attempts
set(gca,'Ydir','reverse'); to get the same orientation as jpg frame has
```

```
% Script 3 written to represent the particle displacement over the sequence of all frames
[r, np]= size(linked{1,end}{1,1})
POI={1:np-1};
figure1 = figure('Name',['Frame XDisplacement for selected particles  ' num2str(sample) 'cm of
E.coli ' video ' ' tracking]); hold on;
np=[]; cmap=[]; legendInfo=[];
[xpoi, ypoi]=size(POI);
for j=1:cFOV
    [r, np]= size(linked{1,end}{1,j}); %%np-give inf about number of detected particles in a
specific FOV
    cmap=jet(cFOV);
    for l=1:ypoi
        for i=POI{l}
            maxXpos=max(linked{1,end}{1,j}{1,i}(:,1));
            minXpos=min(linked{1,end}{1,j}{1,i}(:,1));
            DisplXaxis=maxXpos-minXpos;
            if DisplXaxis>DistLim
                p(i)=plot((linked{1,end}{1,j}{1,i}(:,1))/Res,linked{1,end}{1,j}{1,i}(:,3));
                [legSizR, legSizC]=size(legendInfo);
                legendInfo{legSizC+1}=['Particle nr ' num2str(i) '    FOV' num2str(j) ];
            end
        end
    end
end
legend(legendInfo);xlabel({'X-axes      position      [in      micrometers]'});ylabel({'Frame
number'});title({['Frame XPosition for selected particles  ' num2str(sample) 'cm of E.coli '
video ' ' tracking]});
```

```
%% script 4: for calculation of velocity, writing it on the plot and saving it to ONE variable
'VelocityDataSheet' for all chips.
%% load cursor info before running the script. 'Export cursor data to workspace'
fps=25; deltat=1/fps;
if isempty(VelocityDataSheet)
    VelocityDataSheet{1,1}=1; VelocityDataSheet{1,2}=2;
    for chip=1:2
        for cm=0:4;VelocityDataSheet{2,chip}{cm+1}=num2str(cm);end
    end
end
Userchip = 'which chip is it?      '; Chipstr = input(Userchip,'s'); chip=str2num(Chipstr);
Concentrationstr ='1cm'; conctr=1; Moviestr='DSC_0149'; TrackingNrstr='13h42m45s'; %user
deifined description of tracking parameters
```

```
a=[cursor_info.Position]; %% 'cursor_info' is a variable that was previously exported to
workspace. It was exüprted manually by right mousse clikc 'export cursor data to workspace'
Yposition = a(2:2:length(a)); %consequent Y positions of all cursors
Xposition = a(1:2:length(a));%consequent X positions of all cursors
x=diff(Xposition); Xmanipulation = x(1:2:length(x)); % in micrometers
y=diff(Yposition); Ymanipulation=y(1:2:length(y)); % in frames
Ymanipulation=Ymanipulation*deltat; % time step between two frames
newdata=Xmanipulation./Ymanipulation; %here the velocity is calculated for each displacement
[sxnd, synd]=size(newdata);
j=1;
for k=1:synd
    str = [num2str(newdata(k)), '\mum/s'];
    xposstart=Xposition(j); yposstart=Yposition(j);
    xposend=Xposition(j+1); yposend=Yposition(j+1);
    xpos=mean([xposend,xposstart]); ypos=mean([yposend,yposstart]);
    j=j+2;
    textBox=text(xpos+2,ypos,str); % writing calculated velocity on the plot
    set(textBox,'VerticalAlignment','top'); set(textBox,'HorizontalAlignment','center');
%seting position of textbox
end
[sxDS, syDS]=size(VelocityDataSheet{2,chip});
try
   [sxconc, syconc]=size(VelocityDataSheet{2,chip}{2,conctr+1});
catch
    sxconc=0; syconc=0;
end
VelocityDataSheet{2,chip}{2,conctr+1}{1,syconc+1}=['movie:',Moviestr,' particle:' ,
TrackingNrstr];
VelocityDataSheet{2,chip}{2,conctr+1}{2,syconc+1}(1:synd,1)=newdata(:);
```

**%% script 5 for plotting boxplot Velocity**

```
for cm=1:5
    [sx0 sy0]=size(VelocityDataSheet{2,chip}{2,cm});
    c{1,cm}=[];clear i
    for i=1:sy0
        [sx00, sy00]=size(VelocityDataSheet{2,chip}{2,cm}{2,i}); clear k;
        for k=1:sx00
            singlevel= abs(VelocityDataSheet{2,chip}{2,cm}{2,i}(k,1));
            c{1,cm} =[c{1,cm}, singlevel];
        end
    end
end
for cm=1:5%% preparing variable to be loaded for boxplot
    len=length(c{1,cm}(1:end));
    cnew(1:len,cm)=c{1,cm}(1:end);
end
cnew(cnew == 0) = NaN;
figure;boxplot(cnew,'Labels',{'cm = 0','cm = 1','cm = 2','cm = 3','cm = 4'});
```

**%% script 6: to plot velocities for all tracked particles over frames (with a fit)**

```
np=[];cmap=[];legendInfo=[];[rFOV, cFOV]=size(linked{1,2}); %%cFOV-give inf how many
data(FOVs) were loaded
Res=7.2;
ft = fittype( 'smoothingspline' ); %% Seting up the fittype
figure1 = figure('Name','Velocity for all particles'); hold on;
for j=1:cFOV
    [r, np]= size(linked{1,2}{1,j});np=np-2; %%np-give inf about number of detected particles
in a specific FOV
    cmap=jet(cFOV);
    for i=1:np
        frame=[];
        [rp, cp]=size(linked{1,2}{1,j}{1,i});%%rp-give inf about specific single detected
particle, i.e how long was its trajectory
        for k=2:rp; frame=[frame,k]; end
        velocity=((diff(linked{1,2}{1,j}{1,i}(:,1)))/0.04)/Res;
        [xData, yData] = prepareCurveData( frame, velocity' );
        [fitresult, gof] = fit( xData, yData, ft, 'Normalize', 'on' );  % Fit model to data.
        h = plot( fitresult, xData, yData );
        h(2).Color=cmap(j,:);  h(2).LineWidth=(4/np)*(np+1-i);
        [legSizR, legSizC]=size(legendInfo);
        legendInfo{legSizC+1}=['Data']; legendInfo{legSizC+2}=[ 'Particle nr ' num2str(i) '
FOV' num2str(j) ];
    end
end
```

```
legend(legendInfo);xlabel({'Frame nr.'});ylabel({'velocity [um/sec]'});title({'Velocity graphs for all particles 2800 nm'});
```

**%%Script 7: to plot velocities for all tracked particles (from different FOVs)over positions**

```
np=[];legendInfo=[];
[rFOV, cFOV]=size(linked{1,end}); %%cFOV-give inf how many data(FOVs) were loaded
Res=7.2; sample=4;
figure1 = figure('Name','Velocity for all particles'); hold on;
for j=1:cFOV
    [r, np]= size(linked{1,end}{1,j});np=np-2; %%np- amount of detected particles in a specific FOV
    for i=1:np
        time=[];
        [rp, cp]=size(linked{1,end}{1,j}{1,i});%%rp-length of trajectory of specific particle
        xpos=linked{1,end}{1,j}{1,i}(2:end,1)/Res;
        p=plot(xpos,((diff(linked{1,end}{1,j}{1,i}(:,1)))/deltat)/Res);%% V=deltaX/deltaT
        legSizR, legSizC]=size(legendInfo); legendInfo{legSizC+1}=[ 'Particle nr ' num2str(i) '    FOV' num2str(j) ];
    end
end
legend(legendInfo);xlabel({'x-position [um]'});ylabel({'velocity [um/sec]'});title({['Velocity for ' num2str(sample) ' cm of E.coli'  ]});
```

# Appendix D Binding Protocol

The compound was prepared by adapting and modifying the binding procedure reported in [124].

### A. Preparation of PBS-BSA 0.1%

i. $5\ ml$ of original *Roti®-Stock* $10 \times PBS$ was diluted in $45\ ml$ of DI water.

ii. Next, $49.5\ ml$ of the above obtained solution (1% PBS from step i.) was mixed with $500\ \mu l$ of *original Blocker™ BSA* $(10\%)$ *in PBS* [see Figure 3.2.6]. And as a result, 0.1% PBS-BSA buffer solution was obtained.

### B. Preparation of PBS-T 0.01%

iii. $5\ \mu l$ of original ween® 20 [see Figure 3.2.6] was diluted in $50\ ml$ of 1% PBS. As a result, 0.01% PBS-Tween solution was obtained.

### C. Bacteria washing

1. Required amount ($\underline{1\ cm}$, $\underline{2\ cm}$, etc.) of bacteria loop smear [see Figure 3.2.10] of wild-type K-12 *E.coli* strain was suspended in $1\ mL$ *PBS-Tween (0.01%).*
2. The vial was placed on vortex mixer [see Figure 3.2.7] for $\sim 1\ min$ at maximum rotational speed $\omega_{cyc} = 2500\ rpm$ to syncretize clumps of bacteria with an aqueous medium.
3. After obtaining uniform, homogenous mixture, centrifugation [see Figure 3.2.7] for $\sim 8\ min$ at speed $4.7 \times 10^3\ rpm$ was prepared and immediately followed by gentle removal of supernatant so as to keep bacterial sedimentation intact on the vial's wall.
4. Washed bacteria were suspended in $1\ mL$ *PBS-Tween (0.01%).*
5. Above procedure (step 2, 3 and 4) was repeated 3 times.

### D. Antibody conjugation

6. $7\ \mu l$ of primary antibody Ab20649 (of original concentration $4\ mg/ml$) [see Section 1.5.2 or Appendix F ] was added to previously washed bacteria.
7. To enhance conjugation of antibodies, the sample was positioned for $\underline{1\ hour}$ on programmable multi-rotator [see Figure 3.2.7] at interoperable, rehashed sequence with following parameters: orbital rotation $20\ rpm$ for $5\ sec$, then reciprocal rotation at turning angle $10°$ *for* $5\ sec$ and succeeding vibrational angle $2°$ for $2\ sec$.
8. Once completing incubation process [i.e. step 7], the subject was washed 5 times according to steps 2, 3 and 4 under milder conditions (i.e. vortex mixer at $\omega_{cyc} = 1000\ rpm$ parallel with gentle sample handling). Moreover, instead of using *PBS-Tween* as a washing agent, *PBS BSA* $(0.1\%)$ was conformed to further block nonspecific binding of antibodies. After the last wash, sediment was re-suspended in $\underline{200\ \mu L}$ PBS-BSA to condense the bacteria.

### E. Particle washing

9. $100\ \mu L$ of the original, well mixed [see vortex mixer step 2), solution of Magnetic Particles Dynabeads ™ M-280 Streptavidin [see Section 1.5.4 or Appendix C] was added to $900\ \mu L$ of PBS-Tween (0.01%).
10. To enable separation of solute from the solvent, the obtained mixture was strongly (see step 2) mixed with vortex again and left on Magnetic Separator [see Figure 3.2.8] for $\sim 1\text{-}2\ min$. *Magnetic particles congregated on one side of the vial's wall, were kept intact while pipetting out the buffer solution. Washed MPs were resuspended in* $1\ mL$ *of* PBS-Tween (0.01%).
11. *After repeating magnetic washing procedure (step 10), at the last wash, MPs were resuspended in* $100\ \mu L$-PBS-Tween (0.01%) *to reacquire original concentration of* $10\ mg/mL$.

### F. Magnetic Particle loading

12. Mixing $\underline{40\ \mu L}$ of a compound resulting from procedure D with $\underline{1\ \mu L}$ of output solution from proceeding E was followed by its $\underline{1h}$ incubation on multi-rotator as described in step 7.

13. Obtained solution was diluted in $\underline{200\ \mu L}$ of PBS-BSA (0.1%)
14. Careful magnetic wash was conducted to remove unloaded bacteria. *After the wash, sediment was re-suspended in* $\underline{200\ \mu L}$ *PBS-BSA* (0.1%) to achieve feasible concentration of MPs on microscope's FOV.

### G. *Fluor labelling*

15. Finally, $\underline{1\ \mu L}$ of secondary antibody ab150077 Goat Anti-Rabbit IgG H&L (Alexa Fluor® 488) [see Section 1.5.3 or Appendix F] was added to resulting sample, which was then manually shaken and washed magnetically to remove background noise (i.e. unloaded bacteria and unattached antibodies). Sample was handled very gently (i.e. no vortex, maximum time on a Magnetic Stand Separator: $\underline{\mathrm{t} \approx 1\ \mathrm{min}}$ ) and kept in constant motion to prevent agglomerations.

# Appendix E Properties of Dynabeads™ M-280 Streptavidin and M-270 Carboxylic

## Dynabeads physical characteristics

Dynabeads are uniform, superparamagnetic, porous polystyrene spheres with an even dispersion of magnetic material throughout the bead. The magnetic material within the Dynabeads is a mixture of the two iron oxides maghemite (gamma-$Fe_2O_3$) and magnetite ($Fe_3O_4$), which is encased in the bead matrix by an additional thin polymer shell. This prevents any iron leakage from the beads which could otherwise have a detrimental toxic effects on target cells, while at the same time providing a defined surface area for adsorption or conjugation of various biomolecules.

| Dynabeads type | Diameter $[\mu m]$ | Monodispersity | | Specific surface area $[m^2/g\ DS]$ | Density $[g\ DS/cm^3]$ |
|---|---|---|---|---|---|
| | | SD $[\mu m]$ | CV $[\%]$ | | |
| M-270 Dynabeads | 2.8 | 0.04 - 0.05 | 1.6 - 1.8 | 2 - 5 | 1.6 |
| M-280 Dynabeads | 2.8 | 0.04 | 1.6 | 4 - 8 | 1.4 |

Table E.1: Physical properties of Dynabeads (typical values)

### Magnetic properties of Dynabeads

Due to the small size of the iron domains of the magnetic material in the matrix, Dynabeads are superparamagnetic. This means they will only exhibit magnetic properties when subjected to a magnetic field, and both remanence and coercivity equals zero. This can be seen from the magnetisation curves for the beads below.

**M-280 Dynabeads:**

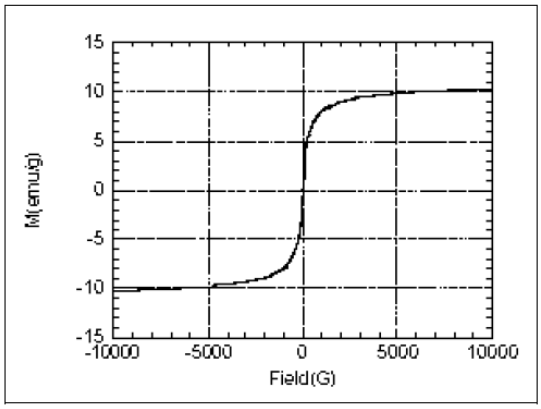


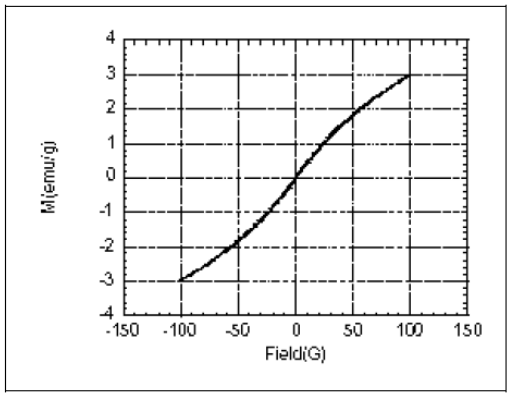

**M-270 Dynabeads:**

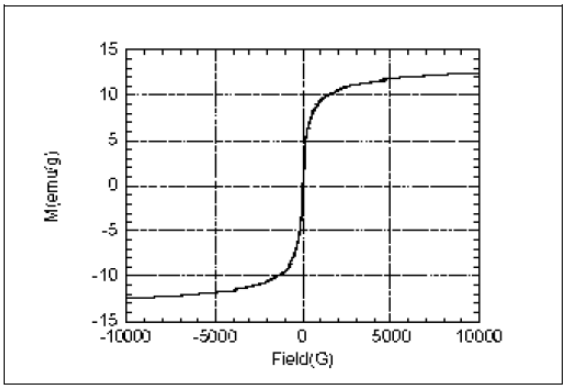


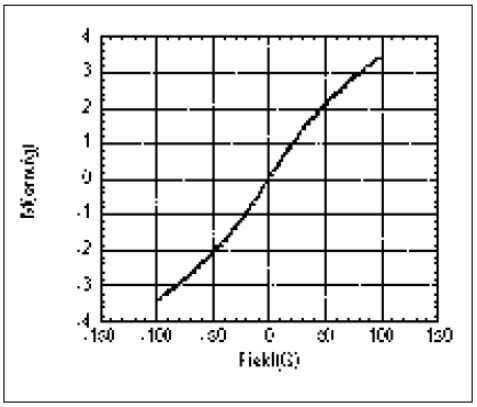


The magnetic susceptibility is used by Dynal as a measure of the beads magnetic properties. Magnetic susceptibility is measured by the oscillator method in the linear range of the magnetisation curve, and typical values for the different bead types are listed in table 2.

The magnetic force exerted on a bead – and hence the separation efficiency when exposed to a magnetic field – is dependant on the degree of magnetisation of the bead. The maximum magnetic field that may be generated by the beads is referred to as their saturation magnetisation (table 2). Due to the high magnetic content of Dynabeads their saturation magnetisation is high, which enables a quick and efficient separation even in viscous samples. Iron content in the beads are in the range 12% - 26%, depending on the bead type. This is further specified in table 2.

| **Dynabeads product** | **Diameter** $[\mu m]$ | **Magnetic Susceptibility (dry substance)** | | **Saturation Magnetisation** | | **Iron content** $[\%]$ **(w/w dry substance)** |
|---|---|---|---|---|---|---|
| | | $[m^3/kg]$ **(mass)** | $[Dimensionless]$ **(volume)** | $[A \cdot m^2/kg]$ **(mass)** | $[kA/m]$ **(volume)** | |
| M-270 Dynabeads | 2.8 | $6 \cdot 10^{-4}$ | 1.0 | 13 | 20 | 14 |
| M-280 Dynabeads | 2.8 | $5 \cdot 10^{-4}$ | 0.7 | 10 | 14 | 12 |

Table E.2: Magnetic properties of Dynabeads (typical values)

**Publication No.** MAN0014017

**Product Contents**

invitrogen
by Thermo Fisher Scientific

# Dynabeads™ M-280 Streptavidin

**Catalog nos. 11205D, 11206D, 60210** **Store at 2 to 8˚C**

| Cat. no. | Volume |
|---|---|
| 11205D | 2 mL |
| 11206D | 10 mL |
| 60210 | 100 mL |

Dynabeads™ M-280 Streptavidin contains 10 mg (~6–7 × $10^8$) Dynabeads™/mL in phosphate buffered saline (PBS) pH 7.4, with 0.1% bovine serum albumin (BSA) and 0.02% sodium azide as preservatives.

## Product Description

Dynabeads™ M-280 Streptavidin are ideal for numerous applications, including purification of proteins and nucleic acids, protein interaction studies, immunoprecipitation, immunoassays, phage display, biopanning, drug screening and cell isolation.

Add Dynabeads™ to a sample containing biotinylated molecules, e.g. peptides, proteins, antibodies, sugars, lectins, oligonucleotides, DNA/RNA. During a short incubation, the biotinylated molecule will bind to the beads. Separate the molecule-bead capture, washing, and detection can be optimized for manual or automated use. With indirect capture, mix the biotinylated molecule with the sample to capture the molecule-target complex before adding Dynabeads™. Indirect target capture is an advantage when molecule-target kinetics are slow, affinity is weak, molecule concentration is low, or molecule-target binding

lifetechnologies.com.

www.lifetechnologies.com/magnets for magnet recommendations.

- Mixing device with tilting and rotation (e.g. HulaMixer® Sample Mixer).
- Buffers and Solutions (see Table 1).
- Biotinylated compounds. For advice on biotinylation, see www.lifetechnologies.com/Dynabeads.
- For biotinylation details, download the Molecular Probes® Handbook from www.lifetechnologies.com/ handbook.

## General Guidelines

- Keep the tube on the magnet for 2 min to ensure that all the beads are collected on the tube wall.
- For diluted samples, increase the incubation time or isolate in smaller batches using the same beads in each batch.
- Avoid air bubbles during pipetting.
- Free biotin in the sample will reduce the binding capacity of the beads. A disposable separation column or a spin column will remove unincorporated biotin.
- For some applications it can be an advantage to add a detergent such as 0.01–0.1% Tween® 20 to the washing/binding buffers to reduce non-specific binding.
- Run the PCR with limiting concentrations of biotinylated primer, or remove free biotinylated primer by ultrafiltration, microdialysis or other cleanup protocols. PCR

The salt concentration and pH (typically 5–9) of the chosen binding/washing buffers can be varied depending on the type of molecule to be immobilized. Beads with immobilized molecules are stable in common buffers.

Both the size of the molecule to be immobilized and the biotinylation procedure will affect the binding capacity. The capacity for biotinylated molecules depends on steric availability and charge interaction between bead and molecule and between molecules. There are two or three biotin binding sites available for each streptavidin molecule on the surface of the bead after immobilization.

- Optimize the quantity of beads used for each individual application by titration.
- Use up to two-fold excess of the binding capacity of the biotinylated molecule to saturate streptavidin.
- Binding efficiency can be determined by comparing molecule concentration before and after coupling.

## Protocol

### Recommended Washing Buffers

- Nucleic acid applications: 1X B&W Buffer (see Table 1 for recipe). Dilute to 1X B&W Buffer with distilled water.
- Antibody/protein applications: PBS, pH 7.4.

### Wash Dynabeads™

Calculate the amount of beads required based on their binding capacity (see Table 2), and transfer the beads to a new tube.

1. Resuspend the Dynabeads™ in the vial (i.e. vortex for >30 sec, or tilt and rotate for 5 min).
2. Transfer the desired volume of Dynabeads™ to a tube.
3. Add an equal volume of Washing buffer, or at least 1 mL, and mix (vortex for 5 sec, or keep on a roller for at least 5 min).
4. Place the tube on a magnet for 1 min and discard the supernatant.
5. Remove the tube from the magnet and resuspend the washed Dynabeads™ in the same volume of washing buffer as the initial volume of Dynabeads™ taken from the vial (step 2).

Table 1: Recommended buffers and solutions

| For coupling of nucleic acids | For Dynabeads™ treatment before RNA manipulations | For coupling of proteins and other molecules |
|---|---|---|
| **Binding and washing (B&W) Buffer (2X):**<br>10 mM Tris-HCl (pH 7.5)<br>1 mM EDTA<br>2 M NaCl | **Solution A:** DEPC-treated 0.1 M NaOH<br>DEPC-treated 0.05 M NaCl<br>**Solution B:**DEPC-treated 0.1 M NaCl | PBS buffer pH 7.4<br>These buffers can also be used for your application if needed:<br>PBS/BSA (PBS, pH 7.4 containing 0.01% [w/v] BSA)<br>PBST (PBS pH 7.4 containing 0.01% [v/v] Tween®-20) |



**For support visit** www.lifetechnologies.com/support or
email techsupport@lifetech.com www.lifetechnologies.com

ThermoFisher SCIENTIFIC

**For research use only. Not for use in diagnostic procedures.**

# Appendix F Properties of Antibodies

abcam

## Product datasheet

## Anti-E. coli antibody (Biotin) ab20640

| Overview | |
|---|---|
| **Product name** | Anti-E. coli antibody (Biotin) |
| **Description** | Rabbit polyclonal to E. coli (Biotin) |
| **Conjugation** | Biotin |
| **Specificity** | Many "O" and "K" antigenic serotypes of Escherichia coli. Will remove E. coli proteins from recombinant preparations. Tested specifically with the strains O18, O20, O44, O55, O111, O112, O125, O157, K12. |
| **Tested applications** | **Suitable for:** ELISA, ICC/IF |
| **Species reactivity** | **Reacts with:** Escherichia coli |
| **Immunogen** | Tissue/ cell preparation (Mixture of E. coli serotypes: K12, O111, O55, O125, O20, and O157). |
| **General notes** | Covalently coupled with the N-Hydroxysuccinimide ester of biotin under mild conditions to give a high degree of substitution. |
| **Properties** | |
| **Form** | Liquid |
| **Storage instructions** | Shipped at 4°C. Store at +4°C short term (1-2 weeks). Store at -20°C or -80°C. Avoid freeze / thaw cycle. |
| **Storage buffer** | Preservative: 0.1% Sodium Azide<br>Constituents: 0.01M PBS, pH 7.2 |
| **Purity** | Protein A purified |
| **Purification notes** | Protein A chromatography. |
| **Clonality** | Polyclonal |
| **Isotype** | IgG |
| **Applications** | |

Our Abpromise guarantee covers the use of **ab20640** in the following tested applications.

The application notes include recommended starting dilutions; optimal dilutions/concentrations should be determined by the end user.

| Application | Abreviews | Notes |
|---|---|---|
| ELISA | | Use at an assay dependent concentration. |

abcam

Product datasheet

# Goat Anti-Rabbit IgG H&L (Alexa Fluor® 488) ab150077

| | |
|---|---|
| **Overview** | |
| **Product name** | Goat Anti-Rabbit IgG H&L (Alexa Fluor® 488) |
| **Description** | Goat polyclonal Secondary Antibody to Rabbit IgG - H&L (Alexa Fluor® 488) |
| **Target species** | Rabbit |
| **Tested applications** | **Suitable for:** ICC/IF, Flow Cyt, IHC-P, ELISA, IHC-Fr |
| **Conjugation** | Alexa Fluor® 488. Ex: 495nm, Em: 519nm |
| **Properties** | |
| **Form** | Liquid |
| **Storage instructions** | Shipped at 4°C. Store at +4°C short term (1-2 weeks). Upon delivery aliquot. Store at -20°C.<br>Avoid freeze / thaw cycle. Store In the Dark. |
| **Storage buffer** | Preservative: 0.02% Sodium azide<br>Constituents: PBS, 30% Glycerol, 1% BSA |
| **Purity** | Immunogen affinity purified |
| **Purification notes** | This antibody was isolated by affinity chromatography using antigen coupled to agarose beads. |
| **Clonality** | Polyclonal |
| **Isotype** | IgG |
| **General notes** | Alexa Fluor® is a registered trademark of Molecular Probes, Inc, a Thermo Fisher Scientific |

Company. The Alexa Fluor® dye included in this product is provided under an intellectual property license from Life Technologies Corporation. As this product contains the Alexa Fluor® dye, the purchase of this product conveys to the buyer the non-transferable right to use the purchased product and components of the product only in research conducted by the buyer (whether the buyer is an academic or for-profit entity). Carlsbad, CA 92008 USA or outlicensing@lifetech.com

**Applications**

Our Abpromise guarantee covers the use of **ab150077** in the following tested applications.
The application notes include recommended starting dilutions; optimal dilutions/concentrations should be determined by the end user.

| Application | Notes |
|---|---|
| **ICC/IF** | 1/200 - 1/1000. |
| **Flow Cyt** | 1/2000 - 1/4000. |
| **IHC-P** | ab199091 - Rabbit monoclonal IgG (Alexa Fluor® 488), is suitable for use as an isotype control to complement this secondary antibody. |
| **ELISA** | Use at an assay dependent concentration. |
| **IHC-Fr** | Use at an assay dependent concentration.<br>Use at an assay dependent concentration. |

# List of Figures

# References


1 *Tabeling, Patrick. Introduction to Microfluidics. 1. publ., Reprint. Oxford [u.a.]: Oxford UnivPress, 2006. http://media.obvsg.at/p-AC06522759-1001, page 4*

2 Mosier, Aaron P., Cady, Nathaniel C. "Analysis of Bacterial Surface Interactions Using Microfluidic Systems." *Science Progress, Science Reviews Ltd*. http://www.freepatentsonline.com/article/Science-Progress/277434768.html.

3 Johnson, Richard W. *Handbook of Fluid Dynamics, Microsystems and Microfluidics*. Second edition. Boca RatonCRC Press, 2016. http://www.gbv.de/dms/bowker/toc/9781439849552.pdf , pages 28.1-18

4 Morini, Gian Luca. "Viscous Heating." In *Encyclopedia of Microfluidics and Nanofluidics*, edited by Dongqing Li, 1–11. Springer US, 2013. doi:10.1007/978-3-642-27758-0_1670-2.

5 Hooman, K., and A. Ejlali. "Effects of Viscous Heating, Fluid Property Variation, Velocity Slip, and Temperature Jump on Convection through Parallel Plate and Circular Microchannels." *International Communications in Heat and Mass Transfer* 37, no. 1 (January 1, 2010): 34–38. doi:10.1016/j.icheatmasstransfer.2009.09.011.

6 Chakraborty, Suman. *Microfluidics and Microfabrication*, Microfluidic Transport and Micro-scale Flow Physics Berlin [u.a.]: Springer, 2010. *Page 1-4*

7 Dixit, Chandra, and Ajeet K. Kaushik. *Microfluidics for Biologists: Fundamentals and Applications*. Springer, 2016, page 24

8 Colin, Stéphane. "Introduction to Microflows." In *Microfluidics*, edited by Stéphane Colin, 1–23. John Wiley & Sons, Inc., 2013. doi:10.1002/9781118599839.ch1, page 6

9 Li, Hao, Randy Ewoldt, and Michael G. Olsen. "Turbulent and Transitional Velocity Measurements in a Rectangular Microchannel Using Microscopic Particle Image Velocimetry." *Experimental Thermal and Fluid Science* 29, no. 4 (April 1, 2005): 435–46. doi:10.1016/j.expthermflusci.2004.06.001.

10 Keinstreuer, Clement. *Microfluidics and Nanofluidics: Theory and Selected Applications*. HobokenWiley, 2013. Pages 5, 192

11 Nge, Pamela N., Chad I. Rogers, and Adam T. Woolley. "Advances in Microfluidic Materials, Functions, Integration and Applications." *Chemical Reviews* 113, no. 4 (April 10, 2013): 2550–83. doi:10.1021/cr300337x.

12 Boks, Niels P., Willem Norde, Henny C. van der Mei, and Henk J. Busscher. "Forces Involved in Bacterial Adhesion to Hydrophilic and Hydrophobic Surfaces." *Microbiology (Reading, England)* 154, no. Pt 10 (October 2008): 3122–33. doi:10.1099/mic.0.2008/018622-0.

13 Sung, H. W. F, and C Rudowicz. "Physics behind the Magnetic Hysteresis Loop—a Survey of Misconceptions in Magnetism Literature." *Journal of Magnetism and Magnetic Materials* 260, no. 1 (March 1, 2003): 250–60. doi:10.1016/S0304-8853(02)01339-2.

14 Hilzinger, Rainer, and Werner Rodewald. *Magnetic Materials: Fundamentals, Products, Properties, Applications*. Erlangen, Hanau: Publicis Publ, VAC Vacuumschmelze, 2013. pages 157, 34, 27-43

15 J. M. D. Coey. *Magnetism and Magnetic Materials: Magnetostatistics','*Cambridge University Press, 2010, Page 39

16 Stefanita, Carmen-Gabriela. *From Bulk to Nano: The Many Sides of Magnetism*. Berlin [u.a.]: Springer, 2008. http://d-nb.info/989061442/04. page 3-4

17 Stöhr, Joachim, and Hans-Christoph Siegmann. *Magnetism: From Fundamentals to Nanoscale Dynamics ; with 39 Tables*. Berlin [u.a.]: Springer, 2006. *catalogplus.tuwien.ac.at*. Web. 13 July 2017, page 480

18 Solymar, Laszlo, and Donald Walsh. Magnetic materials, *Electrical Properties of Materials*. 8. ed. Oxford [u.a.]: Oxford UnivPress, 2010. *catalogplus.tuwien.ac.at*. Web. 13 July 2017, page 281-282

19 Guimarães, Alberto P. *Principles of Nanomagnetism*. Springer Science & Business Media, 2009. page 69

20 Owens, Frank J. *Physics of Magnetic Nanostructures*, *Superparamagnetism,* John Wiley & Sons, 2015. page 35

21 Yu, Seung-Man, Kyung-Rae Dong, Youn-Sang Ji, Eun-Hoe Goo, Woon-Kwan Chung, Jong-Woong Lee, and Chong-Hwan Choe. "Signal Intensity for Contrast Enhancement as a Function of the Molarity of Gadolinium-Based MRI Contrast Media." *Applied Magnetic Resonance* 40, no. 3 (May 1, 2011): 291–301. doi:10.1007/s00723-011-0201-0.

22 Taylor, Robert M, and Laurel O Sillerud. "Paclitaxel-Loaded Iron Platinum Stealth Immunomicelles Are Potent MRI Imaging Agents That Prevent Prostate Cancer Growth in a PSMA-Dependent Manner." *International Journal of Nanomedicine* 7 (2012): 4341–52. doi:10.2147/IJN.S34381.

23 Pan, Dipanjan, Anne H. Schmieder, Samuel A. Wickline, and Gregory M. Lanza. "Manganese-Based MRI Contrast Agents: Past, Present, and Future." *Tetrahedron* 67, no. 44 (November 4, 2011): 8431–44. doi:10.1016/j.tet.2011.07.076.

24 Miele, Evelina, Gian Paolo Spinelli, Ermanno Miele, Federica Tomao, and Silverio Tomao. "Albumin-Bound Formulation of Paclitaxel (Abraxane® ABI-007) in the Treatment of Breast Cancer." *International Journal of Nanomedicine* 4 (2009): 99–105.

25 Eguchi, Haruki, Masanari Umemura, Reiko Kurotani, Hidenobu Fukumura, Itaru Sato, Jeong-Hwan Kim, Yujiro Hoshino, et al. "A Magnetic Anti-Cancer Compound for Magnet-Guided Delivery and Magnetic Resonance Imaging." *Scientific Reports* 5 (March 17, 2015). doi:10.1038/srep09194.

26 Andrä, Wilfried, Urs Häfeli, Rudolf Hergt, and Ripen Misri. "Application of Magnetic Particles in Medicine and Biology." In *Handbook of Magnetism and Advanced Magnetic Materials*. John Wiley & Sons, Ltd, 2007. doi:10.1002/9780470022184.hmm431.

27 Kumar, Challa S. S. R., and Faruq Mohammad. "Magnetic Nanomaterials for Hyperthermia-Based Therapy and Controlled Drug Delivery." *Advanced Drug Delivery Reviews*, Layer-by-Layer Self-Assembled Nanoshells for Drug Delivery, 63, no. 9 (August 14, 2011): 789–808. doi:10.1016/j.addr.2011.03.008, section 3

28 Hedayatnasab, Ziba, Faisal Abnisa, and Wan Mohd Ashri Wan Daud. "Review on Magnetic Nanoparticles for Magnetic Nanofluid Hyperthermia Application." *Materials & Design* 123 (June 5, 2017): 174–96. doi:10.1016/j.matdes.2017.03.036.

29 Zhou, Ran, and Cheng Wang. "Microfluidic Separation of Magnetic Particles with Soft Magnetic Microstructures." *Microfluidics and Nanofluidics* 20, no. 3 (March 1, 2016): 48. doi:10.1007/s10404-016-1714-5.

30 Kwak, Bongseop, Jaehun Lee, Dongkyu Lee, Kangho Lee, Ohwon Kwon, Shinwon Kang, and Youngwoo Kim. "Selective Isolation of Magnetic Nanoparticle-Mediated Heterogeneity Subpopulation of Circulating Tumor Cells Using Magnetic Gradient Based Microfluidic System." *Biosensors and Bioelectronics*, Special Issue Selected papers from the 26th Anniversary World Congress on Biosensors (Part I), 88 (February 15, 2017): 153–58. doi:10.1016/j.bios.2016.08.002.

31 Yu, Elaine Y., Mindy Bishop, Bo Zheng, R. Matthew Ferguson, Amit P. Khandhar, Scott J. Kemp, Kannan M. Krishnan, Patrick W. Goodwill, and Steven M. Conolly. "Magnetic Particle Imaging: A Novel in Vivo Imaging Platform for Cancer Detection." *Nano Letters* 17, no. 3 (March 8, 2017): 1648–54. doi:10.1021/acs.nanolett.6b04865.

32 Rho, Junsung, Jaehoon Chung, Hyungsoon Im, Monty Liong, Huilin Shao, Cesar M. Castro, Ralph Weissleder, and Hakho Lee. "Magnetic Nanosensor for Detection and Profiling of Erythrocyte-Derived Microvesicles." *ACS Nano* 7, no. 12 (December 23, 2013): 11227–33. doi:10.1021/nn405016y.

33 Bob Sinclair. "To Bead or Not To Bead: Applications of Magnetic Bead Technology | The Scientist Magazine®." *The Scientist*, June 22, 1998. http://www.the-scientist.com/?articles.view/articleNo/18984/title/To-Bead-or-Not-To-Bead--Applications-of-Magnetic-Bead-Technology/.

34 "MAGNETIC MICROPARTICLES and NANOPARTICLES - Spherotech." Accessed April 19, 2017. http://www.spherotech.com/para_par.htm.

35 "COMPEL™ | Bangs Laboratories, Inc.". http://www.bangslabs.com/products/magnetic-microspheres-particles/compel.

36 [Kolhatkar, Arati G., Andrew C. Jamison, Dmitri Litvinov, Richard C. Willson, and T. Randall Lee. "Tuning the Magnetic Properties of Nanoparticles." *International Journal of Molecular Sciences* 14, no. 8 (July 31, 2013): 15977–9. doi:10.3390/ijms140815977.]

37 Decuzzi, P., and M. Ferrari. 'The Adhesive Strength of Non-Spherical Particles Mediated by Specific Interactions'. Biomaterials 27.30 (2006): 5307-5314. ScienceDirect.

38 Woodside, Steven M., Graeme Milton, and Jason Dowd. Magnetic particles. WO2009127045 A1, filed April 16, 2009, and issued October 22, 2009. http://www.google.com/patents/WO2009127045A1.

39 Singh, Neenu, Gareth J.S. Jenkins, Romisa Asadi, and Shareen H. Doak. "Potential Toxicity of Superparamagnetic Iron Oxide Nanoparticles (SPION)." *Nano Reviews* 1 (September 21, 2010). doi:10.3402/nano.v1i0.5358.

40 Alterman, Mathias, Andreas Axen, Gunnar Glad, Dag Lindstrom, Ulrika Meyer, Nils Norrman, and Tobias Soderman. Magnetic beads comprising an outer coating of hydrophilic porous polymer and method of making thereof. US7897257 B2, filed April 13, 2006, and issued March 1, 2011. http://www.google.com/patents/US7897257.

41 ThermoFisher SCIENTIFIC. "Dynabeads Types and Uses, Dynabeads for Magnetic Separation." Accessed April 12, 2017. https://www.thermofisher.com/uk/en/home/brands/product-brand/dynal/dynabeads-types-and-uses.html.

42 Lim, JitKang, Caitlin Lanni, Eric R. Evarts, Frederick Lanni, Robert D. Tilton, and Sara A. Majetich. "Magnetophoresis of Nanoparticles." *ACS Nano* 5, no. 1 (January 25, 2011): 217–26. doi:10.1021/nn102383s.

43 Boyer, Timothy H. "The Force on a Magnetic Dipole." *American Journal of Physics* 56, no. 8 (August 1, 1988): 688–92. doi:10.1119/1.15501.

44 Furlani, Edward P., and Xiaozheng Xue. "Field, Force and Transport Analysis for Magnetic Particle-Based Gene Delivery." *Microfluidics and Nanofluidics* 13, no. 4 (October 1, 2012): 589–602. doi:10.1007/s10404-012-0975-x.

45 Kakaç, S., B. Kosoy, D. Li, and A. Pramuanjaroenkij. *Microfluidics Based Microsystems: Fundamentals and Applications*.. Springer, 2010. page 469

46 Yan, Hui, and Hongkai Wu. "Magnetophoresis" In *Encyclopedia of Microfluidics and Nanofluidics*, edited by Dongqing Li Prof, 1043–48. Springer US, 2008. doi:10.1007/978-0-387-48998-8_847, page 1034

47 Jones, Thomas B. '*Dielectrophoresis and magnetophoresis'. Electromechanics of Particles*. Cambridge: Cambridge University Press, 1995. 5–33. Print.,page 65 67

48 Plouffe, Brian D., Laura H. Lewis, and Shashi K. Murthy. “Computational Design Optimization for Microfluidic Magnetophoresis.” *Biomicrofluidics* 5, no. 1 (March 1, 2011): 013413. doi:10.1063/1.3553239.

49 Leong, Sim Siong, Zainal Ahmad, and JitKang Lim. “Magnetophoresis of Superparamagnetic Nanoparticles at Low Field Gradient: Hydrodynamic Effect.” *Soft Matter* 11, no. 35 (August 26, 2015): 6968–80. doi:10.1039/C5SM01422K.

50 Mair, L.O., and R. Superfine. “Single Particle Tracking Reveals Biphasic Transport During Nanorod Magnetophoresis Through Extracellular Matrix.” *Soft Matter* 10, no. 23 (June 21, 2014): 4118–25. doi:10.1039/c4sm00611a.

51 Bruus, Henrik. *Theoretical Microfluidics*. 1. publ., . Oxford [u.a.]: Oxford UnivPr, 2008.page 23-36

52 Rhodes, Martin. “Single Particles in a Fluid.” In *Introduction to Particle Technology*, 29–49. John Wiley & Sons, Ltd, 2008. doi:10.1002/9780470727102.ch2. page 29

53 Sun, Yu. *Micro- and Nanomanipulation Tools*. Weinheim: Wiley-VCH, 2015. *catalogplus.tuwien.ac.at*. Web. 16 June 2017, chapter 10 Unethered Magnetic Micromanipulation, page 259-266

54 Binns, Chris. “Medical Applications of Magnetic Nanoparticles.” *Frontiers of Nanoscience*, Nanomagnetism: Fundamentals and Applications, 6 (January 1, 2014): 217–58. doi:10.1016/B978-0-08-098353-0.00006-3, page 222

55 Dangl, Alexander. *Biosensing Based on Magnetically Induced Motion of Magnetic Microparticles*, 2013, https://resolver.obvsg.at/urn:nbn:at:at-ubtuw:1-77199. page 18-23, 33-36

56 Cooper, Alan. *Biophysical Chemistry*. 2. ed. Cambridge: RSC Publ/ Royal Society of Chemistry, 2011. pages 102-106

57 Barkai, E., Y. Garini, and R. Metzler. “STRANGE KINETICS of Single Molecules in Living Cells.” *Physics Today* 65, no. 8 (2012): 29–35.

58 Michalet, Xavier. “Mean Square Displacement Analysis of Single-Particle Trajectories with Localization Error: Brownian Motion in an Isotropic Medium.” *Physical Review E* 82, no. 4 (October 20, 2010): 041914. doi:10.1103/PhysRevE.82.041914.

59 Cui, Jingqin, Deng Long, Pavel Shapturenka, Ilona Kretzschmar, Xinyi Chen, and Taihong Wang. “Janus Particle-Based Microprobes: Determination of Object Orientation.” *Colloids and Surfaces A: Physicochemical and Engineering Aspects* 513 (January 5, 2017): 452–62. doi:10.1016/j.colsurfa.2016.11.017.

60 Bechinger, C., F. Sciortino, and P. Ziherl. *Physics of Complex Colloids*. IOS Press, 2013. Print. page 508

61 Dhont, J. K. G. *An Introduction to Dynamics of Colloids*. Elsevier, 1996. Print, Chapter 1, page 1-11

62 Mörters, Peter, and Yuval Peres. *Brownian Motion*. Cambridge University Press, 2010. Print.chapter 5: Brownian motion and random walk

63 Caldeira, A. O. *An Introduction to Macroscopic Quantum Phenomena and Quantum Dissipation*. Cambridge University Press, 2014. Print, Chapter 4. Stochastic processes, page 89-92

64 Wayne, Randy. *Light and Video Microscopy*. 2. ed. Amsterdam [u.a.]: Academic Press, Elsevier, 2014. http://media.obvsg.at/p-AC12087769-1001. Chapter 6: Methods of Generating Contrast, pages 111-113, 239-241, 94

65 “ZEISS Microscopy Online Campus | Microscopy Basics | Enhancing Contrast in Transmitted Light.”

http://zeiss-campus.magnet.fsu.edu/articles/basics/contrast.html.

66 Boas, David A., Constantinos Pitris, and Nimmi Ramanujam. *Handbook of Biomedical Optics*. CRC Press, 2016: page 485-486

67 “Microscope Immersion Oils.” https://www.thorlabs.com/newgrouppage9.cfm?objectgroup_id=5381.

68 Haus, Jörg. “Darkfield Microscopy with HighPower LED Illumination.” *Optik & Photonik* 10, no. 1 (February 1, 2015): 29–31. doi:10.1002/opph.201500003.

69 Mondal, Partha Pratim, and Alberto Diaspro. *Fundamentals of Fluorescence Microscopy: Exploring Life with Light*. Dordrecht [u.a.]: Springer, 2014. *catalogplus.tuwien.ac.at*. Web. 18 June 2017. Chapter1: Ray Optics, Wave Optics and Imaging System Design, page 29

70 Hu, Min, Carolina Novo, Alison Funston, Haining Wang, Hristina Staleva, Shengli Zou, Paul Mulvaney, Younan Xia, and Gregory V. Hartland. “Dark-Field Microscopy Studies of Single Metal Nanoparticles: Understanding the Factors That Influence the Linewidth of the Localized Surface Plasmon Resonance.” *Journal of Materials Chemistry* 18, no. 17 (2008): 1949–60. doi:10.1039/b714759g.

71 “Olympus Microscopy Resource Center | Specialized Microscopy Techniques - Darkfield Illumination.” http://www.olympusmicro.com/primer/techniques/darkfield.html.

72 Boas, David A., Constantinos Pitris, and Nimmi Ramanujam. *Handbook of Biomedical Optics*. CRC Press, 2016.

73 Jacobkhed. *English: Jablonski Diagram of Absorbance, Non-Radiative Decay, and Fluorescence.* N.p., 2012. *Wikimedia Commons*. Web. 17 June 2017.

74 Nienhaus, Gerd Ulrich, and Karin Nienhaus. ‘Fluorescence Labeling’. *Fluorescence Microscopy*. Ed. Ulrich Kubitscheck. Wiley-VCH Verlag GmbH & Co. KGaA, 2013. 143–173. *Wiley Online Library*. page 144

75 Birch, David J. S., Yu Chen, and Olaf J. Rolinski. Photonics: Scientific Foundations, Technology and Applications,. *Photonics*. Ed. David L. Andrews. John Wiley & Sons, Inc., 2015. Chapter: Fluorescence, *Wiley Online Library*. page 1–58.

76 Dobrucki, Jurek W. 'Fluorescence Microscopy'. *Fluorescence Microscopy*. Ed. Ulrich Kubitscheck. Wiley-VCH Verlag GmbH & Co. KGaA, 2013. 97–142. *Wiley Online Library*. page 97-118

77 Nienhaus, Gerd Ulrich, and Karin Nienhaus. 'Fluorescence Labeling'. *Fluorescence Microscopy*. Ed. Ulrich Kubitscheck. Wiley-VCH Verlag GmbH & Co. KGaA, 2013. 143–173. *Wiley Online Library*. Page 149

78 'Introduction to Fluorescence Microscopy'. *Nikon's MicroscopyU*. N.p., n.d, https://www.microscopyu.com/techniques/fluorescence/introduction-to-fluorescence-microscopy

79 "Introductory Confocal Concepts." *Nikon's MicroscopyU*. https://www.microscopyu.com/techniques/confocal/introductory-confocal-concepts.

80 'Connecting a Camera to a Microscope'. *MicrobeHunter Microscopy Magazine*. N.p., 6 Jan. 2012. Web. 18 June 2017.

81 Cristóbal, Gabriel. *Optical and digital image processing: fundamentals and applications*. Weinheim: Wiley-VCH Verl, 2011. *catalogplus.tuwien.ac.at*. Web. 18 June 2017.

82 Pitout, Johann D. D. "Escherichia Coli." In Molecular Techniques for the Study of Hospital-Acquired Infection, edited by Steven L. Foley, Anne Y. Chen, Shabbir Simjee, and rcus J. Zervos, 179–92. John Wiley & Sons, Inc., 2011. doi:10.1002/9781118063842. Chapter 11, page 179-180.

83 "Unique Characteristics of Prokaryotic Cells | Microbiology." https://courses.lumenlearning.com/microbiology/chapter/unique-characteristics-of-prokaryotic-cells

84 Yuk, Hyun-Gyun, David J. Geveke, and Howard Q. Zhang. "Efficacy of Supercritical Carbon Dioxide for Nonthermal Inactivation of Escherichia Coli K12 in Apple Cider." *International Journal of Food Microbiology* 138, no. 1–2 (March 31, 2010): 91–99. doi:10.1016/j.ijfoodmicro.2009.11.017.

85 Smith, H. Williams. "Survival of Orally Administered *E.coli* K12 in Alimentary Tract of Man." *Nature* 255, no. 5508 (June 5, 1975): 500–502. doi:10.1038/255500a0.

86Fukiya, Satoru, Hiroshi Mizoguchi, Toru Tobe, and Hideo Mori. "Extensive Genomic Diversity in Pathogenic Escherichia Coli and Shigella Strains Revealed by Comparative Genomic Hybridization Microarray." *Journal of Bacteriology* 186, no. 12 (June 2004): 3911–21. doi:10.1128/JB.186.12.3911-3921.2004.

87 Reshes, Galina, Sharon Vanounou, Itzhak Fishov, and Mario Feingold. "Cell Shape Dynamics in Escherichia Coli." *Biophysical Journal* 94, no. 1 (January 1, 2008): 251–64. doi:10.1529/biophysj.107.104398.

88 Bogosian, G, L E Sammons, P J Morris, J P O'Neil, M A Heitkamp, and D B Weber. "Death of the Escherichia Coli K-12 Strain W3110 in Soil and Water." *Applied and Environmental Microbiology* 62, no. 11 (November 1996): 4114–20.

89 Navarre, William Wiley, and Olaf Schneewind. "Surface Proteins of Gram-Positive Bacteria and Mechanisms of Their Targeting to the Cell Wall Envelope." *Microbiology and Molecular Biology Reviews : MMBR* 63, no. 1 (March 1999): 174–229.

90 Maurer, Lisa M., Elizabeth Yohannes, Sandra S. Bondurant, Michael Radmacher, and Joan L. Slonczewski. "pH Regulates Genes for Flagellar Motility, Catabolism, and Oxidative Stress in Escherichia Coli K-12." *Journal of Bacteriology* 187, no. 1 (January 2005): 304–19. doi:10.1128/JB.187.1.304-319.2005.

91 Marlies Leenaars and Coenraad F. M. Hendriksen, 'Critical Steps in the Production of Polyclonal and Monoclonal Antibodies: Evaluation and Recommendations', *ILAR Journal* 46, no. 3 (1 January 2005): 269–79, doi:10.1093/ilar.46.3.269.

92 "Rabbits Produce Superior Antibodies | Abcam", http://www.abcam.com/primary-antibodies/reasons-why-rabbits-are-capable-of-producing-superior-antibodies.

93 Thermo Scientific Pierce, 'Antibody Production and Purification Technical Handbook', *Thermo Fisher Scintific*, September 2010, Protein Biology Resource Library.

94"Custom Rabbit Polyclonal Antibody Production Protocols.", company homepage, https://www.thermofisher.com/uk/en/home/life-science/antibodies/custom-antibodies/custom-antibody-production/custom-polyclonal-antibody-production/custom-rabbit-polyclonal-antibody-production-protocols.html.

95 Innovagen AB, 'Polyclonal Goat Antibodies', company homepage, *Research Products and Services in the Field of Molecular Biology*, accessed 21 October 2016, http://www.innovagen.com/polyclonal-goat-antibodies.

96 Saber, R., S. Sarkar, P. Gill, B. Nazari, and F. Faridani. "High Resolution Imaging of IgG and IgM Molecules by Scanning Tunneling Microscopy in Air Condition." *Scientia Iranica* 18, no. 6 (December 2011): 1643–46. doi:10.1016/j.scient.2011.11.028.

97 Chen, Yong, Jiye Cai, Qingcai Xu, and Zheng W. Chen. "Atomic Force Bio-Analytics of Polymerization and Aggregation of Phycoerythrin-Conjugated Immunoglobulin G Molecules." *Molecular Immunology* 41, no. 12 (November 2004): 1247–52. doi:10.1016/j.molimm.2004.05.012.

98 Claire-Marie Pradier and Yves Jean Chabal, Biointerface Characterization by Advanced IR Spectroscopy (Elsevier, 2011). 84

99 Michael Green. *Advances in Protein Chemistry*. Vol. 29. Academic Press, 1975. page 85-133

100 O'Sullivan, Valerie J., Isabelle Barrette-Ng, Eric Hommema, Greg T. Hermanson, Mark Schofield, Sau-Ching Wu, Claudia Honetschlaeger, Kenneth K.-S. Ng, and Sui-Lam Wong. "Development of a Tetrameric Streptavidin Mutein with Reversible Biotin Binding Capability: Engineering a Mobile Loop as an Exit Door for Biotin." *PLOS ONE* 7, no. 4 (April 19, 2012): e35203. doi:10.1371/journal.pone.0035203.

101 “11206D Documents & Support and Product FAQs | Thermo Fisher Scientific.” https://www.thermofisher.com/search/results?query=11206D&persona=DocSupport&type=Product+FAQs.

102 Neish, Calum S., Ian L. Martin, Robert M. Henderson, and J. Michael Edwardson. “Direct Visualization of Ligand-Protein Interactions Using Atomic Force Microscopy.” *British Journal of Pharmacology* 135, no. 8 (April 2002): 1943–50. doi:10.1038/sj.bjp.0704660.

103 “14305D Documents & Support and Product FAQs | Thermo Fisher Scientific.” https://www.thermofisher.com/search/results?query=14305D&persona=DocSupport&resultPage=2&resultsPerPage=15.

104 “Dynabeads M-270 Carboxylic Acid - Thermo Fisher Scientific.” Accessed August 15, 2017. https://www.thermofisher.com/order/catalog/product/14305D.

105 Saber, R., S. Sarkar, P. Gill, B. Nazari, and F. Faridani. “High Resolution Imaging of IgG and IgM Molecules by Scanning Tunneling Microscopy in Air Condition.” *Scientia Iranica* 18, no. 6 (December 2011): 1643–46. doi:10.1016/j.scient.2011.11.028.

106 Chen, Yong, Jiye Cai, Qingcai Xu, and Zheng W. Chen. “Atomic Force Bio-Analytics of Polymerization and Aggregation of Phycoerythrin-Conjugated Immunoglobulin G Molecules.” *Molecular Immunology* 41, no. 12 (November 2004): 1247–52. doi:10.1016/j.molimm.2004.05.012.

107 “Importance of Isoelectric Point (PI) of Antibodies.” *The Antibody Society*, June 28, 2017. http://www.antibodysociety.org/importance-isoelectric-point-pi-antibodies/.

108 Zourob, Mohammed, Sauna Elwary, and Anthony P. F. Turner. *Principles of Bacterial Detection: Biosensors, Recognition Receptors and Microsystems*. Springer Science & Business Media, 2008. page 161

109 Haiden, Christoph. *Optical Micro- and Nanoparticle Characterization in Microfluidics*. Wien, 2016.

110 Yan, Hui, and Hongkai Wu. “Magnetophoresis.” In *Encyclopedia of Microfluidics and Nanofluidics*, edited by Dongqing Li, 1–8. Springer US, 2014. doi:10.1007/978-3-642-27758-0_847-2.

111 Lim, JitKang, David X. Tan, Frederick Lanni, Robert D. Tilton, and Sara A. Majetich. “Optical Imaging and Magnetophoresis of Nanorods.” *Journal of Magnetism and Magnetic Materials*, Proceedings of the Seventh International Conference on the Scientific and Clinical Applications of Magnetic Carriers, 321, no. 10 (May 2009): 1557–62. doi:10.1016/j.jmmm.2009.02.085.

112 Crocker, John C., and David G. Grier. “Methods of Digital Video Microscopy for Colloidal Studies.” *Journal of Colloid and Interface Science* 179, no. 1 (April 15, 1996): 298–310. doi:10.1006/jcis.1996.0217.

113 Haiden, C. et al. ‘Sizing of Metallic Nanoparticles Confined to a Microfluidic Film Applying Dark-Field Particle Tracking’. *Langmuir* 30.31 (2014): 9607–9615. *ACS Publications*. Web.

114 Haiden, C. et al. ‘A Microfluidic Chip and Dark-Field Imaging System for Size Measurement of Metal Wear Particles in Oil’. *IEEE Sensors Journal* 16.5 (2016): 1182–1189. *IEEE Xplore*. Web.

115 Haiden, C. et al. ‘Concurrent Particle Diffusion and Sedimentation Measurements Using Two-Dimensional Tracking in a Vertical Sample Arrangement’. *Applied Physics Letters* 108.9 (2016): 094101. *aip.scitation.org (Atypon)*. Web.

116 Hasinoff, Samuel W. “Saturation (Imaging).” In *Computer Vision*, edited by Katsushi Ikeuchi, 699–701. Springer US, 2014. doi:10.1007/978-0-387-31439-6_483.

117 “Depth of Field and Depth of Focus | Edmund Optics.”. https://www.edmundoptics.com/resources/application-notes/imaging/depth-of-field-and-depth-of-focus/.

118 Zhang, Xiaoning, DaShan Brodus, Valerie Hollimon, and Hongmei Hu. “A Brief Review of Recent Developments in the Designs That Prevent Bio-Fouling on Silicon and Silicon-Based Materials.” *Chemistry Central Journal* 11 (February 20, 2017): 18. doi:10.1186/s13065-017-0246-8.

119 Israelachvili, Jacob N. *Intermolecular and Surface Forces*. Academic Press, 2011, page 402

120 García Núñez, C., M. Sachsenhauser, B. Blashcke, A. García Marín, Jose A. Garrido, and Jose L. Pau. “Effects of Hydroxylation and Silanization on the Surface Properties of ZnO Nanowires.” *ACS Applied Materials & Interfaces* 7, no. 9 (March 11, 2015): 5331–37. doi:10.1021/am508752m.

121 “Histogram Plot - MATLAB – MathWorks, https://de.mathworks.com/help/matlab/ref/histogram.html#buhzsb0-1

122 Zhiyao, Song et al. ‘A Simple Formula for Predicting Settling Velocity of Sediment Particles’. *Water Science and Engineering* 1.1 (2008): 37–43. *ScienceDirect*. Web.

123“Box Plot - MATLAB Boxplot - MathWorks Deutschland.” Accessed October 4, 2017. https://de.mathworks.com/help/stats/boxplot.html?requestedDomain=www.mathworks.com.

124 Kokkinis, G., B. Plochberger, S. Cardoso, F. Keplinger, and I. Giouroudi. “A Microfluidic, Dual-Purpose Sensor for in Vitro Detection of Enterobacteriaceae and Biotinylated Antibodies.” *Lab on a Chip* 16, no. 7 (March 23, 2016): 1261–71. doi:10.1039/C6LC00008H.